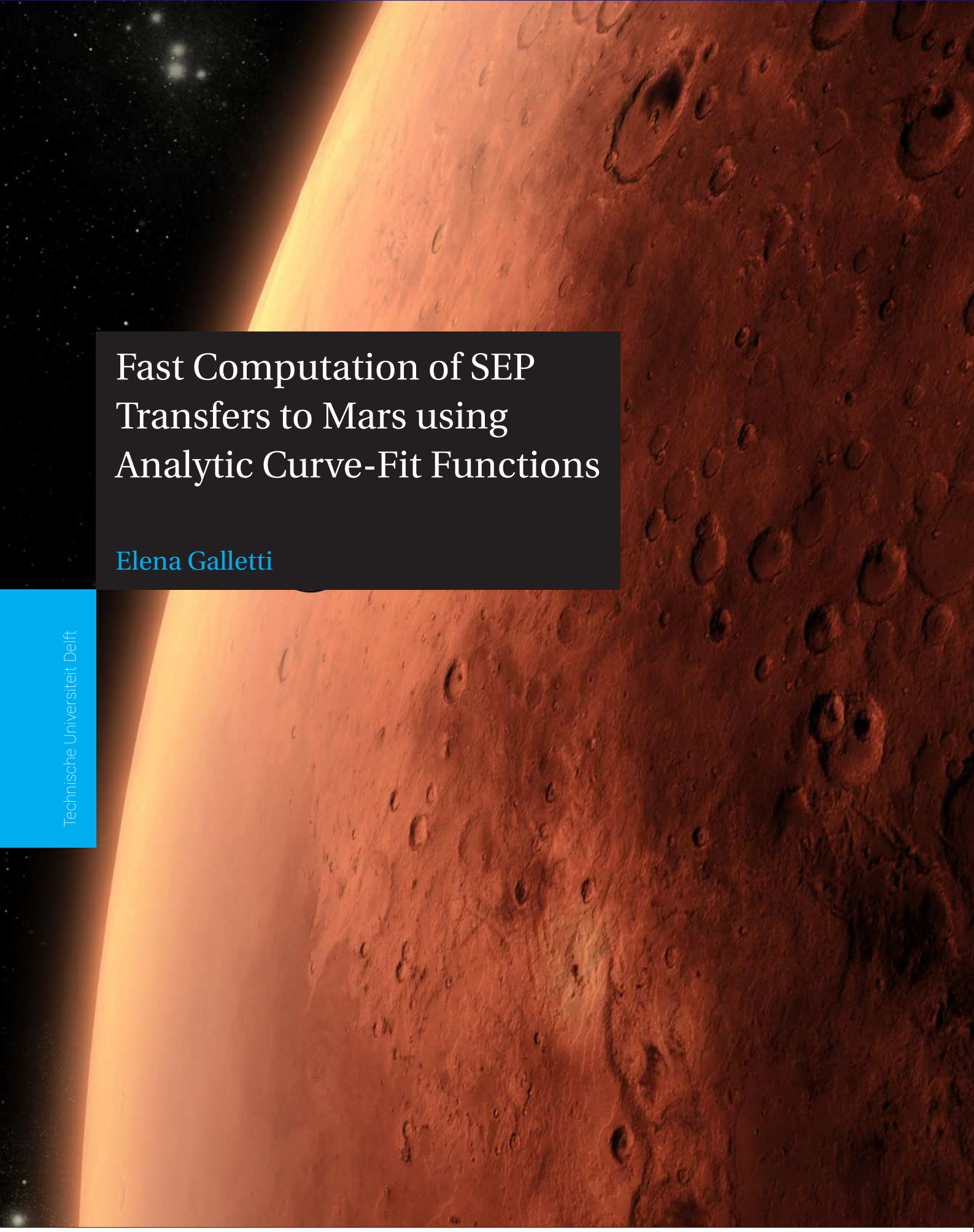

Fast Computation of SEP Transfers to Mars using Analytic Curve-Fit Functions

Elena Galletti

Technische Universiteit Delft

TU Delft Delft University of Technology

esa

Challenge the future

The image on the front page has been retrieved from `https://mars.nasa.gov/msl/multimedia/images/`. It represents an artist's impression of Mars. Image credit: NASA/JPL-CALTECH.

Fast Computation of SEP Transfers to Mars using Analytic Curve-Fit Functions

by

Elena Galletti

in partial fulfilment of the requirements for the degree of

Master of Science
in Aerospace Engineering

at the Delft University of Technology,
to be defended publicly on Tuesday September 26, 2017 at 1:00 PM.

Student number:	4521102	
Project duration:	January 16, 2017 – August 21, 2017	
Thesis Committee:	Prof. Dr. Ir. P. N. A. M. Visser	TU Delft
	Ir. R. Noomen	TU Delft
	K. J. Kowan	TU Delft
	J. M. Sanchez Perez	European Space Agency

This thesis is confidential and cannot be made public until September 26, 2017.

An electronic version of this thesis is available at `http://repository.tudelft.nl/`.

Acknowledgements

This piece of work concludes a two-year long adventure through two different countries and a number of significant challenges, that has marked my life indelibly. A few people deserve special thanks for taking part in this unforgettable learning experience.

I am very grateful to my supervisor Ron Noomen for engaging and supporting me from day one, always making precise and useful suggestions to overcome the difficulties of the project, but also never sparing a "Good job!" after achievement of some result. This kind of motivation and guidance has been very precious.

Special gratitude to Jose Manuel, who has been my mentor during the time spent at ESOC and has followed each step of the project with attention and patience, finding the time for frequent meetings and providing very relevant advice. Thanks also to the rest of the ESOC team, for creating an enjoyable work environment to look forward to in the morning.

To the brightest girl I have ever known, Mònica: during these two years of changes and challenges we have gone through all shades of friendship, as classmates, travel companions, officemates and, most importantly, true allies. I want to say thanks because, in all situations, and in all languages, you have always managed to make it all a lot of fun.

Thanks to my lifelong partners Francesca e Alice for teaching me how to make things last, and grow. Our lasting and loving friendship is and will always be the safest place, the strongest bond, the sweetest responsibility.

The greatest and most special thanks go out to my parents, to Chiara and to Alessandro for being by my side at each step of the journey. Without your continued and unconditional love and support none of this would have been possible.

Elena Galletti
Darmstadt, August 2017

Abstract

The increasing interest in solar electric propulsion (SEP) techniques, that enable significant propellant mass savings for a wide class of transfers, has brought about a revolution in the approach to trajectory design and optimization, as a result of the complexity and diversity of the problem. To date, solutions of different nature exist, but numerical methods that require significant computational effort and user experience are typically used already in the early stages of mission design, due to the limited availability of reliable medium-to-low fidelity design tools for SEP transfers. This research project proposes a novel method that computes transfer performance parameters for Earth-Mars mass-optimal SEP transfers, by means of empirically derived analytic relations. The method is intended for applications such as concurrent engineering and early-phase concept development, which require the fast characterization of a broad design space. Besides accommodating a wide range of currently available SEP systems, the method successfully deals with the modelling of the effect of non-zero infinity velocity at departure and/or arrival.

The methodology that has been applied consists of a first phase of generation and characterization of the transfers, and of the subsequent selection of the model variables and derivation of model functions and architecture. With regard to the generation of the transfers, it is assumed that the transfers are coplanar and that the initial and target orbits are circular. Hundreds of transfers are optimized in a semi-automatic way and characterized in terms of thrust profile and transfer performance parameters. In the investigated design space, different regimes are identified, but approximately 90% of the acceleration range of interest falls into the thrust-coast-thrust profile for any combination of departure and arrival infinity velocity. For a proper description of the underlying trends in the transfer parameters, three key variables have been identified, namely the average acceleration, the total infinity velocity and the infinity velocity at arrival (expressed as a function of the total infinity velocity). By means of curve-fitting, analytic relations are derived that successfully describe those trends, limited to the thrust-coast-thrust class of transfers.

The method that is presented here computes near-optimal transfers in terms of ΔV cost, transfer time, transfer angle and departure date. While the first three parameters are the outputs of the curve-fit model mentioned above, the departure date is computed by solving analytically the problem of the phasing with Mars, in a subsequent step. The fit functions that are derived model circle-to-circle planar transfers with an accuracy in the order of 0.1% with respect to the ΔV, 1.5% with respect to the transfer time and 1.2% with respect to the transfer angle, successfully dealing with the dependence on the departure and arrival infinity velocities and generating instant estimates for all relevant transfer parameters. When the model performance is considered in relation to transfers derived in the full ephemeris model, the errors are within 1% for the ΔV, within 15% for the transfer time and within 12% for the transfer angle, which, together with the demonstrated efficiency and simplicity of implementation, make it suitable both for early-stage assessments and for generation of suitable first guesses.

Contents

List of Symbols

Symbol	Units	Description
ΔV	m/s	Velocity variation
I_{sp}	s	Specific impulse
c_e	m/s	Effective exhaust velocity
g_0	m/s^2	Standard gravity
v_∞	m/s	Infinity velocity
m	kg	Mass
t	s	Time
TOF	days	Time of flight
θ_T	∘	Transfer angle
θ_C	∘	Coast angle
$\vec{r}$	m	Position vector
$\vec{v}$	m/s	Velocity vector
$\vec{w}$	rad/s	Angular velocity vector
$\vec{a}_{tot}$	m/s^2	Total acceleration vector
$\vec{g}$	m/s^2	Central acceleration vector
$\vec{f}_p$	m/s^2	Perturbing acceleration vector
l	m	Semi-latus rectum
e	–	Eccentricity
i	∘	Inclination
θ	∘	True anomaly
ω	∘	Argument of the pericenter
Ω	∘	Right ascension of the ascending node
H	m^2/s	Specific angular momentum
μ	m^3/s^2	Gravitational parameter
G	m^3/kg$\cdot$s^2	Gravitational constant
$\vec{T}$	N	Thrust vector
A	m^2	Area
p	Pa	Pressure
m_p	kg	Propellant mass
W	W/m^2	Solar flux
P	W	Power
F	N	Force
η	–	Efficiency
$\bar{a}$	m/s^2	Average acceleration
C_D	–	Drag coefficient
C_R	–	Reflectivity
B	–	Ballistic coefficient
ρ	kg/m^3	Atmospheric density
R	m	Mean equatorial Earth radius
c	m/s	Speed of light
δ	∘	Sun aspect angle
α	–	Surface absorptivity
σ	W/m$^2\cdot$K^4	Stefan-Boltzmann constant
κ	–	Surface ratio
ϵ	–	Emissivity
T	K	Temperature
C_T	%/K	Temperature coefficient

Acronyms

AU	Astronomical Unit
COV	Calculus of Variations
DFET	Direct Finite Element Transcription
DITAN	Direct Interplanetary Trajectory Analysis
ESA	European Space Agency
ESOC	European Space Operations Centre
FET	Finite Elements in Time
GEO	Geostationary Earth Orbit
JAXA	Japan Aerospace Exploration Agency
JPL	Jet Propulsion Laboratory
MALTO	Mission Analysis Low-Thrust Optimizer
NASA	National Aeronautics and Space Administration
NLP	Non Linear Programming
OCP	Optimal Control Problem
OTIS	Optimal Trajectories by Implicit Simulation
PPU	Power Processor Unit
RSS	Root of Sum of Squares
SEP	Solar Electric Propulsion
SMART	Small Missions for Advanced Research in Technology
SW	Software
TOF	Time Of Flight
VARITOP	Variational calculus Trajectory Optimization Program
2BP	Two-Body Problem

1 Introduction

For missions that stay in the inner Solar System, Solar Electric Propulsion (SEP) represents nowadays an enabling technology, under consideration for most ongoing and future projects, especially for high ΔV missions. It is known, however, that the continuous nature of the low-thrust transfer optimization problem poses great challenges to trajectory design [Racca, 2003]. Use of advanced optimization tools implies a significant computational effort and user experience, while in the early design stages implementation of faster and simpler techniques is advantageous. The subject of this research is related to the derivation of a model that enables quick computation of the transfer performance parameters, which is intended for applications as concurrent engineering and early-stage concept development. In the present chapter, the project is put into context with regard to mission heritage and state-of-the-art research, in Sections 1.1 and 1.2. Then, the methodology proposed is introduced and detailed in terms of research objectives, in Section 1.3, and tasks, in Section 1.4.

1.1. Framework

The very first demonstration of SEP as primary propulsion system dates back to 1998, with Deep Space 1 within the framework of NASA's New Millenium Program [Sovey et al., 2001]. Since then, the technology has been used in a number of missions beyond geostationary Earth orbit (GEO) [Dankanich, 2010], the most relevant listed in Table 1.1. Nowadays, SEP is considered one of the key technologies for affordable future exploration missions. Its benefits are most significant for missions that stay in the inner Solar System, with specific regard to missions that require large ΔVs, involving for example multiple targets, big inclination changes or time-limited deep space rendezvous [Dankanich, 2010]. The decrease of the available power when moving away from the Sun, as well as the limitations due to the solar arrays technology, are outweighed by the savings in terms of propellant mass, related to the high exhaust velocities of these systems. This is the reason for the frequent inclusion of such a propulsion technique in the trade-off for missions with the mentioned features.

Mission	***Operator***	***Year***	***Type***	***Target***
Deep Space 1	NASA	1998	Flyby	asteroid 9969 Braille
Hayabusa	JAXA	2003	Sample return	near-Earth asteroid (25143 Itokawa)
SMART-1	ESA	2003	Orbiter	Moon
Dawn	NASA	2007	Orbiter	asteroids Vesta, Ceres
Hayabusa 2	JAXA	2014	Sample return	asteroid Apollo (162173 Ryugu)

Table 1.1: Deep space missions using low-thrust propulsion [Sovey et al., 2001] [Kuninaka and Kajiwara, 2011] [Estublier et al., 2007].

With regard to trajectory analysis, the revolution represented by low-thrust transfers is twofold. The advent of new propulsion techniques creates further opportunities for efficient transfers, but it also complicates significantly the problem of transfer design and optimization. The very low thrust provided by these systems results in finite-time thrusting periods, meaning that the trajectory is not shaped any longer by gravitational attraction only. The problem becomes a continuous optimization problem, requiring a fundamentally different mathematical approach for the trajectory design [Racca, 2003].

A large number of methods and tools have been developed in the last 20 years to deal with low-thrust trajectory design. Analytic solutions have been derived, but these are however restricted to specific cases, due to the complexity of the problem [Conway, 2010]. There has been the effort of extending graphical techniques such as Tisserand graphs to low-thrust transfers, although limited to simple control laws, in order to preserve the simplified nature of the technique [Chen et al., 2008] [Campagnola et al., 2014]. Semi-analytical methods have also become very popular, which assume a shape for the trajectory by means of a known analytic function, characterized by a small number of parameters. Those parameters are optimized by means of simple algorithms, and possibly shaped-based solutions are combined with global optimization methods. A review of some common shapes can be found in [Petropoulos and Sims, 2002], while a more recent discussion is provided by [Gondelach, 2012]. Although they perform well in generating approximated optimal solutions, the resulting trajectory may not have a feasible thrust profile, especially for SEP systems where the distance spacecraft-Sun plays a dominant role [Kluever, 2014].

Due to the limitations that have been pointed out above, numerical optimization methods are typically employed for the design of low-thrust transfers. They are generally grouped into direct, indirect and stochastic methods, as detailed in the comprehensive overview provided by [Conway, 2010]. While very advanced numerical methods have been developed, that can deal with complex problems and generate accurate optimal trajectories, such tools are less suitable for early-stage assessments and broad searches. In fact, in the initial phases of a project, trajectory analysis consists in the definition of the transfer options and the characterization of a broad search space. For such activities, efficiency and simplicity of implementation are crucial features of the methods employed, and outweigh (to a certain extent) aspects like accuracy. Figure 1.1 sums up some of the most relevant design methods and tools that are currently used for SEP missions, in relation to the specific phase of the trajectory analysis process.

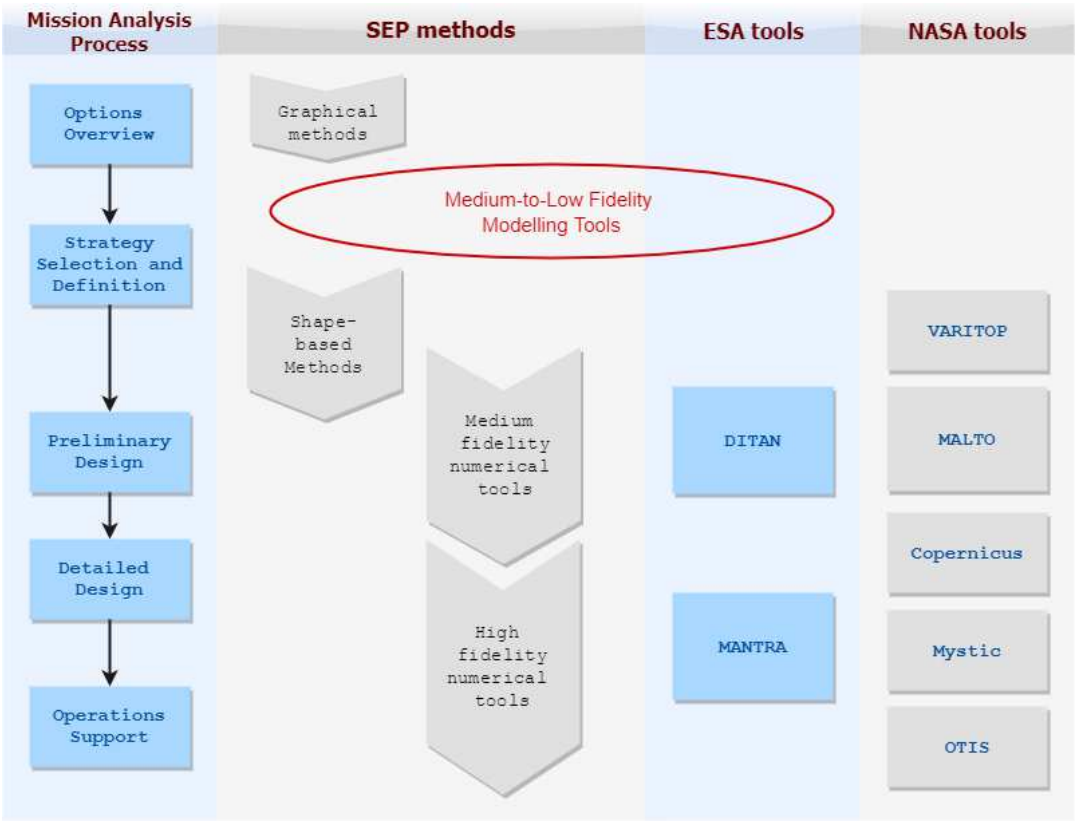

Figure 1.1: Inventory of SEP design methods and tools, in relation to the corresponding stage of the mission analysis process.

Especially in comparison with the large number of graphical methods, look-up tables and analytic relations that provide quick estimates for chemical propulsion transfers, the availability of such tools for SEP trajectories is very limited. A significant gap exists in terms of quick trajectory computation tools, which is shown in Figure 1.1. They are crucial for applications such as concurrent engineering and early-stage assessments.

1.2. State of the art

In recent literature, the potential of simple analytic relations that quickly model optimal trajectories, derived from the analysis and characterization of pre-optimized transfers, has been identified and investigated. In particular, the strategy proposed consists in generating quantitative trajectory data to targets of interest, and studying a combination of physics-based and empirical functions to determine the trends in the transfer performance parameters such as ΔV cost and transfer time. Such an approach is most beneficial when target bodies such as Mars and Jupiter are addressed, which are continuously under study. The methodology was first applied to the constant-power case, both for chemical-electric orbit-raising missions [Oh et al., 2004] and interplanetary applications [Oh, 2006]. More recently, the analysis was extended to variable-power optimum specific impulse transfers by the same group [Oh and Landau, 2010] [Oh and Landau, 2011] [Oh and Landau, 2013], and to some extent also to fixed non-optimum specific impulse systems [Oh and Landau, 2011].

Regarding the variable-power model, circular coplanar orbits are assumed for the celestial bodies, and several targets in the Solar System are included. A dataset of several thousands of fixed-time mass-optimal transfers was generated and modelled by means of both physics-based and empirical relations, resulting in a set of analytic functions to estimate optimum specific impulse and mass fraction. Besides the transfer time and the system parameters, infinity velocity at departure or at arrival were included as inputs[1]. The reported errors amount to a maximum of 15% for the final mass and 21% for the specific impulse, for all destinations [Oh and Landau, 2013]. Progress made towards an extended model that accounts for more realistic fixed non-optimum specific impulse introduced an empirical ΔV correction that depends on the thrust-to-mass ratio and transfer time [Oh and Landau, 2011]. The reported errors for the extended model amount to a maximum of +/-15% in the mass fraction for the majority of the data points[2] [Oh and Landau, 2013].

A similar methodology has been used in more recent work to parameterize inward and outward SEP transfers between arbitrary circular orbits. As in the previous studies, the model is derived by analysis of a database of optimal transfers, and refers to circular coplanar orbits. The main difference in terms of problem formulation lies in the setup of the optimization: mass optimal transfers are found with free transfer time, but with a defined thrust profile (three sub-arcs: *thrust-coast-thrust*). As for the dataset generation, circular orbits with arbitrary radius between 1 and 2 AU are used as departure and target orbits, instead of specific celestial bodies. The four output variables ΔV, transfer time, transfer angle and coast angle are parameterized with respect to the system parameters and the orbits radii, only by means of empirical relations obtained by curve-fitting. Infinity velocities are not included in the model. Relative errors are in order of a few percentage points for all variables for current SEP systems, exceeding 5% only in the case of the coast angle [Kluever, 2014].

The main characteristics of the models described above are summarized in Table 1.2. Although the setups are different, they both show the potential of analyzing pre-optimized transfers to derive more general analytic relations. The errors in the computed transfer parameters are in fact compatible with the results of preliminary assessments and options investigation, while the efficiency and simplicity of implementation of such methods allow to carry out broad searches with a limited amount of effort and time. The difficulties of modelling the discontinuities between different sets of families are pointed out, which results in much better accuracies if the model is restricted to a specific thrust profile.

Model	***Obj***	***Assumptions***	***Destinations***	***Model functions***	***Inputs***	***Outputs***	***Accuracy***
JPL	mass	circular coplanar fixed TOF	celestial bodies	empirical physics-based	system parameters flight time infinity velocities	I^*_{sp} m^*_f m_f	$+/-20\%$ $+8/-15\%$ $+/-15\%$ [a]
Kluever	mass	circular coplanar t-c-t profile	arbitrary circular orbits	empirical	system parameters radii	TOF ΔV θ_T θ_C	4% $<1\%$ 4% 7%

Table 1.2: General characteristics and performance of SEP modelling tools [Oh and Landau, 2011] [Kluever, 2014].

[a] For a limited number of transfers, mass fraction errors exceed 15%. Globally non-optimal solutions that have errors greater than 50% were omitted [Oh and Landau, 2011].

[1] Combined effect of non-zero departure infinity velocity and non-zero arrival infinity velocity is not taken into account.

[2] Results are only presented for the case of Earth-Jupiter transfers.

1.3. Objective Definition

The research project proposes to further investigate the possibility of analyzing a database of existing optimal transfers to derive simple analytic model functions. In the light of the conducted survey of current methods and of the study of recent literature, in the coming paragraphs the problem is formulated and detailed, with specific regard to the innovative aspects and methodology.

1.3.1. Problem Statement

The study is concerned with free-time mass-optimal SEP transfers between circular coplanar orbits. For a realistic description of currently available SEP technology, systems with variable power and fixed non-optimum specific impulse are considered. A relevant extension with respect to previous studies is the analysis of the dependence of the transfer performance parameters on the departure and arrival infinity velocities. A successful description of this dependence could extend the modelling to a wider range of real applications, and even pave the way for a generalization to multiple-leg missions. The purpose being the development of a novel methodology to describe these trends, rather than the repetitive examination of a large number of destinations, the analysis is limited to Earth-Mars transfers. This selection obviously follows from the central role of the planet in current exploration programs, due to its proximity and its features.

Turning to the operational aspects, it has been decided to derive analytic relations by means of a curve-fitting process, according to the promising results found in literature. However, in order to gain more insight in the physics of the problem, an initial phase of characterization of the transfers is introduced. First, trajectories are optimized with no specification in terms of thrust profile[3]. Later, before proceeding with the examination and data fitting, they undergo an extensive analysis and are categorized into distinct families depending on their characteristics. Since the optimizer is not intended to introduce any novel element but is only used as a tool to build the database, it was decided to carry out the optimization by means of existing software available on site, that is compatible with the problem formulation and has been widely tested and used.

1.3.2. Research Questions

For proper definition of the research objectives, the aspects to be examined are formalized through two main research questions, which are in turn structured into a number of sub-questions:

RQ1 - How can quantitative data be generated so as to effectively capture the main characteristics of mass-optimal Earth-Mars transfers using solar electric propulsion?

- **RQ1.1** - What simplifications/assumptions in the problem description are needed to reduce the complexity and diversity of such transfers without causing major inaccuracies?
- **RQ1.2** - For generation of a representative dataset, what are the key variables and what is the range of interest and the required resolution for each of them?
- **RQ1.3** - What are the characteristics of the corresponding transfers in terms of thrust profile, number of revolutions and typical values of transfer performance parameters?

RQ2 - To what extent can empirical functions derived by curve-fitting describe trends in the transfer parameters depending on the system parameters, and account for infinity velocity at departure and arrival?

- **RQ2.1** - What analytic relations describe these trends best and with what accuracy?
- **RQ2.2** - What is the performance of the modelling tool resulting from the combination of such model functions in computing transfers performance parameters?
  - **RQ2.2.1** - What is the performance in relation to transfers between circular coplanar orbits? Is the requirement of maximum error of 5% for all transfer parameters met, when the analysis is extended to include the effect of the infinity velocities?
  - **RQ2.2.2** - What is the performance in relation to transfers optimized in the full ephemeris model? Is the requirement of maximum error of 15-20% for all transfer parameters, that is typically adopted of the intended applications, met?

[3] The restriction on the thrust follows from the profile used to describe SEP systems, but no specific sequence or number of arcs is prescribed.

1.3.3. Research Objectives

The objectives of the research can be stated as three main goals, by organizing the requirements that follow from the research questions of Subsection 1.3.2:

OBJ1 - **Generation of the database**. Model description, establishment of the database structure and composition, trajectories optimization and subsequent characterization of the generated transfers.

OBJ2 - **Model derivation**. Examination of the quantitative data, identification of suitable analytic model functions and integration of the derived expressions into a comprehensive architecture.

OBJ3 - **Performance assessment**. Model testing and assessment of the performance by means of test cases derived under the circular coplanar assumption, as well as in the full ephemeris model.

1.4. Methodology

The three research objectives result in three project phases which, for detailed presentation of the methodology that has been followed, are described here and organized into tasks. For illustration purposes, the breakdown structure is visualized in Figure 1.2. It is worth pointing out that the three phases of the project are equally significant in terms of relevance and conclusions drawn, as well as of effort and time consumption.

T1 - **Database generation**

- **T1.1** - **Model description**: *Chapter 2*
  Mathematical modelling of the dynamical environment and propulsion system.
- **T1.2** - **Database structure and composition**: *Section 3.1*
  Selection of input and output variables and identification of ranges of interest as well as of discrete values of each variable that provide sufficient resolution of the design space.
- **T1.3** - **Trajectory optimization**: *Section 3.2*
  Implementation aspects, including introduction to the software tools, software verification, setup and automation of the continuation problem, trajectory optimization.
- **T1.4** - **Transfers characterization**: *Section 3.3*
  Analysis and categorization of the optimal transfers, identification of typical thrust profiles and values of performance parameters and number of revolutions.

T2 - **Model derivation**

- **T2.1** - **Analysis of zero infinity velocity transfers**: *Section 4.1*
  Identification of proper independent variables and derivation of model functions by curve fitting.
- **T2.2** - **Analysis of non-zero infinity velocity transfers**: *Section 4.2*
  Identification of proper independent variables and derivation of model functions by curve fitting.
- **T2.3** - **Establishment of model architecture**: *Chapter 5*
  Integration of the model functions, phasing problem and description of the full architecture.

T3 - **Performance assessment**

- **T3.1** - **Residuals analysis**: *Section 6.1*
  Study of the significance and distribution of the residuals of the entire dataset.
- **T3.2** - **Testing and verification**: *Section 6.2*
  Generation of test cases and determination of the model accuracy in the simplified dynamics.
- **T3.3** - **Comparison with full ephemeris model**: *Section 6.3*
  Considerations on accuracy and applicability of the tool in the full ephemeris model.

For easy reference to the table of contents, the list that has just been presented includes the location of each topic in the report. It can be noticed that the analysis spans over the five chapters that compose the core of the document, namely Chapters 2 to 6. The remainder of the report consists of this introduction, the conclusions that have been drawn (Chapter 7) and the additional information that is included in the appendices.

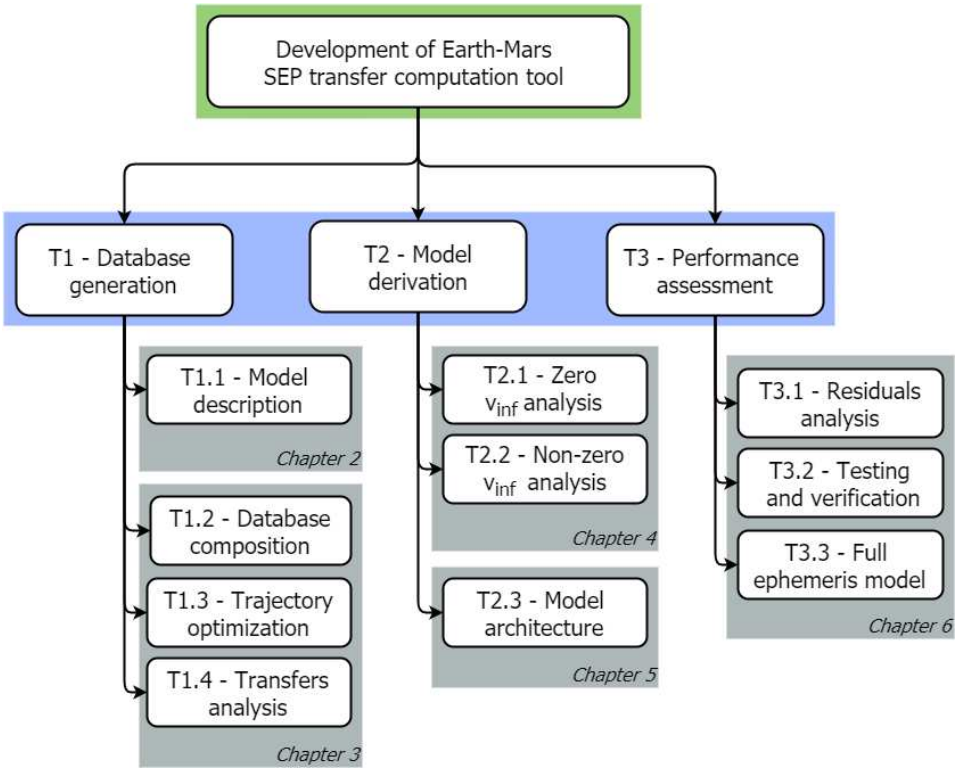

Figure 1.2: Work Breakdown Structure for the MSc thesis project.

2

Theoretical Background

While the selection of the target and of the technology of interest is considered part of the problem statement, as it follows from analysis of the motivation and context for the present research, the choices related to models and methods used originate from a thorough study of the underlying theory. This study has been extensively documented in the related literature survey [Galletti, 2017], the main findings of which are reported in the present chapter, adequately revised and commented in the light of what has been found when carrying out the project. Two main topics are addressed. In Section 2.1, the mathematical models used to describe the transfers are specified, while in Section 2.2, the methods applied to optimize the transfers are introduced.

2.1. Problem Formulation

The description of the motion of a spacecraft through its interplanetary journey requires the definition of a suitable reference frame and coordinate system for proper representation of its state vector, as well as the identification of the most appropriate formulation of the equations of motion that determine the evolution of such state vector. All these aspects related to the modelling of the trajectory design problem are addressed in Subsection 2.1.1. However, the mathematical description of a transfer is not restricted to the dynamical environment, but it must include a model for the system itself, which is the subject of Subsection 2.1.2. It is pointed out that the considerations presented in the current section account for a twofold analysis. On the one hand, the inventory and assessment of models that was conducted before the start of the research project. On the other hand, the availability of functionalities already implemented in the software tools to be used (DITAN) together with the time needed to implement and test custom ones.

2.1.1. Astrodynamics

The main reference for the writing of the following paragraphs is the theoretical background in [Wakker, 2015], to which the reader is recommended for the definition of common astronomical concepts.

State Vector Representation

This research being concerned with the interplanetary phase of Earth-Mars transfers, when the spacecraft is outside the sphere of influence of the planets, the heliocentric reference frame is adopted for the description of the motion. In this frame, the Sun corresponds to the origin of the axes and the ecliptic plane represents the XY-reference plane, as shown in Figure 2.1. The $+Z$-axis thus identifies the ecliptic north pole on the celestial sphere. The $+X$-axis defines a reference direction with respect to the celestial sphere, which is typically the vernal equinox. Finally, the $+Y$-axis lies in the ecliptic and is chosen to form a right-handed frame [Wakker, 2015]. Specifically, the mean J2000 ecliptic plane is used in this case as reference plane [Vasile, 2009].

Position and velocity of a spacecraft in the heliocentric reference frame are uniquely defined by six parameters, which are represented by a set of coordinates or orbital elements. Both can be expressed in several ways, which have been considered and compared to the capabilities of the software, as outlined in [Vasile, 2009]. For the analysis of planar transfers between circular orbits, use of a planar coordinates system would certainly simplify the formulation of boundary conditions. However, DITAN allows the use of polar coordi-

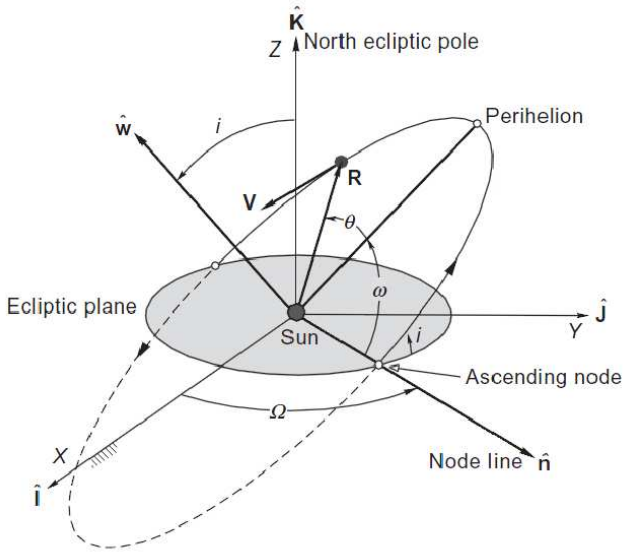

Figure 2.1: Motion of a spacecraft or celestial body in the heliocentric reference frame [Curtis, 2013].

nates only for a specific dynamic model, with constant acceleration, which is not the case for SEP . For this reason Cartesian coordinates have been adopted, which are easily implemented for planar transfers as they decouple in-plane and out-of-plane motion as well. Moreover, they are already available in the software and compatible with any dynamical model without the need for any modification to the source code.

It is worth mentioning that in this study the state vector is composed in fact of a total of seven elements, since the mass is included on top of the six Cartesian coordinates that have been mentioned.

Dynamical model

The general form of the equations of motion in the full dynamical model is widely known as in Equation 2.1:

$$\frac{d\vec{x}}{dt} = \frac{d}{dt}\begin{bmatrix}\vec{r}\\ \vec{v}\end{bmatrix} = \begin{bmatrix}\vec{v}\\ \vec{a}_{tot}\end{bmatrix} = \begin{bmatrix}\vec{v}\\ \vec{g}+\vec{f}_p\end{bmatrix} \tag{2.1}$$

It can be seen that the motion of the body is the result of two contributions: the central acceleration $\vec{g}$, that expresses the gravitational attraction of the main celestial body, and the perturbing acceleration $\vec{f}_p$, which accounts for all intended or unintended perturbing factors. Typically intended perturbing effects consist of the acceleration due to the thrust, while the unintended ones are the actual pertubations, among which the most relevant are the atmospheric drag, the non-spherical gravitational potential, the gravitational potential of celestial bodies other than the central one, and the solar radiation pressure.

With regard to the unperturbed motion of a spacecraft in a heliocentric orbit (i.e. $\vec{f}_p = \vec{0}$), the simplified dynamics of the two-body problem (2BP) applies. The simplification follows from the assumption that one body is significantly larger than the second one, under which the motion of this second body about the large one is described by Equation 2.2 [Wakker, 2015]:

$$\frac{d^2\vec{r}}{dt^2} = -\frac{\mu}{r^3}\vec{r} \tag{2.2}$$

where the approximation $\mu = G(m_1 + m_2) \approx Gm_1$ is introduced and μ represents the gravitational parameter of the massive body. The analytical solution of Equation 2.2 is the *conic section* described by Equation 2.3:

$$r = \frac{H^2/\mu}{1+e\cos\theta} = \frac{l}{1+e\cos\theta} \tag{2.3}$$

where H is the magnitude of the angular momentum (per unit mass), e the eccentricity, l the semi-latus rectum and θ the true anomaly.

As for the perturbed motion, an assessment has been carried out to determine the order of magnitude of each contribution during interplanetary cruise between Earth and Mars. Table 2.1 reports the magnitude of the perturbing accelerations for a spacecraft located halfway between Earth and Mars (1.25 AU from the Sun) that travels in a coplanar Solar System. Contributions include the acceleration caused by Earth, Mars, Jupiter, Moon, Earth's oblateness, atmospheric drag, radiation pressure and thrust of a typical SEP system (see Section B for the assumptions and the geometry used to produce Table 2.1). For reference purposes, the main acceleration due to the Sun attraction is also included.

Acceleration	***Description***	***Value*** [m/s^2]
$\vec{f}_{Sun}$	Sun attraction	3.8×10^{-4}
$\vec{f}_{Earth}$	Earth attraction	2.7×10^{-7}
$\vec{f}_{Mars}$	Mars attraction	3.0×10^{-8}
$\vec{f}_{Moon}$	Moon attraction	3.3×10^{-9}
$\vec{f}_{Jup}$	Jupiter attraction	1.5×10^{-7}
$\vec{f}_{drag}$	atmospheric drag	$<< 10^{-10}$
$\vec{f}_{J2}$	J2 effect (Earth)	$<< 10^{-10}$
$\vec{f}_{rad}$	radiation pressure	1.8×10^{-8}
$\vec{f}_{T}$	SEP thrust	10^{-4}

Table 2.1: List of perturbing acceleration and their magnitude.

A difference of several orders of magnitude exists between the effect of the Sun and any pertubation, although they have been computed in the worst-case scenario, with the obvious exception of the thrust that has a significant impact. This justifies, for the preliminary design of the transfers, the adoption of a two-body dynamical model in which the thrust represents the only perturbing force.

Propulsive force

The simplified equations of motion that follow from the preceding analysis are those of Equation 2.4:

$$\frac{d^2\vec{r}}{dt^2} = -\frac{\mu}{r^3}\vec{r} + \vec{f}_T = -\frac{\mu}{r^3}\vec{r} + \frac{\vec{T}}{m} \tag{2.4}$$

The propulsive force $\vec{T}$ generated by the system is determined by the mass flow rate $\dot{m}_p$ of the expelled gas, the expulsion velocity $\vec{v}_e$, the pressure at the nozzle exit area p_e, the external pressure p_{amb} and the exit surface vector $\vec{A}_e$[1], by means of Equation 2.5:

$$\vec{T} = -\dot{m}_p \vec{v}_e + (p_e - p_{amb})\vec{A}_e \tag{2.5}$$

In order to eliminate the pressure term, the effective exhaust velocity c_e or specific impulse $I_{sp,e}$ are typically used instead, as defined in Equation 2.6. Although the specific impulse is also an effective value, for ease of notation $I_{sp,e}$ is reduced to I_{sp} in the remainder of this report.

$$T = \dot{m}_p c_e = \dot{m}_p g_0 I_{sp} \tag{2.6}$$

Equation 2.6 leads to the derivation of the last equation of the system, that governs the evolution of the mass:

$$\dot{m} = -\dot{m}_p = -\frac{T}{g_0 I_{sp}} \tag{2.7}$$

[1]The exit surface vector $\vec{A}_e$ is defined as the vector of magnitude equal to the exit surface area A_e and direction normal to such surface.

Dynamical equations

In conclusion, a simplified dynamic environment has been adopted to describe Earth-Mars transfers, which is summarized in Equations 2.8 to 2.10:

$$\frac{d\vec{r}}{dt} = \vec{v} \tag{2.8}$$

$$\frac{d\vec{v}}{dt} = -\frac{\mu}{r^3}\vec{r} + \frac{\vec{T}}{m} \tag{2.9}$$

$$\frac{dm}{dt} = -\frac{T}{g_0 I_{sp}} \tag{2.10}$$

It can be noticed that Equations 2.8 to 2.10 still refer to full 3D model dynamics. The restriction to planar transfers between coplanar circular orbits has been achieved by the formulation of proper boundary conditions, which is described in detail in Section 3.2.

2.1.2. Propulsion System

The system parameters that are relevant to the transfer design problem are those related to its propulsion system, as it provides the propulsive force that modifies the trajectory. The complete propulsion system model is composed of two elements: the thruster model and the power supply model, which in the case of SEP is based on solar arrays. In the following the formulas that are relevant to the mathematical description of both are first introduced separately and then combined.

Power Supply Model

In SEP technology, the electric power generation system is based on solar cells, which convert the incoming solar energy into electrical energy. The generation thus depends on the availability of incoming solar power, which in turn follows from the Sun-spacecraft distance. At heliocentric distance r_{AU} (measured in AU), the solar flux is derived from the solar constant $W_{1,AU}$ by means of Equation 2.11 [Lissauser and de Pater, 2013]:

$$W = \frac{W_{1,AU}}{r_{AU}^2} \tag{2.11}$$

where $W_{1,AU} = 1366\ \mathrm{W/m^2}$ is defined conventionally as the mean solar irradiance at a distance of one astronomical unit [Lissauser and de Pater, 2013]. Accordingly, given a solar panel surface A and having defined the total received solar power at 1 AU as $P_0 = W_{1,AU} A$, the total incoming power at arbitrary heliocentric distance r follows from Equation 2.12:

$$P_{in} = P_0 \left(\frac{r_0}{r}\right)^2 \tag{2.12}$$

Given the imperfections of the power conversion process, the corresponding generated electrical power depends on an efficiency factor, introduced in Equation 2.13 as η_{SP}, whose value can be up to 30% for current space-qualified technology [Fatemi et al., 2005].

$$P_{SP} = \eta_{SP} P_{in} = \eta_{SP} P_0 \left(\frac{r_0}{r}\right)^2 \tag{2.13}$$

Options exist other than the use of a constant efficiency factor for the effective representation of how the available power decays, among which the adoption of a variable efficiency factor that accounts for degradation of the solar arrays, or the adjustment of the exponent of the power loss law. These options have been compared in an assessment that is fully documented in Section B. It has been concluded that for the requirements of the intended application, the inverse-square law has sufficient accuracy for Earth-Mars transfers, while preserving the simplicity of the relation. The effective input power generated by the solar arrays P_{SP} is provided to the propulsion system (specifically to the power processor unit, PPU) as well as to the spacecraft bus:

$$P_{SP} = P_{SC} + P_{PPU} \quad \Rightarrow \quad P_{PPU} = \eta_{SC} P_{SP} \tag{2.14}$$

The flowchart in Figure 2.2 depicts the power distribution process to the PPU and the spacecraft bus.

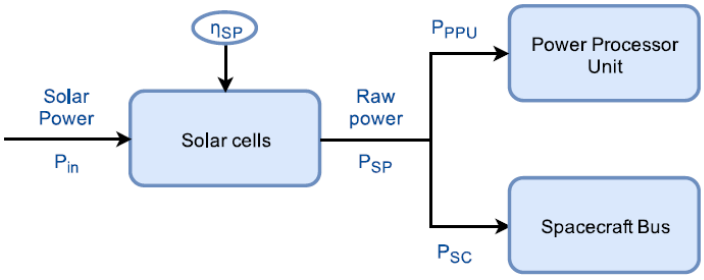

Figure 2.2: Solar power conversion process and distribution to the system.

Thruster Model

Due to the conditioning and the transformations carried out by the PPU to convert electrical input power into thruster input power, a factor is introduced to account for this effect:

$$P_T = \eta_{PPU} P_{PPU} \tag{2.15}$$

Besides the losses due to the efficiency of the PPU η_{PPU}, some more losses are associated with the electrical efficiency η_e, which accounts for the energy used for the ionization and acceleration process:

$$P_j = \eta_e P_T \tag{2.16}$$

In Equation 2.16, P_j is the effective beam power. From a different perspective, this is the power required for acceleration of the propellant mass flow to the exhaust velocity, as shown in Equation 2.17 [Ohndorf, 2016]:

$$P_j = \frac{1}{2}\dot{m}_p c_e^2 = \frac{1}{2} T c_e = \frac{1}{2} T g_0 I_{sp} \tag{2.17}$$

The flowchart in Figure 2.3 depicts the power conversion process from power source to thrust beam.

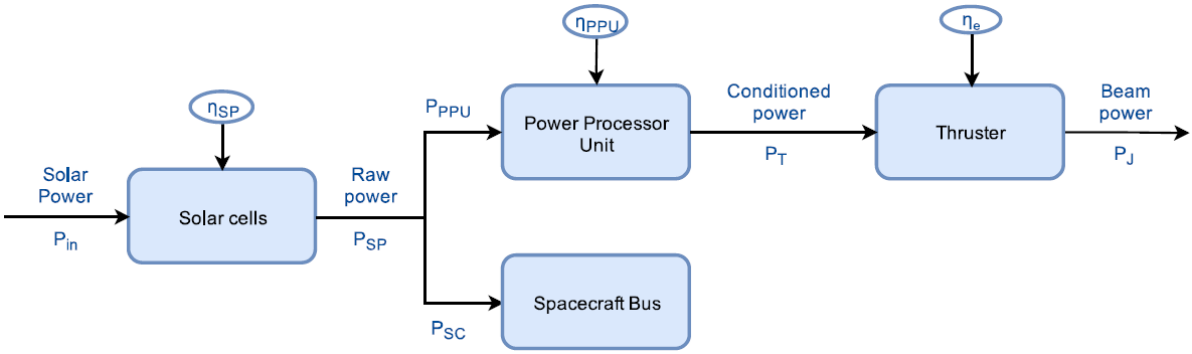

Figure 2.3: Power conversion process from power source to thrust beam.

The combination of Equations 2.15, 2.16 and 2.17 yields an important relation between the three key parameters of electric propulsion systems: thrust (T), input power (P_{PPU}) and specific impulse (I_{SP}). Keeping in mind that $T = \dot{m}_p c_e$, this relation is expressed by Equation 2.18:

$$T = \frac{2\eta_e \eta_{PPU}}{g_0} \frac{P_{PPU}}{I_{sp}} \qquad \dot{m}_p = \frac{2\eta_e \eta_{PPU}}{g_0^2} \frac{P_{PPU}}{I_{sp}^2} \tag{2.18}$$

Since the systems of interest have constant specific impulse and the efficiency factors are considered constant as well, Equation 2.18 can be further combined with Equations 2.13 and 2.14 and the inverse-square law turns out to be valid not only for the available power, but also for the available thrust. If one defines the overall efficiency of the system $\eta = \eta_e \eta_{PPU} \eta_{SC} \eta_{SP}$, Equation 2.18 becomes:

$$T = \frac{2\eta}{g_0 I_{sp}} \frac{P_0}{r_{AU}^2} \qquad \dot{m}_p = \frac{2\eta}{g_0^2 I_{sp}^2} \frac{P_0}{r_{AU}^2} \tag{2.19}$$

2.2. Low-Thrust Transfers Optimization

Trajectory optimization is a dynamic optimization problem which is concerned with a system of non-linear differential state equations and aims at the minimization of a defined objective function, subject to a number of dynamic constraints and initial and terminal boundary conditions. The suitability of a specific optimization technique to the solution of the problem depends on multiple factors, including the accuracy required, the dimension of the search space and the properties of the performance index to be optimized. As it has been mentioned, an existing piece of software is used to generate optimal transfers. The choice was done in the light of the capabilities of the method that is implemented as well as of the many functionalities of the tool, which can handle a great variety of models and constraints and can deal with the different stages of the trajectory design problem, from guess generation to solution refinement. The purpose of this section is the introduction of the concepts on which the software optimization tool is based. They are extensively discussed in [Bernelli Zazzera et al., 2002], which is used as a reference for the coming paragraphs.

2.2.1. Optimal Control Problem

The differential equations that describe the dynamic model, subject of Subsection 2.1.1, are summarized in Equation 2.20:

$$\dot{\vec{x}} = \vec{f}[\vec{x}(t), \vec{u}(t), t] \qquad t_0 \le t \le t_f \tag{2.20}$$

where vectors $\vec{u}(t)$ and $\vec{x}(t)$ represent respectively the vector of control variables and the vector of state variables. The performance of the system is measured and represented by a functional J of the form:

$$J[\vec{x}, \vec{u}, t_f] = \phi(\vec{x}, \vec{u}, t)\Big|_{t_0}^{t_f} + \int_{t_0}^{t_f} L[\vec{x}, \vec{u}, t]\,dt \tag{2.21}$$

For a complete description of the problem, it is also necessary to specify the constraints to which state and control variables are subjected and the boundary conditions that should be satisfied, as in Equation 2.22:

$$\vec{G}(\vec{x}(t), \vec{u}(t), t) \ge 0 \quad [t_0 \le t \le t_f] \qquad \vec{\psi}(\vec{x}(t_0), \vec{x}(t_f), t_f) = 0 \tag{2.22}$$

The statement of the optimal control problem is equivalent to require that for the optimal control $\vec{u}^*$ Equation 2.23 holds:

$$J^* = \phi(\vec{x}^*, \vec{u}^*, t)\Big|_{t_0}^{t_f^*} + \int_{t_0}^{t_f^*} L[\vec{x}^*, \vec{u}^*, t]\,dt \le \phi(\vec{x}, \vec{u}, t)\Big|_{t_0}^{t_f} + \int_{t_0}^{t_f} L[\vec{x}, \vec{u}, t]\,dt \tag{2.23}$$

Having defined the augmented performance index $\tilde{J}$:

$$\tilde{J} = \left[\phi + \vec{\nu}^T\vec{\psi}\right]_{t_0}^{t_f} + \int_{t_0}^{t_f}\left[L(\vec{x}, \vec{u}, t) + \vec{\lambda}^T(\vec{f} - \dot{\vec{x}}) + \vec{\mu}^T\vec{G}\right]dt \tag{2.24}$$

the optimality conditions are derived by looking for stationary points of $\tilde{J}$ [Bernelli Zazzera et al., 2002]. For convenience, the Hamiltonian H and auxiliary function Φ are defined:

$$H = L(\vec{x}, \vec{u}, t) + \vec{\lambda}^T\vec{f}(\vec{x}, \vec{u}, t) + \vec{\mu}^T\vec{G}(\vec{x}, \vec{u}, t) \tag{2.25}$$

$$\Phi = \phi(\vec{x}_0, \vec{x}_f, t_f) + \vec{\nu}^T\vec{\psi}(\vec{x}_0, \vec{x}_f, t_f) \tag{2.26}$$

Because of the introduction of the multiplier functions $\vec{\lambda}$ that appear in the augmented performance index $\tilde{J}$, the size of the dynamical system is doubled, resulting in the adjoint equations Equation 2.28. By setting the variations $\delta\tilde{J}$ to zero, the complete set of necessary conditions (differential-algebraic equations) follows:

$$\dot{\vec{x}} = \left(\frac{\delta H}{\delta\vec{\lambda}}\right)^T = \vec{f}(\vec{x}, \vec{u}, t) \tag{2.27}$$

$$\dot{\vec{\lambda}} = -\left(\frac{\delta H}{\delta\vec{x}}\right)^T = -\left(\frac{\delta L}{\delta\vec{x}}\right)^T - \left(\frac{\delta\vec{f}}{\delta\vec{x}}\right)^T\vec{\lambda} - \left(\frac{\delta\vec{G}}{\delta\vec{x}}\right)^T\vec{\mu} \tag{2.28}$$

$$\left(\frac{\delta H}{\delta\vec{u}}\right)^T = \left(\frac{\delta L}{\delta\vec{u}}\right)^T + \left(\frac{\delta\vec{f}}{\delta\vec{u}}\right)^T\vec{\lambda} + \left(\frac{\delta\vec{G}}{\delta\vec{u}}\right)^T\vec{\mu} = 0 \tag{2.29}$$

$$\vec{\lambda}(t_f) = \Phi_x^T = \left(\frac{\delta\phi}{\delta\vec{x}} + \vec{\nu}^T\frac{\delta\vec{\psi}}{\delta\vec{x}}\right)^T\Big|_{t=t_f} \tag{2.30}$$

$$(\Phi_t + H)\big|_{t=t_f} = 0 \tag{2.31}$$

2.2.2. Direct Transcription with FET

Calculus of variations (COV) is the classical theory that deals with trajectory optimization problems and enables the derivation of necessary conditions for optimality. As the resulting problem is typically difficult to solve, numerical approaches are normally used to handle it, which, generally speaking, can be divided into two types: direct and indirect. Indirect methods are those that, starting from COV, use the optimality conditions to solve a dynamical system of double size, due to the addition of the adjoint equations. Direct methods, instead, parameterize the continuous problem to a finite-dimensional non-linear programming problem (NLP) [Conway, 2010]. A comprehensive description and analysis of both approaches is provided by [Betts, 1998].

The core algorithm of the software that has been used (DITAN, Direct Interplanetary Trajectory Analysis) belongs to the latter category and is based on a direct collocation technique using finite elements in time [Bernelli Zazzera et al., 2002]. The general logic behind using direct transcription to solve trajectory optimization problems consists in translating the original optimal control problem into a NLP problem, made up by a number of non-linear algebraic equations and one objective function. This can be subsequently solved with a general optimizer. For a software using direct transcription by finite elements in time (DFET), the logic of the overall process therefore looks like in Figure 2.4.

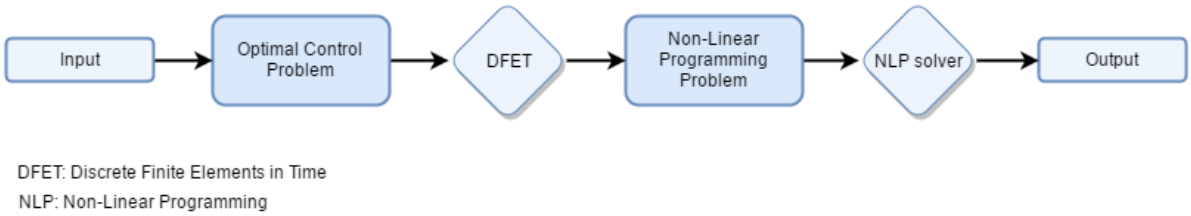

Figure 2.4: Logic of software employing direct finite elements transcription [Bernelli Zazzera et al., 2002].

The method implemented by DFET consists of the following phases [Bernelli Zazzera et al., 2002]:

1. The general trajectory optimization problem is decomposed into M phases (either parallel or sequential), each phase divided into N finite time elements;
2. The optimization problem is stated on each phase j, thus identifying an objective function J^j, dynamic equations $\dot{\vec{x}} = \vec{f}^j$, constraints $\vec{G}^j \geq 0$ and boundary conditions $\vec{\psi}^j \geq 0$ (including inter-phase links);
3. In each element, state and control variables are parameterized by means of polynomial basis functions;
4. On each phase j, the problem is first formulated in the weak (integral) form and subsequently discretized by means of quadrature-sums at Gauss points;
5. A set of non-linear algebraic equations is derived that compose the NLP problem.

The features and the formulation of the NLP problem are summarized in Figure 2.5, in comparison with the original optimal control problem.

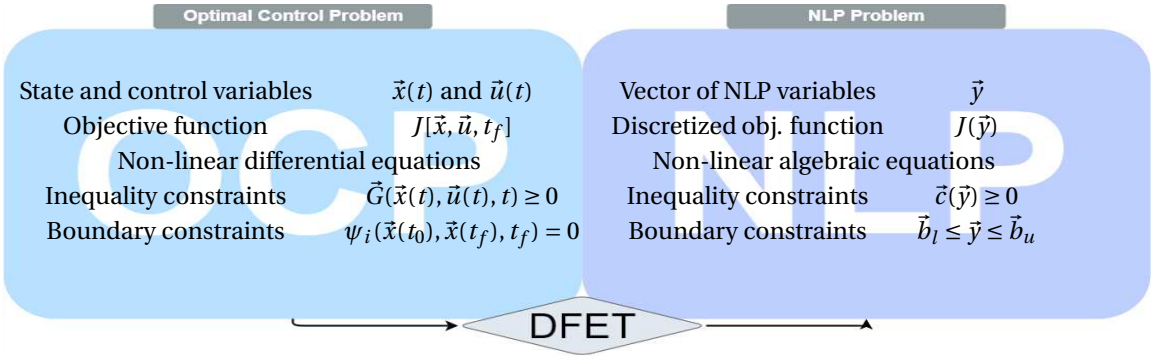

Figure 2.5: Formulation of the original optimal control problem vs. non-linear programming problem [Bernelli Zazzera et al., 2002].

3

Database Generation and Characterization

The generation of the quantitative data constitutes a fundamental part of the research since it determines the composition and structure of the dataset in terms of characteristics of the transfers included and of the variables used to describe them. These aspects have a strong impact on the capabilities of the tool that is the outcome of this study, since they define what type of transfers it will be able to model, and by means of what parameters. The purpose of the present chapter is to describe in sufficient detail what choices were made and why during the generation of the database of trajectories, as well as to draw conclusions from the characterization of the optimized transfers. In Section 3.1 the decisions taken during the setup of the database are addressed. Section 3.2 focuses on the implementation aspects of the actual data generation, including the verification of the SW tools and the automation of the optimization process. Attention is also given to the numerical and practical issues encountered, which have provided an insight into the problem that was essential to tune the process and to produce meaningful results. Lastly, in Section 3.3, preliminary considerations about the produced transfers are drawn, which are crucial to introduce the analysis of Chapter 4.

3.1. Database Composition

Several factors have contributed to the eventual structure and composition of the database of trajectories, the most significant ones being illustrated in the following. With structure and composition of the database, it is referred to the types of trajectories the database contains, their number, the objective function that is optimized, the variables that are free to vary, those that are fixed, *et cetera*. First of all, an extensive survey of the recent literature identified where interesting trends could be found that could be best analyzed by a curve-fitting method. It also indicated what existing models could be improved and/or extended and what other possibilities had not yet been explored, as summarized in Chapter 1. Secondly, applicability in the frame of the early design stages of real missions was considered. In this regard, staying in an operational environment for most of the duration of the project significantly enhanced insight into requirements and relevant aspects of such studies. Lastly, the practicability of studying the different transfer options was taken into account: computations were run only after making sure that the available software tools would provide reliable results in a limited amount of time. Cases for which the effort required to set up and complete the optimization was significantly outweighing the effort of the data modelling were limited as much as possible.

3.1.1. Objective Function

The first choice to be made is concerned with the selection of the type of transfers that are to be included in the dataset. For interplanetary low-thrust transfers, those trajectories are typically of interest that make use of low propellant mass and/or enable reaching the target in a realistically short time. One could therefore decide to optimize the propellant mass, either for free or fixed transfer time, or the time of flight [1]. Given the fact that, for real applications, minimization of the ΔV cost is the priority, final mass has been selected as objective function. Moreover, in line with the rationale specified above, implementation aspects were considered at

[1] While mass-optimal transfers can be very long and time-optimal transfers can achieve very high ΔV cost, fixing the transfer time and optimizing the propellant mass represents a simple way of conducting a trade-off between mass and time, by evaluating the ΔV impact of reducing the flight time compared to mass-optimal free-time transfers.

this stage. Given the large number of transfers that are to be derived, these should not be optimized one by one, but by automating a continuation problem. In this regard, it is important to point out that DITAN is in general not able to jump from one family of transfers to another, for example with a different number of revolutions. Therefore, the way the continuation problem is set up (that is to say, what initial guess is used at each step) significantly affects the class of optimal transfers that are found. In conclusion, it was decided to produce first a set of minimum-time transfers, which are easily optimized from propagated continuous tangential thrust solutions. These are then used as initial guess for the mass-optimal transfers. With this setup, mass-optimal transfers are found that have the same number of revolutions as the corresponding time-optimal solutions, which limits the transfer times to reasonably short values.

3.1.2. Variables Selection

Following the formulation of the problem described in Section 2.1 and the selection of the objective function, it is possible to proceed to the definition of the design space to be investigated, with regard to:

1. identification and categorization of the main design drivers and relevant variables;
2. selection of input/output parameters;
3. definition of the variation ranges for the input parameters;
4. iterative adjustment of ranges depending on preliminary analysis of the results.

Figure 3.1 visualizes the outcome of points 1 and 2 by displaying a list of the main model variables, their classification into inputs/outputs as well as into the following groups: geometric parameters, transfer-specific parameters and system parameters. Below, characteristics and ranges of interest of each variable are described.

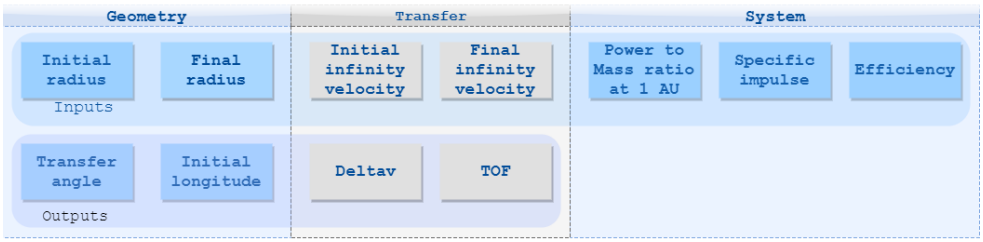

Figure 3.1: Summary of the selected input/outputs parameters.

Inputs: Geometric Parameters

Since the analysis is restricted to circle-to-circle planar transfers, the only relevant geometric parameters that affect the model are initial and final orbit radii. As the aim of this study is not only the derivation of the full Earth-Mars model, but also the identification of an effective methodology that allows quick extension of such a model to other destinations, it has been decided to keep those variables under the label of relevant input parameters. However, for all the practical computations that are reported in the remaining of this report, initial and final radii are fixed and correspond to the mean semi-major axes of the Earth and of Mars orbit.

Inputs: Transfer Parameters

Departure and arrival infinity velocities have non-zero values for several missions of practical meaning. The initial infinity velocity is related to the launcher performance and achieved either by direct escape or by using coast arcs or parking orbits. As for the conditions at arrival, it should be mentioned that typically the thrust provided by SEP systems is too low for capture to Mars if the relative speed is significant. Therefore, final infinity velocity close to zero is needed if the same low-thrust engine is used for transfer and capture, or a separate high-thrust engine becomes necessary [Biesbroek, 2016]. In order not to lose generality, non-zero values for the arrival infinity velocity are accounted for, which also enables future extension of the model to multiple-leg missions. The range for the variation of the infinity velocity, both at departure and at arrival, is selected by looking at the burns of the Hohmann transfer, since transfers for which the initial/final velocity is smaller than the corresponding Hohmann burn are considered most meaningful. The ΔV of the Hohmann transfer to Mars orbit amounts to 5.594 km/s, split into two burns of 2.945 and 2.649 km/s (Section A).

For simplicity, both initial and final velocities are allowed to vary within the same range, specifically from 0 to 2 km/s.

Inputs: System Parameters

The mathematical modelling of the propulsion system carried out in Subsection 2.1.2 has identified four parameters that have an impact on its performance: initial mass m_0, power at 1 AU P_0, specific impulse I_{sp} and propulsion system efficiency η. They define the maximum thrust-to-mass ratio at 1 AU a_0 as in Equation 3.1:

$$a_0 = \frac{T_0}{m_0} = \frac{2\eta}{g_0 I_{sp}} \frac{P_0}{m_0} \tag{3.1}$$

The thrust-to-mass ratio is the system parameter on which the thrust profile and thus the transfer characteristics depend. Equation 3.1 shows that in terms of thrust-to mass-ratio independent variations of I_{sp}, P_0, m_0 and η are equivalent to varying only one parameter while keeping the other three fixed. However, the thrust-to-mass ratio is not comprehensive of all aspects of the propulsion system. For transfers with the same thrust-to-mass ratio at 1 AU, different values of the specific impulse result in distinct propellant masses. For this reason, it is decided to fix two of the four aforementioned system parameters (efficiency and initial mass) and to vary specific impulse and power at 1 AU. To conclude, the following choices have been made after surveying currently available technology:

- **Propulsion system efficiency**: a constant value of 0.65 is assumed;
- **Specific impulse**: it is varied within the range 1500 to 5000 s;
- **Initial mass**: a constant value of 1000 kg is assumed;
- **Power at** 1 AU: it is varied within the range 4 to 20 kW.

Outputs Parameters

As we are looking into mass-optimal trajectories, choosing the ΔV as most relevant performance parameter follows naturally. An estimate for the propellant mass is in fact easily derived from the ΔV, and there is no need to model it independently. The time of flight is let free to vary, and it is therefore another key output of the optimization in such cases. Finally, it is important to have insight in the geometry of the transfers in terms of initial and final longitudes, and as a result determine the departure and arrival dates. For this to be achieved, the problem of the phasing with Mars should be solved. As explained in detail in Section 5.1, departure and arrival dates can be analytically derived if transfer time and angle are known. Therefore, the transfer angle is selected as third parameter to be modelled by curve fitting. In Figure 3.1, the initial longitude is listed as output to show that phasing with Mars is also included in the modelling tool.

Table 3.1 shows a summary of the variables introduced above and of their characteristics. It refers to power-to-mass ratio, which will be used in the remaining part of the report, instead of to the two distinct variables.

Variable	Symbol	Unit	Type	I/O	Value	Vector
Initial Radius	r_i	[AU]	Geometry	I	Fixed	1
Final Radius	r_f	[AU]	Geometry	I	Fixed	1.524
Initial Infinity Velocity	$v_{\infty,i}$	[km/s]	Transfer	I	Varied	0-2
Final Infinity Velocity	$v_{\infty,f}$	[km/s]	Transfer	I	Varied	0-2
P/m at 1 AU	P_0/m_0	[W/kg]	System	I	Varied	4-20
Specific Impulse	I_{sp}	[s]	System	I	Varied	1500-5000
Efficiency	η	-	System	I	Fixed	0.65
Transfer Angle	θ_t	[◦]	Geometry	O	-	-
Initial Longitude	θ_0	[◦]	Geometry	O	-	-
Time of Flight	TOF	[days]	Transfer	O	-	-
Deltav	ΔV	[km/s]	Transfer	O	-	-

Table 3.1: List of the main design drivers and transfer performance parameters, divided into geometry, transfer and system parameters.

3.1.3. Database Structure

For each of the ranges identified in the previous section, a discretization that aims at capturing a sufficient number of intermediate points between the chosen lower and upper boundaries, without making the overall computational effort too heavy, was selected. Discretization is needed with regard to power-to-mass ratio, specific impulse and infinity velocity.

System Parameters

The discrete values adopted for the system parameters power-to-mass ratio and specific impulse are:

$$\overrightarrow{P/m}|_0 = \begin{bmatrix} 4 & 8 & 12 & 16 & 20 \end{bmatrix} \text{W/kg} \tag{3.2}$$

$$\overrightarrow{I_{sp}} = \begin{bmatrix} 1500 & 2667 & 3833 & 5000 \end{bmatrix} \text{s} \tag{3.3}$$

Acceptance of these discrete values was done after checking that the corresponding values of the initial thrust cover the entire range of interest and are fairly distributed over it. As shown in Figure 3.2 and Equation 3.4, the thrust vector covers the range 106 to 1768 mN (initial mass is always fixed at 1000 kg), which is comprehensive of currently employed technology for such missions.

$$\begin{aligned} \vec{T}_0 = \begin{bmatrix} 0.106 & 0.138 & 0.199 & 0.212 & 0.277 \\ 0.318 & 0.354 & 0.398 & 0.415 & 0.424 \\ 0.530 & 0.553 & 0.597 & 0.692 & 0.707 \\ 0.795 & 0.994 & 1.061 & 1.414 & 1.768 \end{bmatrix} \text{N} \end{aligned} \tag{3.4}$$

The distribution over this range is more dense in the lower part ($T_0 < 0.8$ N), which is considered to be a positive factor since in this interval variations of the performance parameters are faster, as it is shown in Section 3.3. Moreover, the number and distribution of samples in the range $T_0 > 0.8$ N also allow reliable analysis of the trends in this region.

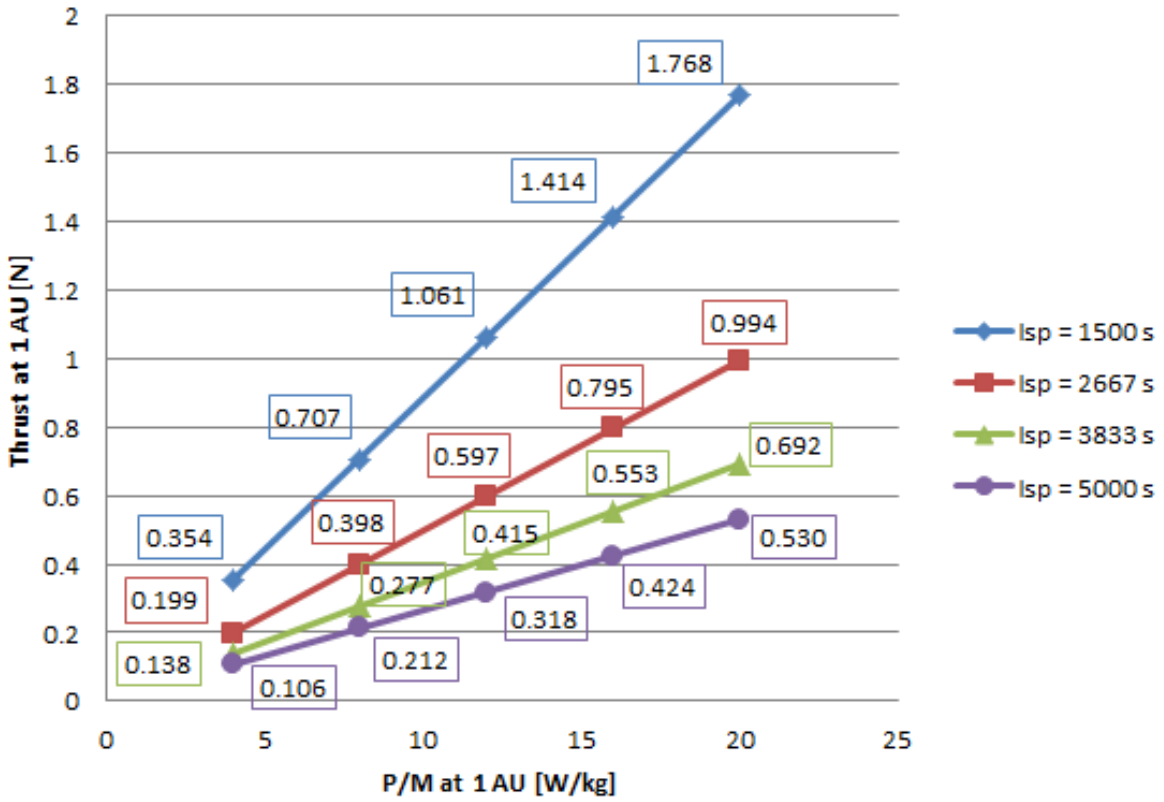

Figure 3.2: Visualization of the discrete values of the thrust at 1 AU in relation to P/m at 1 AU and I_{sp}.

Infinity Velocity

The discretization used in the beginning for the infinity velocity vectors proposed three discrete values of 0, 1 and 2 km/s at each end, resulting in nine possible combinations of departure/arrival infinity velocity. However, a preliminary analysis of the results showed that a densification was required, which increased the number from nine to 24 possible combinations. The reasons and the logic of such densification are related to the specific trends which were found, and will be explained in detail in Section 4.2. For the time being, it is anticipated that for those trends to be captured both a smaller step size and the exploration of specific regions of the design space were needed. In terms of step size, the densification resulted in 10 discrete values, instead of three, which are listed in Equation 3.5:

$$\vec{v}_\infty = \begin{bmatrix} 0 & 0.125 & 0.25 & 0.5 & 0.75 & 1 & 1.25 & 1.5 & 1.75 & 2 \end{bmatrix} \text{km/s} \tag{3.5}$$

Although considering all possible combinations would produce 100 $(v_{\infty,i}, v_{\infty,f})$ couples, only 24 have been included in the database, the reason being the exploration and analysis of specific trends. As a result of these considerations, which are the subject of Section 4.2, all the pairs of the type $v_{\infty,i} = v_{\infty,f}$ were considered (10 couples). Moreover, 14 additional combinations were taken into account, for which $v_{\infty,i} \neq v_{\infty,f}$, according to the following logic:

- three combinations for which: $v_{\infty,i} + v_{\infty,f} = 0.25$ km/s;
- five combinations for which: $v_{\infty,i} + v_{\infty,f} = 1$ km/s;
- five combinations for which: $v_{\infty,i} + v_{\infty,f} = 2$ km/s;
- five combinations for which: $v_{\infty,i} + v_{\infty,f} = 3$ km/s.

The distribution of the selected couples is visualized in Figure 3.3, over the 10×10 full matrix.

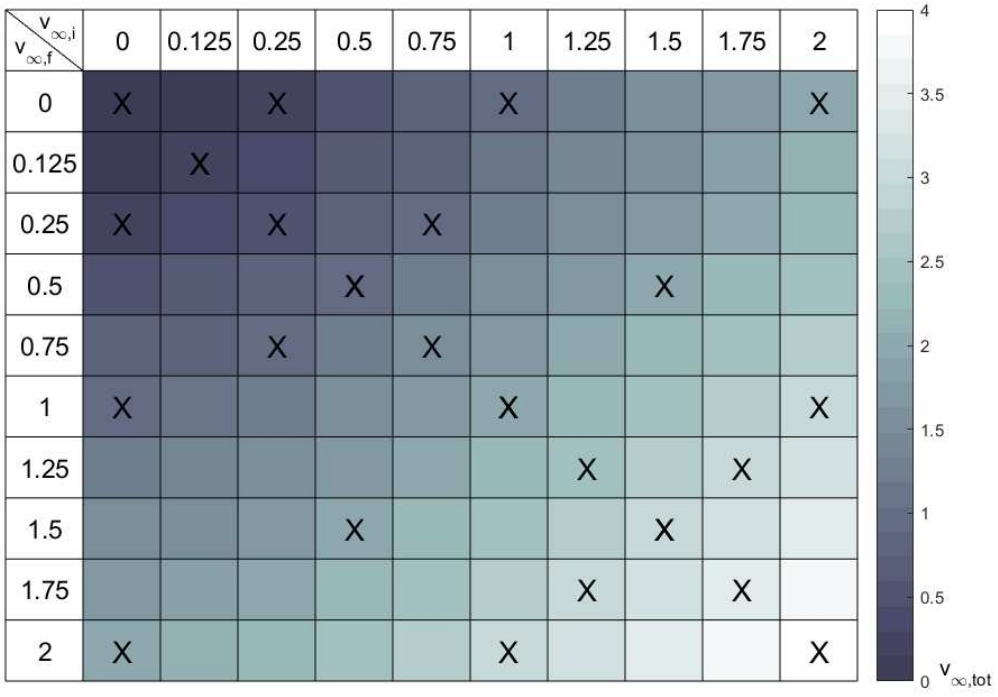

Figure 3.3: The pattern of the selected $(v_{\infty,i}, v_{\infty,f})$ couples is highlighted. The combinations of interest are marked with an 'X', while the colour scale refers to the values of $v_{\infty,tot}$ $(= v_{\infty,i} + v_{\infty,f})$. It is pointed out that the $(v_{\infty,i}, v_{\infty,f})$ pairs for which $v_{\infty,i} \neq v_{\infty,f}$ correspond to specific values of $v_{\infty,tot}$, resulting in the pattern shown, and in its symmetry.

For the 24 cases of Figure 3.3, $(v_{\infty,i}, v_{\infty,f})$ couples are reported in Table 3.2. All values are in km/s.

Family	**#1**	**#2**	**#3**	**#4**	**#5**	**#6**	**#7**	**#8**	**#9**	**#10**	**#11**	**#12**
$v_{\infty,i}$	0	0.25	0.125	0	0.25	1	0.75	0.5	0.25	0	0.75	2
$v_{\infty,f}$	0	0	0.125	0.25	0.25	0	0.25	0.5	0.75	1	0.75	0

Family	**#13**	**#14**	**#15**	**#16**	**#17**	**#18**	**#19**	**#20**	**#21**	**#22**	**#23**	**#24**
$v_{\infty,i}$	1.5	1	0.5	0	1.25	2	1.75	1.5	1.25	1	1.75	2
$v_{\infty,f}$	0.5	1	1.5	2	1.25	1	1.25	1.5	1.75	2	1.75	2

Table 3.2: Discrete values of departure and arrival infinity velocities of the 24 families of transfers that are produced.

Database Composition

In conclusion, the choices that have been made translate into $5 \times 4 \times 24 = 480$ distinct combinations of input parameters, each corresponding to an optimal solution to the transfer problem. In order to make the reading more clear, the future usage of a number of terms is introduced here:

- the term ***transfer*** is used to refer to a specific setup (i.e. combination of inputs);
- a ***family*** groups all the transfers which have the same values of initial and final infinity velocities (simultaneously), with any arbitrary combination of system parameters $(P/m\big|_0, I_{sp})$;
- a ***group*** brings together all the transfers that have the same value of total infinity velocity (as in infinity velocity at departure plus infinity velocity at arrival).

Therefore the 480 transfers that are derived are arranged into 24 families and 10 groups, as in Figure 3.4.

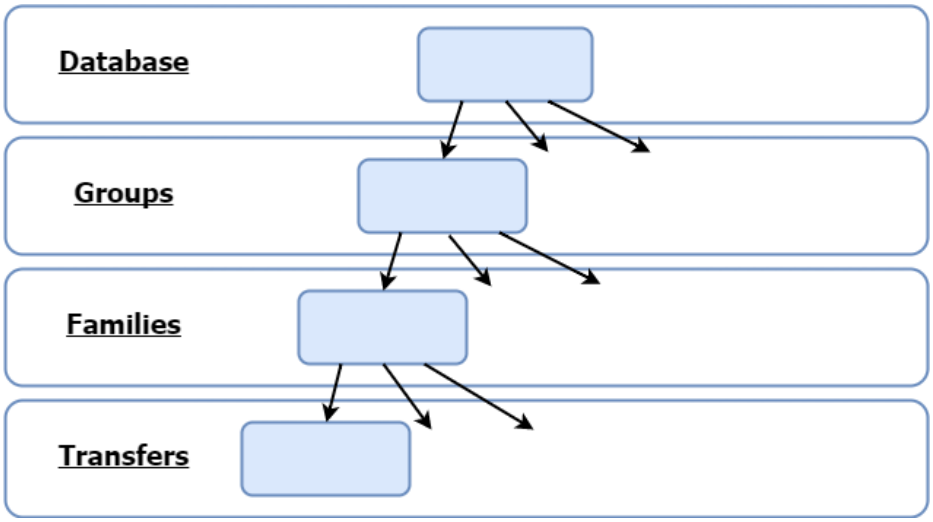

Figure 3.4: Representation of the layers of the database of transfers.

3.2. Implementation Aspects

From an operational point of view, the generation of the database has been achieved by using existing software in combination with *ad hoc* developed functions and scripts. Both elements are dealt with in the present section. Subsection 3.2.1 concerns itself with explaining how the existing piece of software has been used to implement the setup described in the previous sections. Verification of such implementation, but also of the SW tool in general, is addressed in Subsection 3.2.2. At last, Subsection 3.2.3 provides details into how the entire optimization process was automated.

3.2.1. Introduction to the SW Tool

The optimization of individual transfers has been entirely carried out by DITAN, since the software allows different types of analysis, among which the options `guess`, `optimise` and `improve`. For the complete optimization of each transfer, multiple DITAN calls are required according to the specific sequence outlined in Subsection 3.2.3. Each run executes one of the following three analyses [Vasile, 2009]:

- `run guess` generates a guess by propagating a given control law or solving a simpler problem;
- `run optimise` optimizes the solution that is provided as input;
- `run improve` refines the mesh grid according to the quality of the input solution provided.

The type of analysis is specified in an input file that contains all the information needed to build and run the optimization process. This file has a very complex structure, therefore only a few blocks and features are detailed here: those that are relevant to implement the simplified dynamics and configuration of the problem.

Guess Generation

The concept used for the generation of the initial guess is forward propagation of initial conditions by using a guessed control law. The initial conditions do not only include a guessed state vector, but most importantly a guessed departure date and time of flight. Although the departure date is not relevant to the present case[2], the guessed transfer time should be guessed carefully or derived from a similar solution. Moreover, among the basic control laws available, the option chosen was `tangential +`, which consists of continuous tangential positive (in the direction of the velocity vector) thrust.

Simplified Dynamics

The simplified unperturbed dynamics derived in Subsection 2.1.1, expressed in Cartesian coordinates and in the heliocentric reference frame, is easily obtained by means of the commands:

```
Model 1
Center Sun
Reference Ecliptic
Bodies 0
```

However, `Model 1` implements the full 3D dynamical model, with no restriction to the planar case. Moreover, this formulation expects the specification of `Departure` and `Arrival` bodies with respect to which the boundary conditions are computed. This also means that the full ephemeris model would be used for the computation. In order to restrict the problem to the circular planar case, the following needs to be done:

- use of the command `Departure initial` so that initial state values are defined with respect to the body `Center` instead of to the planet Earth;
- use of attributes `initial` and `final` for the definition of the boundary conditions to specify them as absolute coordinates;
- external computation of numeric values for the definition of the initial state and the boundary conditions, that correspond to circular planar orbits with semimajor axes of Earth and Mars.

[2] Because of the use of the circle-to-circle simplification, and later adjustment of the phase.

Boundary Conditions

Here a list of the conditions that follow from the previous paragraph. The boundary conditions needed to force planar motion are straightforward:

```
bcon value state[3] initial = 0.00      bcon value state[3] final = 0.00
bcon value state[6] initial = 0.00      bcon value state[6] final = 0.00
```

Boundary conditions needed to specify the initial location at 1 AU, with specific value of infinity velocity:

```
bcon value radius initial = 149597870.7
bcon value velocity initial = [value]
bcon value radial_velocity initial = 0.00
```

Boundary conditions needed to specify the final location at 1.52 AU, with specific value of infinity velocity:

```
bcon value radius final = 227936638.9
bcon value velocity final = [value]
bcon value radial_velocity final = 0.00
```

It becomes clear from the form of the boundary conditions that infinity velocities are forced to be tangential, as the magnitude of $\vec{v}_\infty$ is added to the circular velocity at 1 or 1.52 AU. This is a simplification that is representative of real cases, since tangential is the most efficient direction. Results confirm that the tangential infinity velocity assumption applies to transfers optimized in the full ephemeris model (see Section 6.3).

Engine Model

The dependency of the thrust on the inverse square of the Sun-spacecraft distance can be easily modelled by means of the built-in `Model 2`, by specifying maximum thrust and specific impulse [Vasile, 2009].

3.2.2. Software Verification

Although the software has been widely tested and used since its development, specific tests were run with the purpose of verifying and familiarizing with its functions as well as verifying the setup described in Subsection 3.2.1. Optimal transfers found in literature were used as reference for the verification. Implementation of the simplified dynamics introduced in Sections 2.1 and 3.2.1 is found in [Kluever, 2014], in which the interplanetary SEP transfers are optimized with a direct optimization method. Ten test cases were extracted from the reference, all of them for circle-to-circle planar transfers between 1 and 1.5 AU, and using an inverse square thrust model [Kluever, 2014]. Input parameters and outcome of the optimization are reported in Table 3.3.

Input variables			**Output variables**			
$P/m\|_0$ [W/kg]	I_{sp} [s]	η [-]	TOF [days]	Transfer angle [◦]	Coast angle [◦]	ΔV [m/s]
7	2000	0.58	356.3	251.8	108.8	5419.6
7	3000	0.65	397.5	280.8	80.1	5426.9
7	1500	0.5	339	239.9	121	5417.1
7	1000	0.5	305.6	216.5	144	5412.9
7	5000	0.7	484.1	342.1	18.7	5441.2
10	7000	0.7	483.9	341.6	19.5	5441.1
5	3000	0.65	453.8	321.1	39.6	5436.8
15	3000	0.65	322	226.9	133.5	5414.6
20	3000	0.65	305.4	215.2	145.1	5412.7
25	3000	0.65	295.4	208.1	152.1	5411.9

Table 3.3: On the left: description of the setup. On the right: outputs of the optimization [Kluever, 2014].

The results of the verification done for this study are displayed in Figure 3.5. Errors being within 0.035% for the ΔV, 0.45% for the transfer time and 0.35% for the transfer angle for all optimal transfers, the proper performance of DITAN can be considered as verified[3].

[3] After optimality of the solution has been ensured, the transfers were not refined further. We can expect errors to decrease if an improvement of the mesh is performed. This is out of the scope of this section, the purpose being the verification of the agreeement between the two pieces of software.

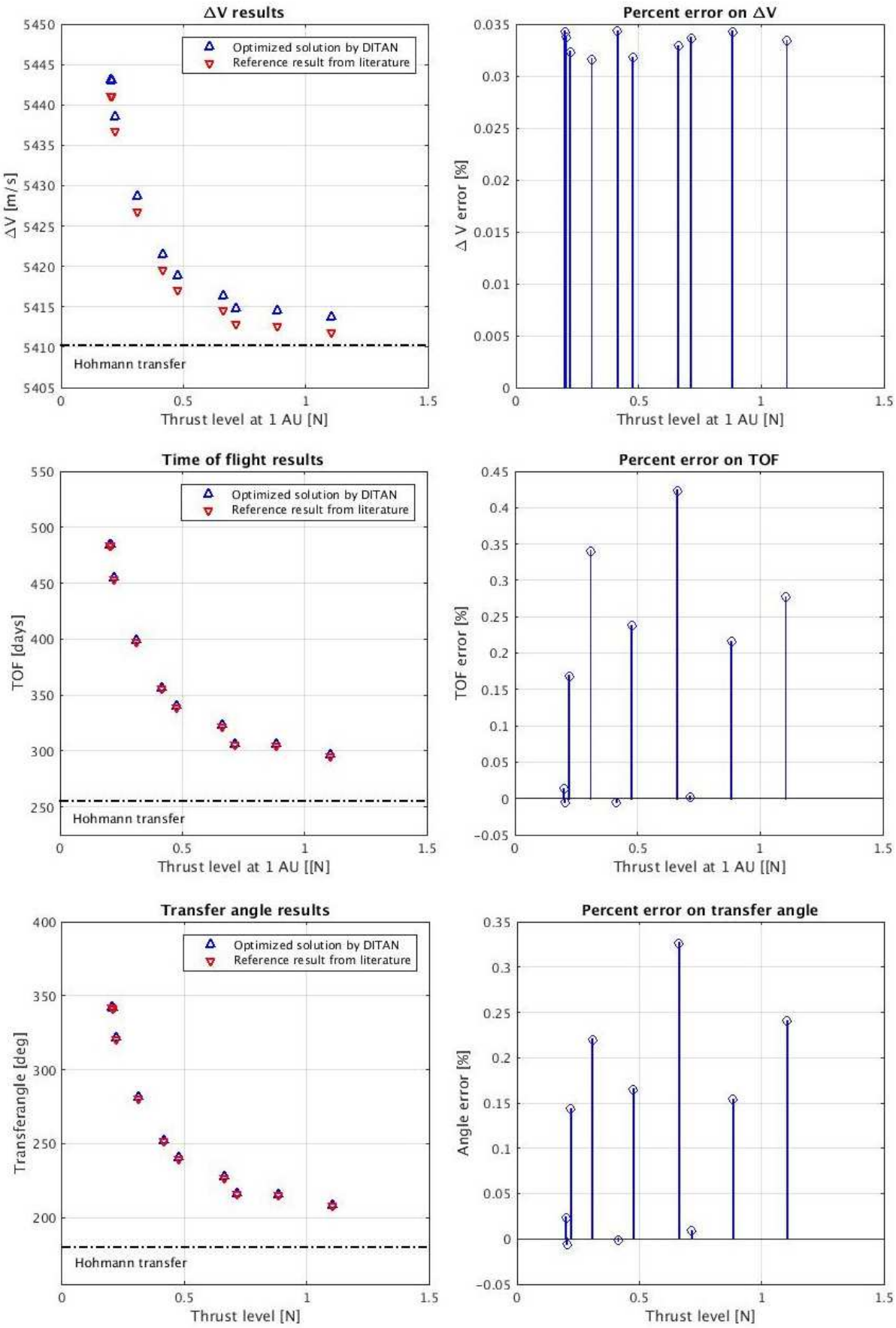

Figure 3.5: Comparison of DITAN results with reference obtained from literature, with respect to ΔV, time of flight and transfer angle.

3.2.3. Process Automation

Given the large number of optimal transfers to be derived, some additional scripting has been done to make the optimization process as automatic as possible. First of all, for each of the transfers multiple DITAN runs are required, with a minimum of one iteration of refinement/optimization (the mesh is first adjusted according to the input solution, and the optimization is subsequently run with the improved mesh). Typically, more than one of such iterations is needed, and potentially also the generation of a dedicated guess. Secondly, a set of transfers can be generated altogether by continuation, which in this case has been implemented within each family. On the contrary, the 24 continuation problems corresponding to the 24 families of transfers have been initiated manually. In the coming paragraphs this logic will be detailed, by following a bottom-up approach, from inner to outer scripting layers.

Optimization of Individual Transfers

The derivation of each optimal transfer is composed of different steps, displayed in Figure 3.6 and implemented in the Python function `full_optimization.py`. This function calls DITAN one or more times. If the path to an input solution is provided, this is used as initial guess, otherwise an adequate initial guess is generated with DITAN (`run guess`). After a first optimization is completed (`run optimise`), the corresponding gap file that contains the maximum normalized gaps between boundary and internal nodes is inspected. If there are elements in the file which are bigger than the specified threshold, iterative refinements of the mesh (`run improve`) and subsequent optimizations (`run optimise`) are run until the desired accuracy is achieved.

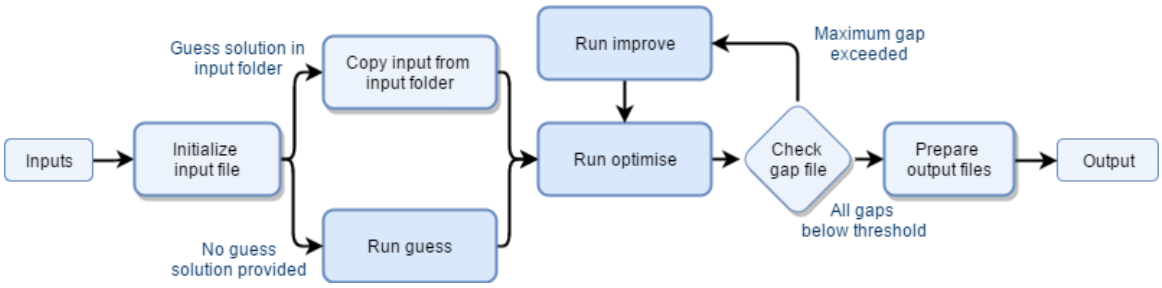

Figure 3.6: Logic of the full optimization loop for analysis of each transfer.

Continuation within Each Family of Transfers

Out of the 24 families of transfers that compose the database, a batch of nine families were generated in a first moment to build the original dataset, while the remaining 15 were optimized in a second moment, following the densification mentioned in Subsection 3.1.3. The continuation loop used for each of the first nine families is depicted in Figure 3.7. First 20 time-optimal transfers are optimized, by using as a starting point the

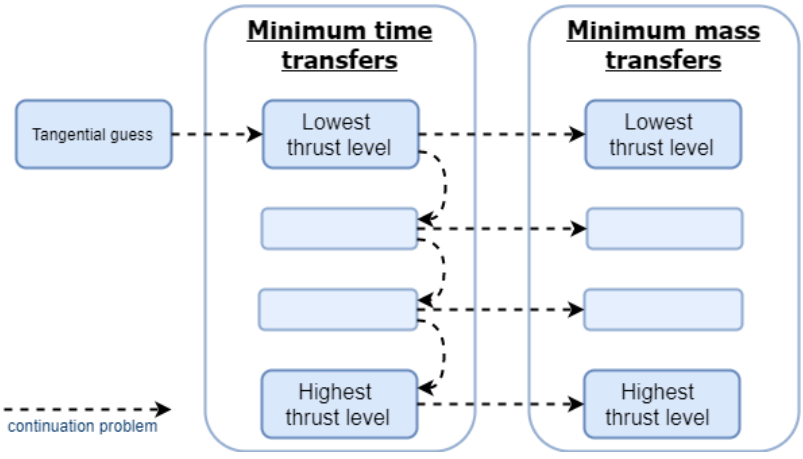

Figure 3.7: Continuation loop for generation of the original nine families of transfers.

continuous thrust propagated guess with the lowest thrust level. Then, each of the time-optimal solutions is used as guess for the corresponding mass-optimal transfer. This strategy was used because it enables to find safely all 20 mass-optimal transfers, in an automatic way. Optimizing directly the mass from a propagated solution would require intermediate steps or adjustments which were found hard to be automated, at least in this setup.

As for the remaining 15 families, those were derived from the previous batch of trajectories. In this case the continuation is reduced to the loop represented in Figure 3.8. The 'guess' family was selected from the previously derived ones, case by case.

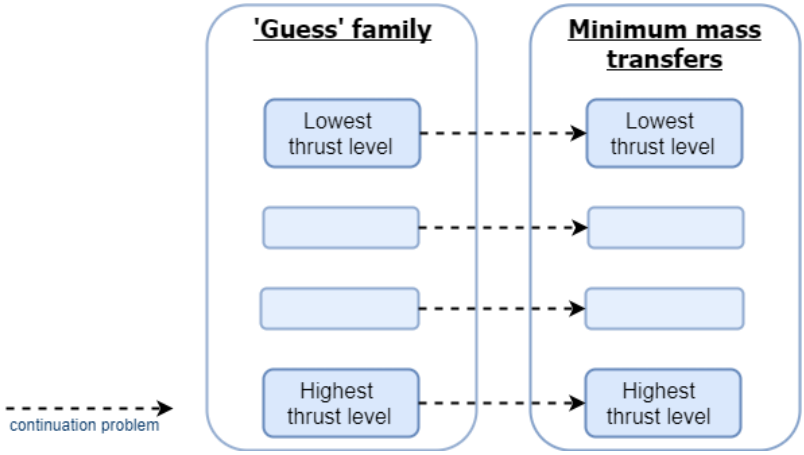

Figure 3.8: Continuation loop for generation of the additional 15 families of transfers.

General Layout

The different scripting layers are integrated in an architecture that mirrors the structure of the database presented in Subsection 3.1.3. They are displayed accordingly in Figure 3.9.

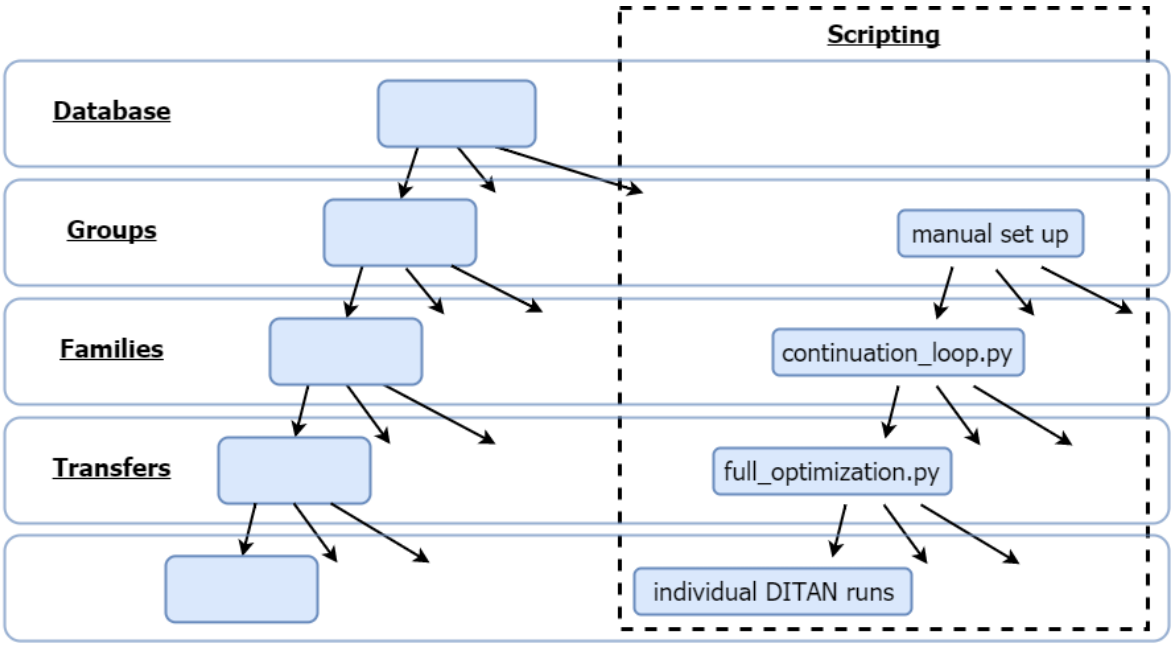

Figure 3.9: Automatic generation of the database of transfers.

3.3. Transfers Characterization

A preliminary study of the transfers was conducted before establishing the conclusive structure and composition of the database. This analysis and the plots produced include only the nine families that composed the original dataset, and the transfers are examined from two different perspectives. Firstly, for the identification of typical values and trends of the trajectory performance parameters (Subsection 3.3.1). Secondly, for characterization of the transfers in terms of number of revolutions, number of coast arcs and sequence of thrusting/coasting arcs (Subsection 3.3.2). The conclusions that were drawn are summarized in Subsection 3.3.3, which also explains how those considerations led to rethink the structure of the database.

3.3.1. Preliminary Analysis of Trajectory Parameters

In the coming paragraphs DITAN outputs are visualized and examined with respect to ΔV, transfer time and transfer angle[4]. Within each family, the variations of these variables with the initial thrust-to-mass ratio are highlighted. Typical values and ranges are also compared across the families.

Delta-V

Boundary conditions being equal, the ΔV cost of the transfer typically decreases with increasing thrust-to-mass ratio, as shown in Figure 3.10. If no infinity velocity is imparted, in the upper range of the thrust-to-mass ratio vector the ΔV becomes really close to the Hohmann transfer (about 5594 m/s). At the lower boundary of the thrust-to-mass ratio vector, the ΔV is about 55 m/s higher.

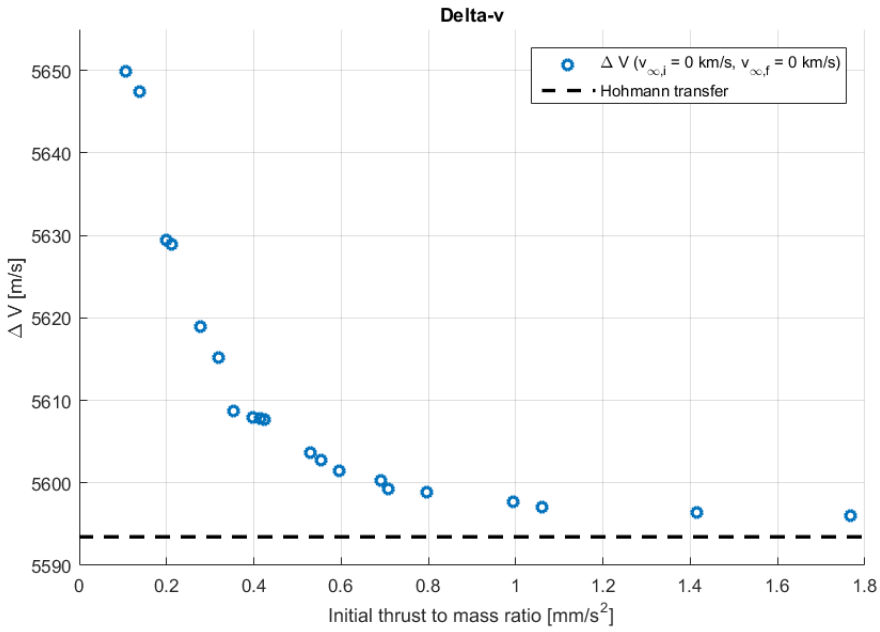

Figure 3.10: Evolution of the ΔV within the family 0-0 (no infinity velocity), ordered by thrust to mass ratio at 1 AU.

The same decreasing trend is observed in all the families. However, an offset between the curves exists due to the different values of infinity velocities. For this reason, it is convenient to plot the ΔV across families after removing this offset (equal to the sum of infinity velocity at departure and infinity velocity at arrival). In order to illustrate the issue, the ΔV data of four distinct families is compared in Figure 3.11. The left-hand side of the figure displays it before the removal of the offset, while the effect of the removal is shown in the right-hand side. The format of the right-hand side is used throughout the report to represent ΔV costs. Figure 3.11 shows that the asymptote and range identified in the case of the family 0-0 are valid for the other families as well (offset excluded). On top of that, two more features are observed. The curves are not overlapping, meaning that substracting the offset is not sufficient to capture the way the ΔV decreases when infinity velocities are

[4]The fourth intended output, namely the initial longitude/departure date, is not obtained by direct modelling of DITAN outputs, but by a subsequent analysis which is the subject of Section 5.1.

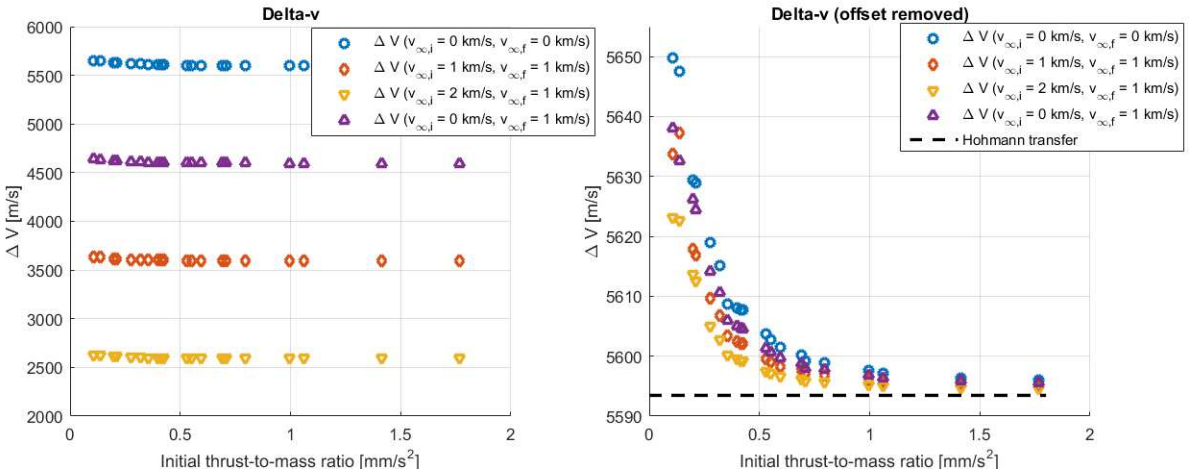

Figure 3.11: Evolution of the ΔV for four families of the original dataset, ordered by thrust to mass ratio at 1 AU.

non-zero. Moreover, there exist irregularities in the left side of the graph, which suggest the presence of different regimes. This point will be further explained in Subsection 3.3.2.

Time of Flight

The transfer time also decreases with increasing thrust-to-mass ratio, up to the lower bound provided by the Hohmann transfer (≈ 259 days). However, no offset removal is needed in this case, as shown in Figure 3.12. In fact, the values of the time of flight are in the range 265 to 965 days for all the families. The discontinuity observed between the first two samples and the rest of the data points suggests the presence of transfers with diverse numbers of revolutions. Irregularities visible in the left part of the graph mirror those mentioned in relation to the ΔV.

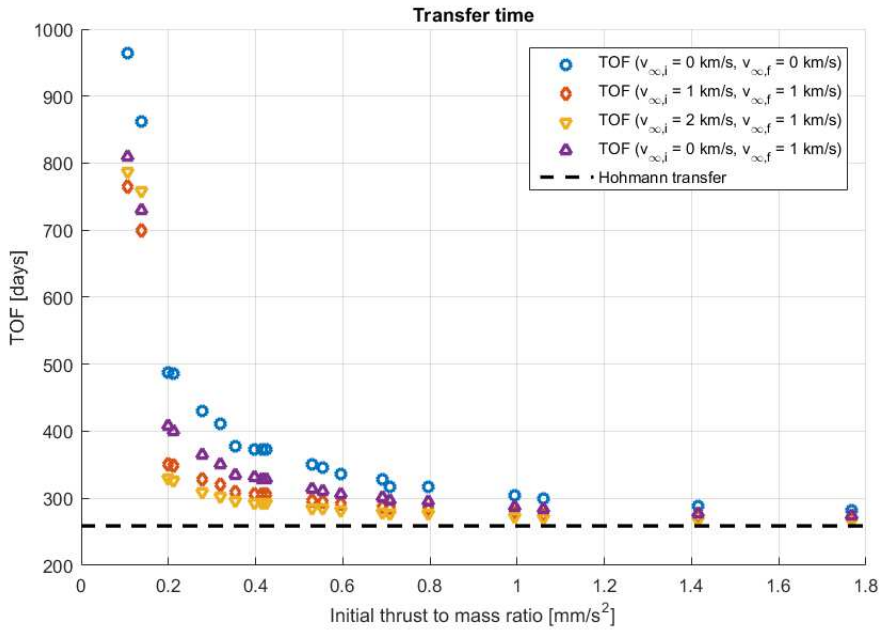

Figure 3.12: Evolution of the transfer time for four families of the original dataset, ordered by thrust to mass ratio at 1 AU.

Transfer Angle

For the transfer angle, the same trends are observed as for the transfer time (see Figure 3.13). In this case the range of interest is between 185° (close to the Hohmann transfer) and 680°, which confirms that all the transfers are completed in less than one or two revolutions.

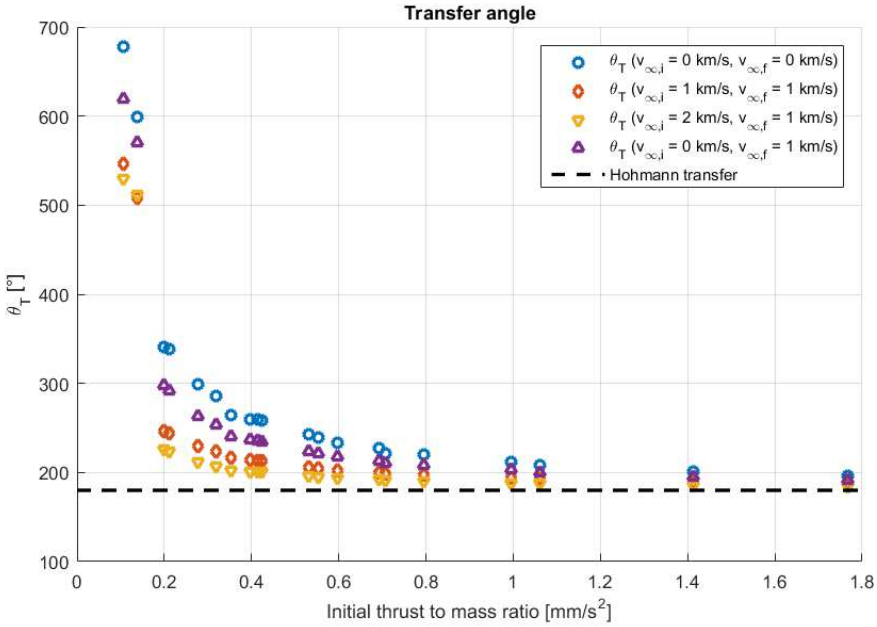

Figure 3.13: Evolution of the transfer angle for four families of the original dataset, ordered by thrust to mass ratio at 1 AU.

3.3.2. Revolutions and Thrust Profile

The full characterization of the transfers is not limited to the performance parameters but it includes the number of revolutions and coast arcs, especially to explain the irregularities observed in Subsection 3.3.1.

Number of Revolutions

In the investigated range, the transfers found are always shorter than two revolutions. In the upper part of the thrust-to-mass ratio vector, thrust levels are sufficiently high to enable transfers shorter than one revolution. However, for the samples close to the lower bound (i.e. the left part of the plots), no transfer shorter than one revolution is allowed. Figure 3.14 shows examples of the two cases, by comparing transfers for two distinct values of initial thrust-to-mass ratio.

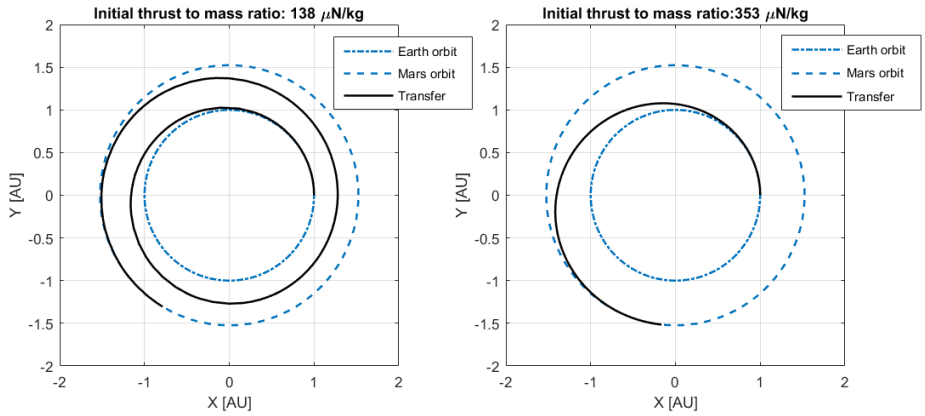

Figure 3.14: Earth-Mars transfers on the ecliptic for values of the initial thrust to mass ratio of 0.14 mN/kg (left) and 0.35 mN/kg (right).

Thrust Profile

Neither the number nor the duration of the coast arcs that define the thrust profile are imposed *a priori*, therefore the sequence of ballistic/powered arcs is an output of the computation and is optimized by the software. According to the diverse number of revolutions, the transfers present different thrust profiles in the investigated range. Two regimes are observed: a five sub-arc profile for transfers longer than one revolution, and a three sub-arc profile for those shorter than one revolution. The former includes two coast arcs (left-hand side of Figure 3.15), while the latter only has one coast arc (right-hand side of Figure 3.15). The

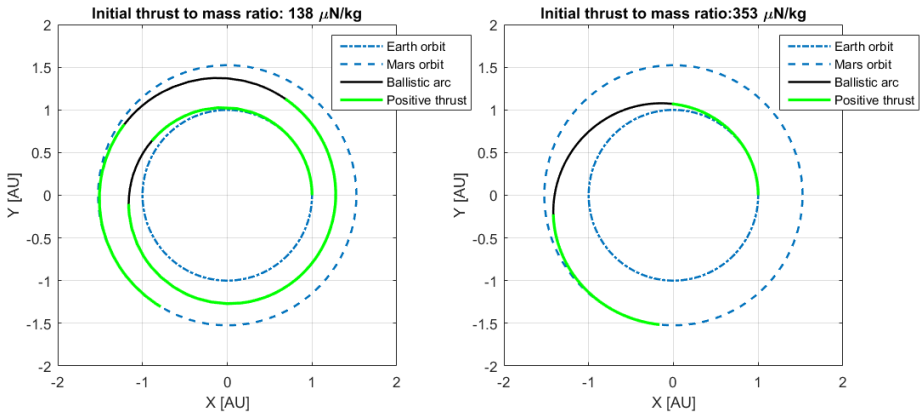

Figure 3.15: Earth-Mars transfers on the ecliptic for values of the initial thrust to mass ratio of 0.14 mN/kg (left) and 0.35 mN/kg (right). The thrust profile is highlighted: powered arcs are coloured, while ballistic arcs are black.

transition occurs at different values of the thrust-to-mass ratio across the families, thus involving a different number of samples in each of them. For example, the transition happens between 0.138 and 0.198 mN/kg for the family 0-0, and between 0.212 and 0.276 mN/kg for the family 2-0. The values have been reported for these specific two families because they identify the lower and upper bounds of this 'transition range' across the dataset. They are compared in terms of ΔV in Figure 3.16, where the average thrust-to-mass ratio is used as independent variable. For the time being, it is anticipated that this variable is used as it allows a better vi-

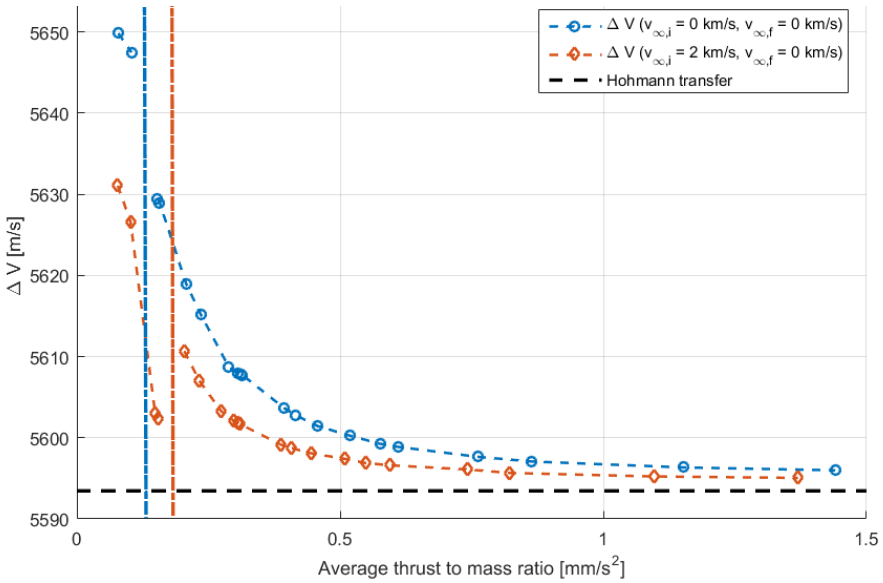

Figure 3.16: Comparison of the transition between three and five subarc regimes for two distinct families of orbits.

sualization of the trends. The theoretical explaination of this is presented in detail in Section 4.1. It should be mentioned that the vast majority of the samples falls into the thrust-coast-thrust regime. The most restricting case is represented by family 2-0, for which the transition occurs for the highest values of the thrust-to-mass ratio. Even in this case, though, about 90% of the investigated range has the three-arc thrust profile.

The analysis of the number of revolutions and coast arcs across the database confirms that the irregularities found in relation to the trajectory parameters can be traced back to the presence of distinct regimes, which cause the observed discontinuity. From Figure 3.16, it becomes clear that in order to achieve the desired model accuracy, dedicated model functions should be used for each of the two regimes. Given the fact that the large majority of the transfers are of the type thrust-coast-thrust, covering at least 90% of the investigated thrust-to-mass ratio range for all families, it has been decided to limit the development of the model to this class of transfers. It follows a restriction to transfers shorter than one revolution and, accordingly, to values of the average thrust-to-mass ratio higher than 0.2 mm/s^2, while the upper bound stays unchanged.

3.3.3. Conclusions

The analysis of DITAN outputs enabled a preliminary characterization of the transfers, both in terms of output parameters and of transfer profile. First of all, the performance parameters within each family of transfers present the expected trends, specifically a decrease with increasing thrust-to-mass ratio until the bound represented by the Hohmann transfer is approached. For each parameter, ranges of interest have been identified for the whole dataset. In the case of the ΔV, the removal of an offset related to the infinity velocities is required to allow comparison across families. With regard to the thrust profile, two distinct regimes are observed, with a transition from a five-arc profile to a three-arc profile when the thrust-to-mass ratio increases beyond a certain threshold. The threshold depends on the values of the infinity velocities, and therefore changes across families. Ninety percent of the thrust-to-mass ratio vector has a thrust-coast-thrust profile in all the families. In conclusion, the trends that are observed seem to be promising for the modelling of the trajectory performance parameters. However, the presence of different regimes complicates such modelling. For this reason, it was decided to restrict the analysis to transfers with thrust-coast-thrust profile. This implies limiting the validity range of the model to the mentioned 90% of the original thrust-to-mass ratio vector. For illustration purposes, Figure 3.17 shows the modification performed to the original dataset (top) and the reduced dataset (bottom), limited to family 0-0.

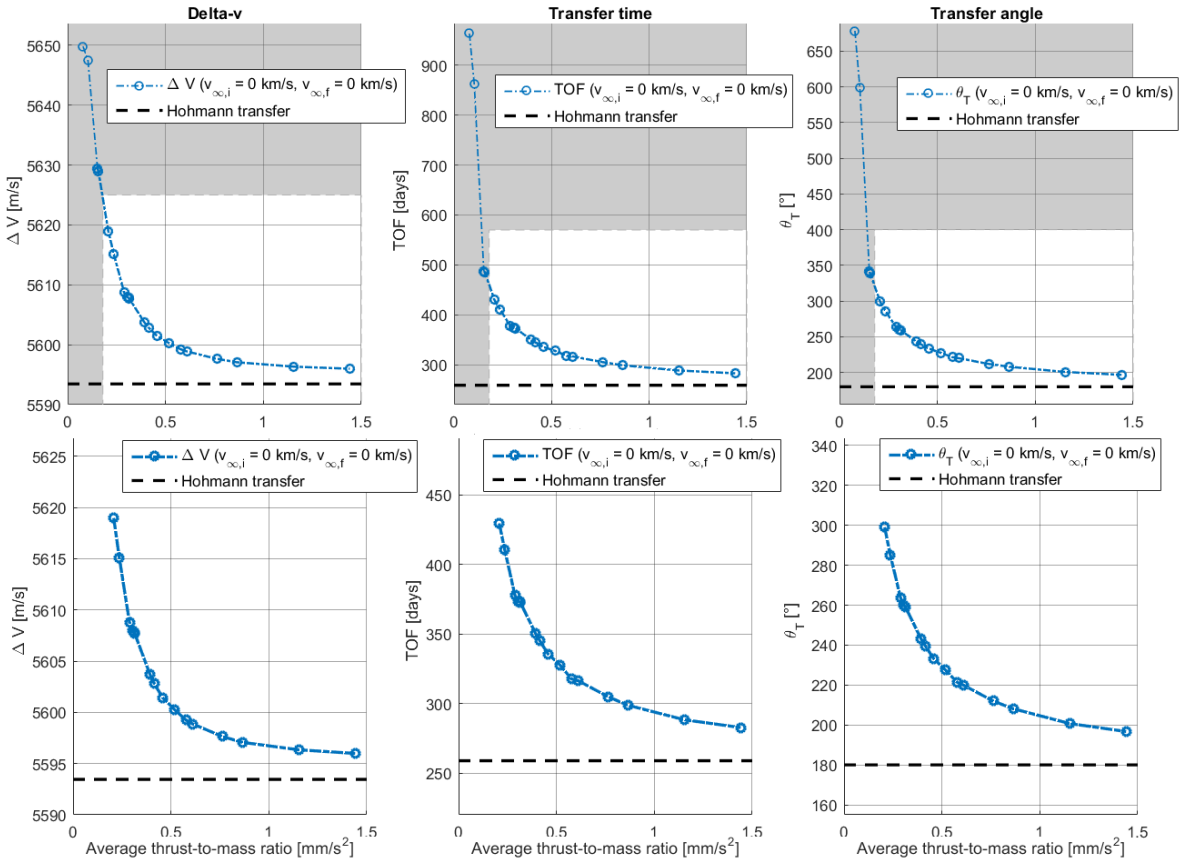

Figure 3.17: Restriction to thrust-coast-thrust transfers displayed for all trajectory parameters of the family 0-0.

4

Model Derivation

The first and core element of the modelling tool consists of a number of analytic functions which are integrated with one another in a specific architecture. They altogether approximate the profile of the transfer performance parameters ΔV, transfer time and transfer angle. The derivation of the model required several steps. First of all, the identification of the underlying trends, and of adequate independent variables to capture them. Secondly, the application of curve-fitting analysis to approximate each of the identified relations. Finally, the design of an architecture that could effectively combine these fitting blocks. In order to simplify the process, a methodology was adopted that comprises two consecutive stages. By analyzing the reference family with no infinity velocity, suitable model functions have been derived for each of the performance parameters. Such analysis is the subject of Section 4.1. The same model functions have subsequently been applied to the rest of the dataset, in order to study how to adjust them to include any combination of infinity velocities, as explained in Section 4.2.

4.1. Analysis of Zero Infinity Velocity Transfers

Having observed similar trends across all families in Section 3.3, the purpose of the present section is the derivation of analytic relations valid for the reference 0-0 family, which can then be extended to all transfers. Modelling of the data is achieved through algebraic curve-fitting, and specifically by using the ordinary least square approach for parameter estimation. Given a set of couples $\{x_i, y_i\}$ and a generic fitting model $\widetilde{f}(x)$, the aim is the minimization of the root of the sum of the squares (RSS) of the algebraic residuals $|y_i - \widetilde{f}(x_i)|$. This means finding the best fit $\overline{f}(x)$ among all fitting models $\widetilde{f}(x)$ that minimizes the RSS:

$$\sqrt{\sum_{i=0}^{n} |y_i - \overline{f}(x_i)|^2} \leq \sqrt{\sum_{i=0}^{n} |y_i - \widetilde{f}(x_i)|^2} \tag{4.1}$$

For each of the investigated models, the corresponding RSS was optimized by means of the built-in Matlab function `fmincon`. The criteria used for the selection of a model function for each variable are:

1. **Goodness** of the fit, which is expressed by means of the RSS;
2. **Complexity** of the model, which should be reduced as much as possible;
3. Distribution of the **residuals**, aiming at an even distribution with respect to the independent variable.

The relevant model basis functions which were considered are listed below:

x^k (polynomial) $\quad \left(\frac{1}{x}\right)^k$ (hyperbolic) $\quad e^{kx}$ (exponential) $\quad e^{k/x}$ (modified exponential)

4.1.1. Independent Variable: Average Acceleration

The trends to be approximated are those that emerged in Subsection 3.3.1 by plotting the transfer metrics against the initial thrust-to-mass ratio. Use of this ratio as independent parameter seems natural, however

it does not account for the fact that the acceleration profile is also very much dependent on the mass evolution during the transfer. This meaning that, even if the initial thrust-to-mass ratios are equal, the propellant consumption is strongly affected by the value of the specific impulse. As a result, also intermediate and final values of the thrust-to-mass ratio can be very different for distinct values of specific impulse, despite having the same thrust-to-mass ratio at departure. For this reason, the average acceleration is introduced in Equation 4.2:

$$\bar{a} = \frac{1}{2}(a_0 + a_f) = \frac{1}{2}\left(\frac{T_0}{m_0} + \frac{T_f}{m_f}\right) \tag{4.2}$$

This variable accounts for both aspects of the propulsion system: the initial thrust levels and the specific impulse. From the inverse square law of Equation 2.19 (thrust as a function of the Sun-spacecraft distance), the thrust-to-mass ratio can then be computed at the end of the transfer:

$$a_f = \frac{T_f}{m_f} = \frac{1}{m_f}\frac{T_0}{r_{AU}^2} \tag{4.3}$$

The use of the average acceleration as independent variable successfully deals with some of the irregularities which are observed if the initial thrust-to-mass ratio is used. The vanishing of such irregularities is best observed by comparing the top three plots of Figure 4.1, in which the initial thrust-to-mass ratio is used, with the bottom ones, that use the average acceleration as independent variable.

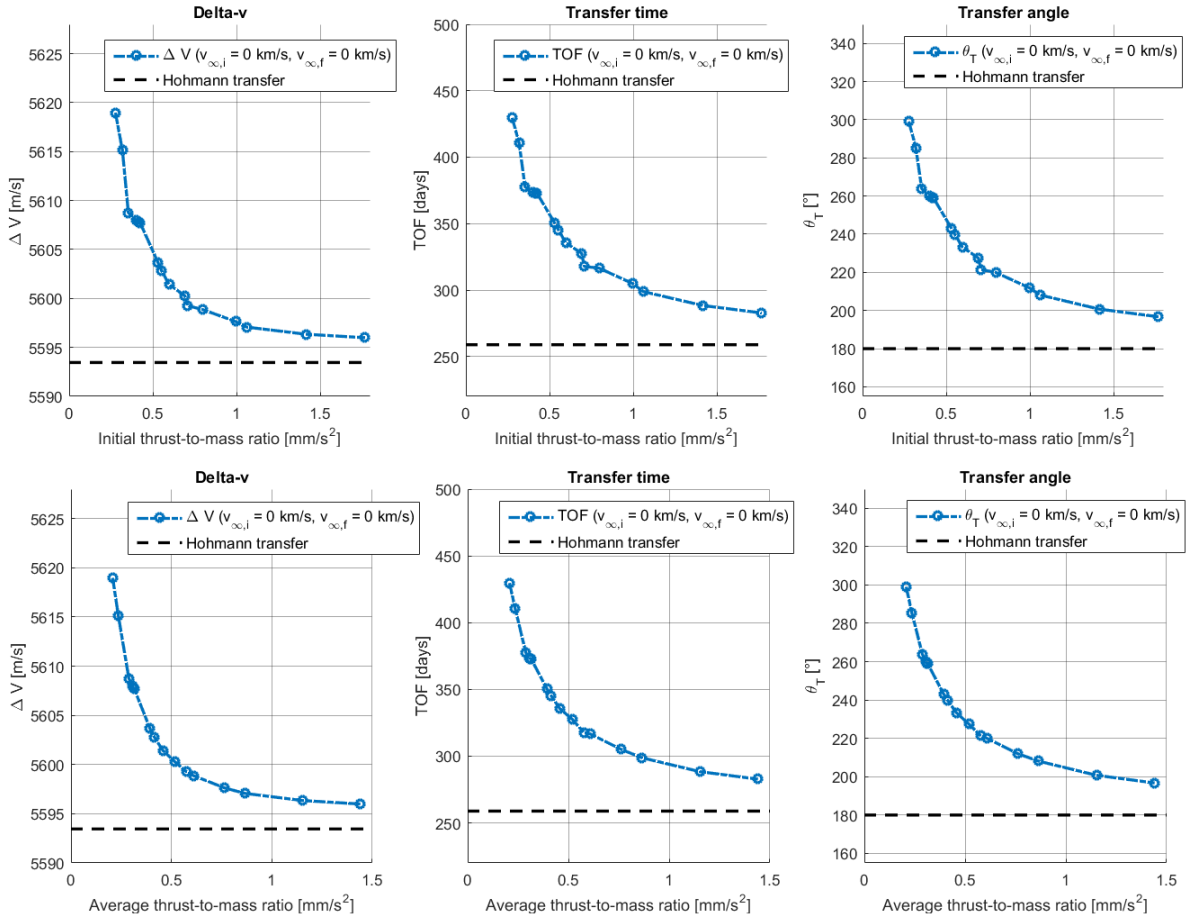

Figure 4.1: Comparison between the use of initial and average acceleration as independent variable.

It is worth mentioning that unlike the initial thrust-to-mass ratio, the average acceleration is not an input to the problem, as it depends on the final mass (i.e. on the ΔV). However, it can be estimated from the inputs, by approximating the final mass with that corresponding to the Hohmann transfer, as in Equation 4.4:

$$\tilde{\bar{a}} = \frac{1}{2}\left(\frac{T_0}{m_0} + \frac{1}{\tilde{m}_f}\frac{T_0}{r_{AU}^2}\right) \qquad \tilde{m}_f = m_0 e^{-\widetilde{\Delta V}_H / g_0 I_{sp}} \tag{4.4}$$

The symbol $\widetilde{\Delta V}_H$ is used to represent an adjusted ΔV_H cost. The Hohmann ΔV_H should in fact be corrected by means of the offset mentioned above before computing the final mass, to account for the infinity velocities. Figure 4.2 analyzes the relative errors on the average acceleration brought about by using the values estimated with this procedure. Errors have been computed for all 384 cases that compose the definitive dataset. The histogram on the left-hand side shows how these errors are distributed between 0% and −0.035%, which is the largest estimation error over the entire database. All errors are negative due to the fact that $\widetilde{\Delta V}_H$ slightly underestimates the low-thrust ΔV, resulting in final mass lower than $\tilde{m}_f$, and in a real average acceleration higher than estimated. Moreover, in the right-hand side of Figure 4.2 the maximum percent error for each initial thrust-to-mass ratio value is displayed as a bar. The aim is to show that errors are greater for lower thrust levels, easily explained by the fact that in those cases the ΔV is farther from the Hohmann reference case. Relative errors are in all cases very limited, therefore it can be concluded that use of the average acceleration as independent variable is safe, besides beneficial, since it can be accurately estimated from the inputs.

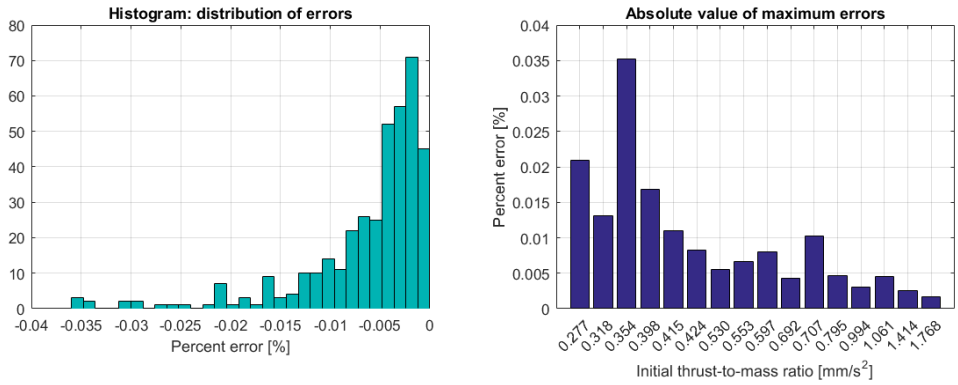

Figure 4.2: Percent errors in the estimate of the average acceleration: distribution of the errors (left) and maximum relative errors (right).

4.1.2. Modelling the Data

The evolution of the trajectory performance parameters with respect to the average acceleration is modelled according to the procedure outlined in the above. The results are presented in the following paragraphs.

Delta-V

A linear combination of hyperbolic basis functions provides a good fit for the ΔV. Figure 4.3 shows the fitting through the data points as well as the residuals distribution. Four fit coefficients are optimized:

$$\Delta V = k_{0,\Delta V} + \frac{k_{1,\Delta V}}{\bar{a}} + \frac{k_{2,\Delta V}}{\bar{a}^2} + \frac{k_{3,\Delta V}}{\bar{a}^3} \tag{4.5}$$

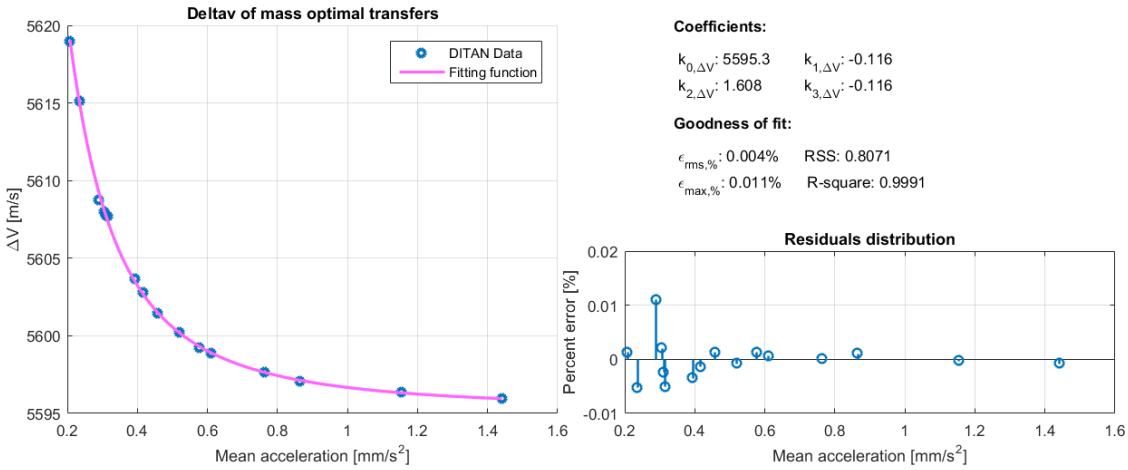

Figure 4.3: ΔV fitting through the data points: visualization, residuals distribution and goodness of fit.

Transfer Time Modelling

A hyperbolic function provides a good fit for the transfer time, in the form of Equation 4.6.

$$TOF = k_{0,TOF} + \frac{k_{1,TOF}}{\bar{a}} \tag{4.6}$$

Figure 4.4 shows the fitting through the data points as well as the residuals distribution.

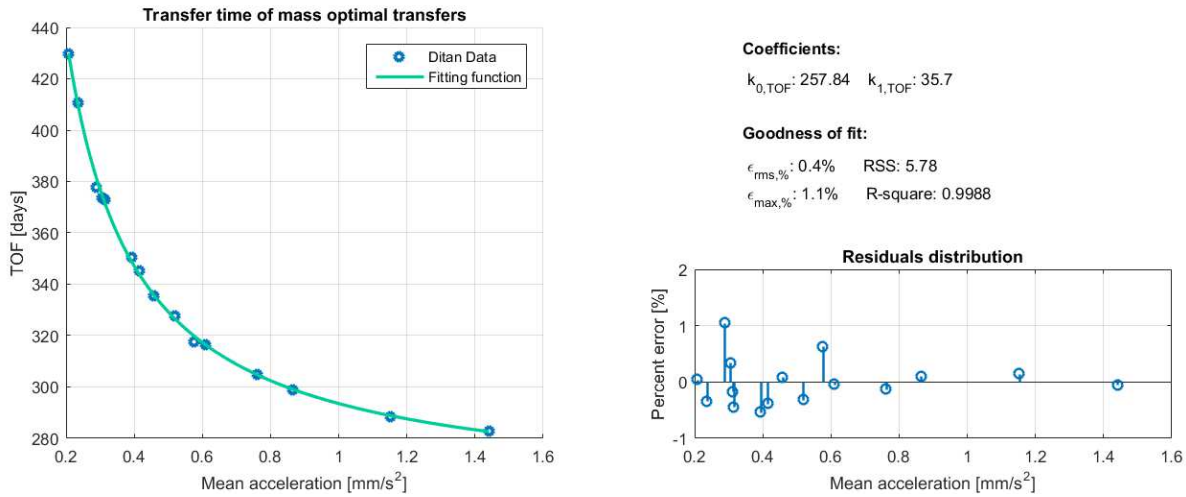

Figure 4.4: Time of flight fitting through the data points: visualization, residuals distribution and goodness of fit.

Transfer Angle Modelling

A hyperbolic fitting function was chosen for the transfer angle. As for the transfer time, only two coefficients are optimized (Equation 4.7).

$$\theta_T = k_{0,\theta_T} + \frac{k_{1,\theta_T}}{\bar{a}} \tag{4.7}$$

Figure 4.5 shows the fitting through the data points as well as the residuals distribution.

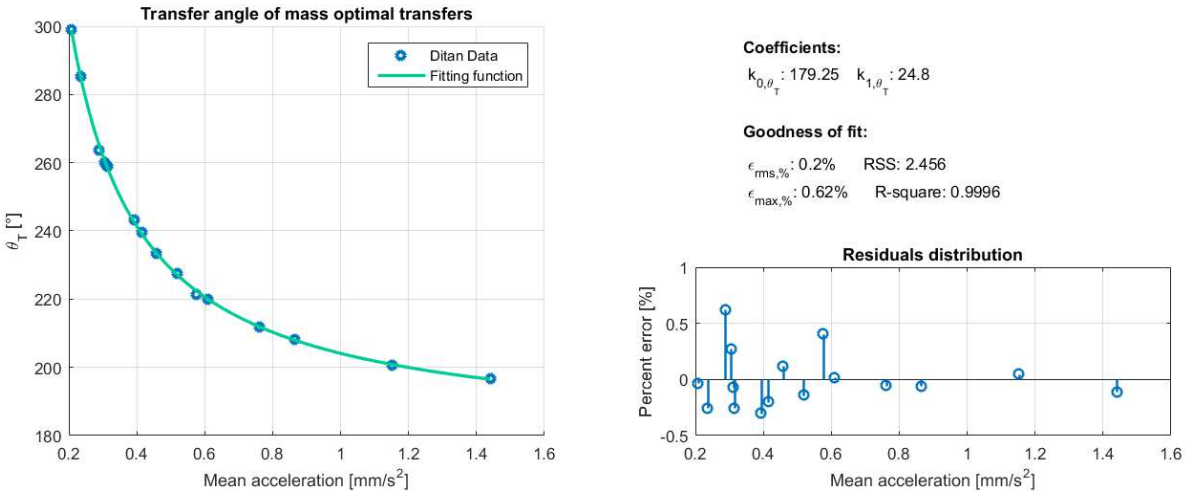

Figure 4.5: Transfer angle fitting through the data points: visualization, residuals distribution and goodness of fit.

4.1.3. Conclusions

After identification of a proper independent variable for the modelling, the best fit in a least square sense was constructed for each of the three trajectory parameters. The model functions which were built all consist of linear combinations of hyperbolic basis functions, with two to four parameters to be estimated:

$$\Delta V = k_{0,\Delta V} + \frac{k_{1,\Delta V}}{\bar{a}} + \frac{k_{2,\Delta V}}{\bar{a}^2} + \frac{k_{3,\Delta V}}{\bar{a}^3}$$

$$TOF = k_{0,TOF} + \frac{k_{1,TOF}}{\bar{a}}$$

$$\theta_T = k_{0,\theta_T} + \frac{k_{1,\theta_T}}{\bar{a}}$$

The extension of the three models to the rest of the dataset is the subject of Section 4.2. It is anticipated here that one of the outcomes of such an extension is the finding that the behaviour of the coefficients $k_{i,p}$ is more regular across families if a variant of the model functions is used. Therefore, instead of using the expressions of Equations 4.5, 4.6 and 4.7, the models are adjusted by forcing the asymptotes to the values corresponding to the Hohmann transfer, as in Equations 4.8 to 4.10:

$$\Delta V = \Delta V_H + \frac{k_{1,\Delta V}}{\bar{a}} + \frac{k_{2,\Delta V}}{\bar{a}^2} + \frac{k_{3,\Delta V}}{\bar{a}^3} \tag{4.8}$$

$$TOF = TOF_H + \frac{k_{1,TOF}}{\bar{a}} \tag{4.9}$$

$$\theta_T = \theta_{T,H} + \frac{k_{1,\theta_T}}{\bar{a}} \tag{4.10}$$

The adjustment results in the overall improvement of the model accuracy in terms of maximum error on the entire dataset, although the coefficients $k_{0,p}$ do not have the optimal value on individual families of transfers. Figure 4.6 compares DITAN data with the adjusted model functions (i.e. those of Equations 4.8 to 4.10 that make use of ΔV_H, TOF_H and $\theta_{T,H}$), and reports the adjusted fit coefficients as well as the goodness of the fit.

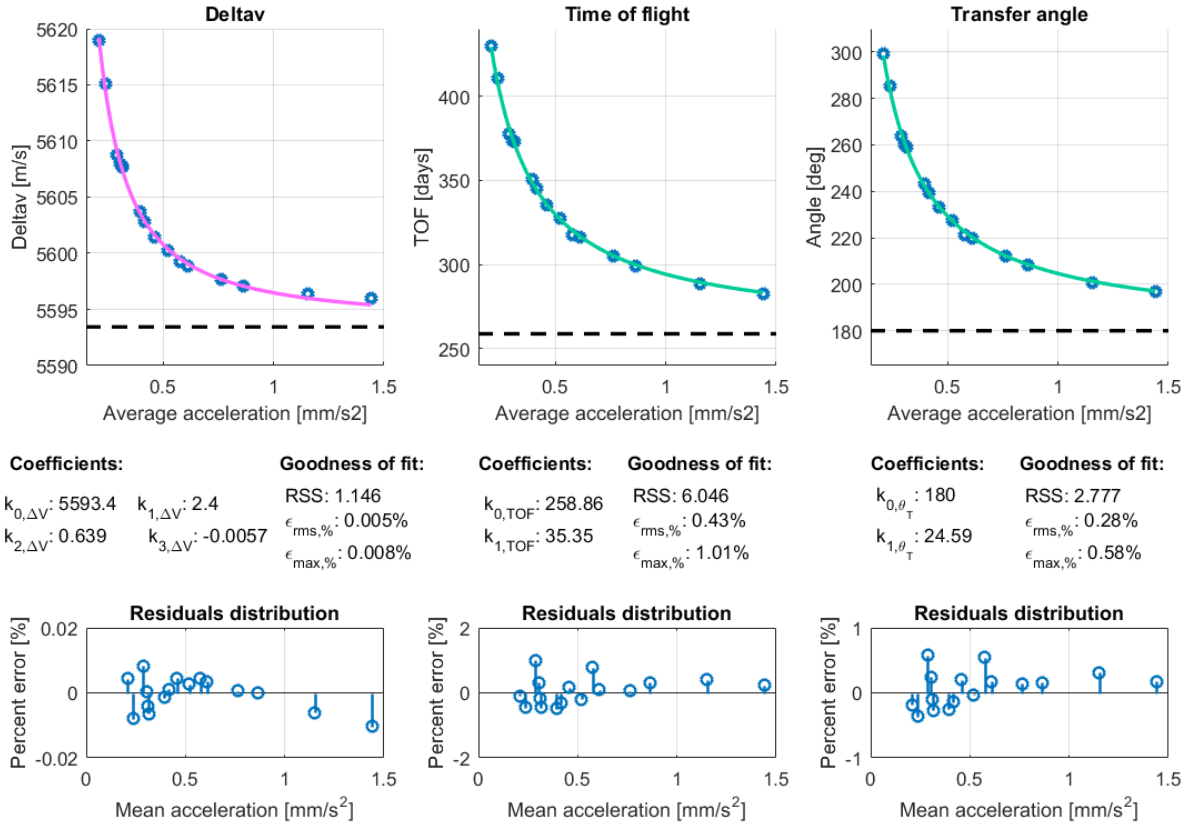

Figure 4.6: ΔV, transfer time and angle fitting through the data points: visualization, residuals distribution and goodness of fit.

4.2. Analysis of Non-zero Infinity Velocity Transfers

The purpose of the present section is to model the dependence of the trajectory parameters on the values of infinity velocity at departure and at arrival, since they have been found to have an impact, as already mentioned in Section 3.3. A preliminary analysis of the optimal transfers has shown that the effect is not symmetric between departure and arrival infinity velocity. Moreover, the impact of the excess velocities can be decomposed into two contributions, which are attributed to the two distinct parameters. They are identified and defined in Subsection 4.2.1. The two contributions are then analyzed and modelled separately, respectively in Subsections 4.2.2 and 4.2.3. From this investigation, the behaviours are found to be the same for all three trajectory parameters. However, the significance of the latter contribution is negligible in the case of the ΔV, while it plays an important role with regard to transfer time and transfer angle. Therefore, although plots and numerical values are reported for all the variables, the discussion and the comments are for brevity focused on the time of flight only.

4.2.1. Identification of Independent Variables

For the characterization of the trajectory metrics across families, use of the average acceleration is not sufficient to capture their evolution. For better visualization and analysis of the underlying trends, two additional variables are defined here:

1. **Total infinity velocity** $v_{\infty,tot}$, which is the magnitude of the sum of initial and final infinity velocities:

$$v_{\infty,tot} = v_{\infty,i} + v_{\infty,f} \tag{4.11}$$

2. **Velocity fraction at arrival** $\hat{v}_{\infty,f}$, which is the fraction of infinity velocity at arrival, with respect to the total infinity velocity, and accounts for the distribution of $v_{\infty,tot}$ between departure and arrival:

$$\hat{v}_{\infty,f} = \frac{v_{\infty,f}}{v_{\infty,tot}} \tag{4.12}$$

In Figure 4.7, the velocity fraction at arrival is used as independent coordinate together with the average acceleration to display the transfer time data (respectively, $\hat{v}_{\infty,f}$ along the X-axis and $\bar{a}$ along the Y-axis). Fifteen families are represented, which are arranged into three groups of different colours according to the

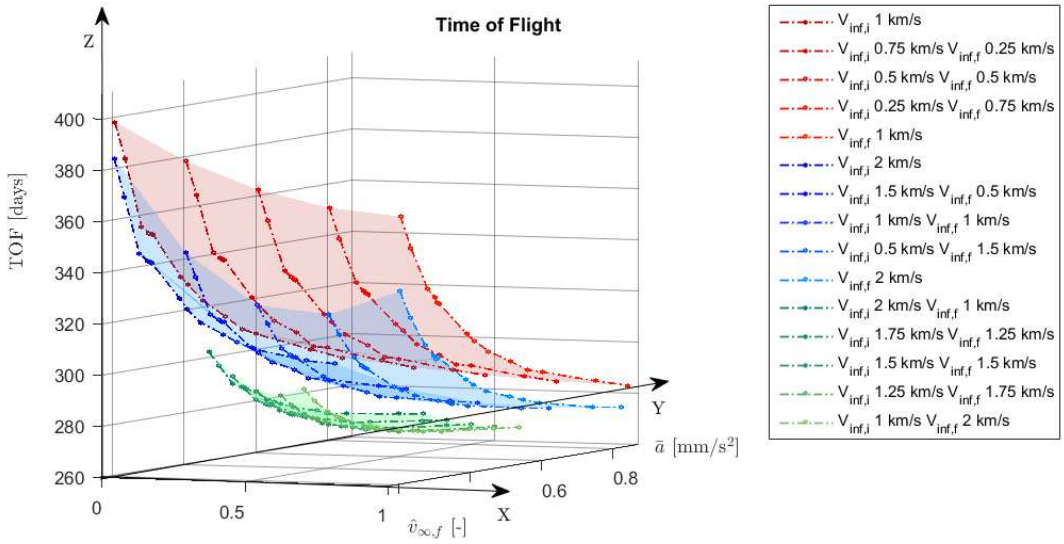

Figure 4.7: 3D visualization of the time of flight data against average acceleration and fraction velocity at arrival.

value of total infinity velocity $v_{\infty,tot}$ (red: $v_{\infty,tot}$ = 1 km/s, blue: $v_{\infty,tot}$ = 2 km/s, green: $v_{\infty,tot}$ = 3 km/s). Moreover, for illustration purposes only the average acceleration range 0.2-0.8 mm/s^2 is included. By visually inspecting the data two overlapping trends emerged. Firstly, in general higher values of $v_{\infty,tot}$ correspond to shorter transfers. Secondly, a quadratic trend is observed on the XZ-plane of Figure 4.7. In fact, being

average acceleration and total infinity velocity equal, the evolution of the transfer time with respect to fraction velocity at arrival appears to follow a quadratic function. Visual inspection of the data suggests that the two overlapping trends can be analyzed separately, by modelling the impact of $v_{\infty,tot}$ first, and applying a correction depending on $\hat{v}_{\infty,f}$ afterwards. By impact, it is referred to the impact of the variable of interest on the coefficients $k_{i,p}$ introduced in Subsection 4.1.2, and therefore on the shape of the function $p(\bar{a})$ for the evolution of the parameter p.

Methodology

First, the behaviour of the hyperbolic coefficients is studied in relation to the total infinity velocity $v_{\infty,tot}$. A selection of families is used for this analysis, specifically those for which the initial infinity velocity is equal to the final infinity velocity. These families of transfers are in the following referred to as *reference families*. Selecting the reference curves only corresponds to restricting to the YZ-plane of Figure 4.7, for $\hat{v}_{\infty,f} = 0.5$. This is the plane represented in Figure 4.8. This restriction also explains the densification mentioned in Subsection 3.1.3, which was carried out with the intention of having a minimum of 10 families on this plane.

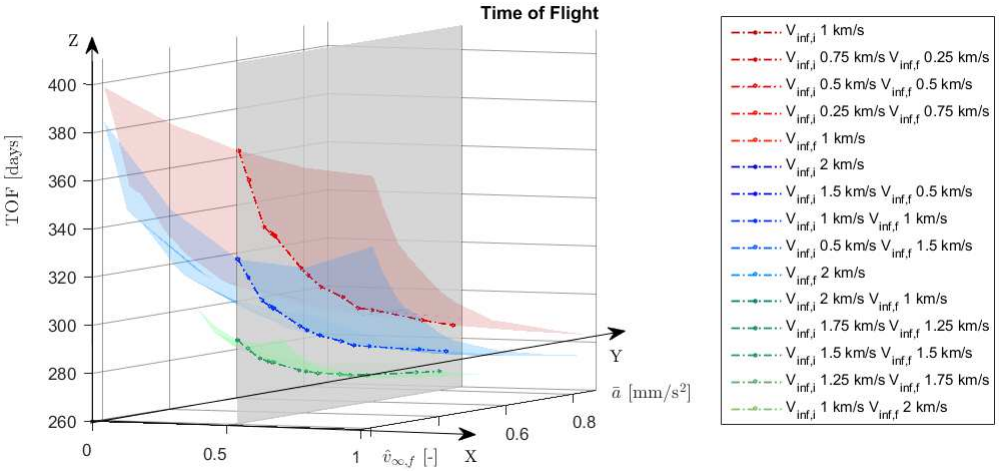

Figure 4.8: Visualization of the YZ-plane ($\hat{v}_{\infty,f} = 0.5$) on which the reference curves lie.

The second part of the modelling consists in considering the impact of $\hat{v}_{\infty,f}$ and implementing a related correction. It is equivalent to analyzing the XZ-plane represented in Figure 4.9. In this regard, it is useful to refer to *groups* of families, meaning that families are grouped according to the value of $v_{\infty,tot}$. The behaviour of the hyperbolic coefficients is then studied within each group, and across groups. This is a reason of a further densification, aiming at having four groups with enough resolution in terms of $\hat{v}_{\infty,f}$ in each group. Subsections 4.2.2 and 4.2.3 address the two modelling steps that have just been described.

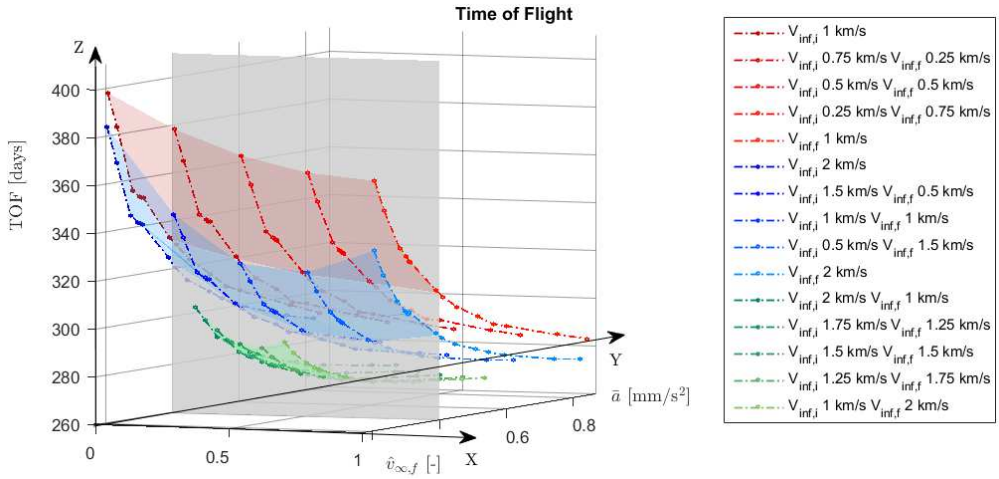

Figure 4.9: Visualization of XZ-plane used for analysis of the effect of $\hat{v}_{\infty,f}$.

4.2.2. Analysis of Reference Curves

Transfer time

The time of flight data of all 10 reference curves is included in Figure 4.10, together with the hyperbolic best fit through the data points. It is pointed out how the curve flattens as the total infinity velocity increases, getting closer and closer to the Hohmann asymptote.

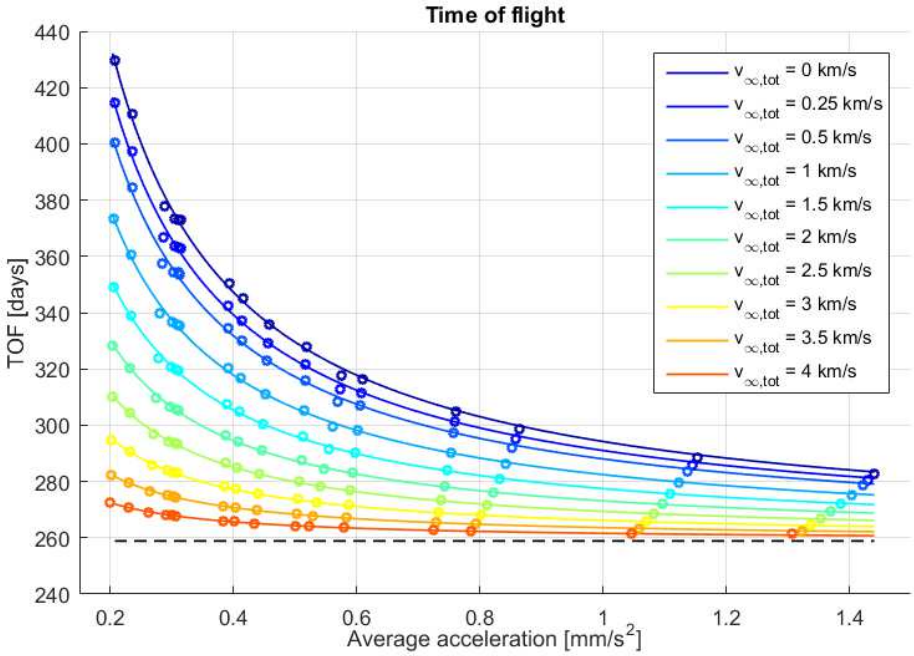

Figure 4.10: Time of flight data of reference curves depending on average acceleration and total infinity velocity.

The lowering of the curve is mirrored by the decrease in the hyperbolic coefficient $k_{1,TOF}$. In fact, this coefficient is simply the excess time (compared to the Hohmann TOF_H) for a value of the average acceleration equal to 1 mm/s^2, as it follows from Equation 4.9. The evolution of $k_{1,TOF}$ for increasing total infinity velocity is well approximated by a polynomial function of order two, as shown in Figure 4.11.

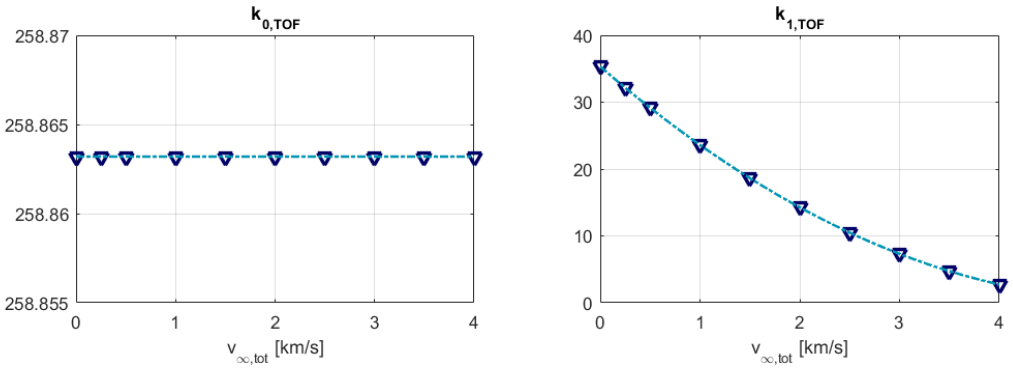

Figure 4.11: Hyperbolic coefficients $k_{0,TOF}$ and $k_{1,TOF}$ against total infinity velocity.

The total infinity velocity being known, the hyperbolic coefficients $k_{0,TOF}$ and $k_{1,TOF}$ of the corresponding reference curve are then easily derived from the polynomial functions displayed in light blue in Figure 4.11 and identified by the polynomial coefficients TOF_H,and $p_{1j,TOF}$ (with $j = 0,1,2$):

$$k_{0,TOF} = TOF_H \tag{4.13}$$

$$k_{1,TOF} = p_{10,TOF} + p_{11,TOF} v_{\infty,tot} + p_{12,TOF} v_{\infty,tot}^2 \tag{4.14}$$

Transfer angle

Results found for the transfer angle reflect those of the transfer time. In the left-hand side of Figure 4.12 the lowering of the data is shown, as well as the hyperbolic fitting curves through the data points. The right-hand side of the same figure depicts the evolution of the coefficients, with the order-two polynomial fit.

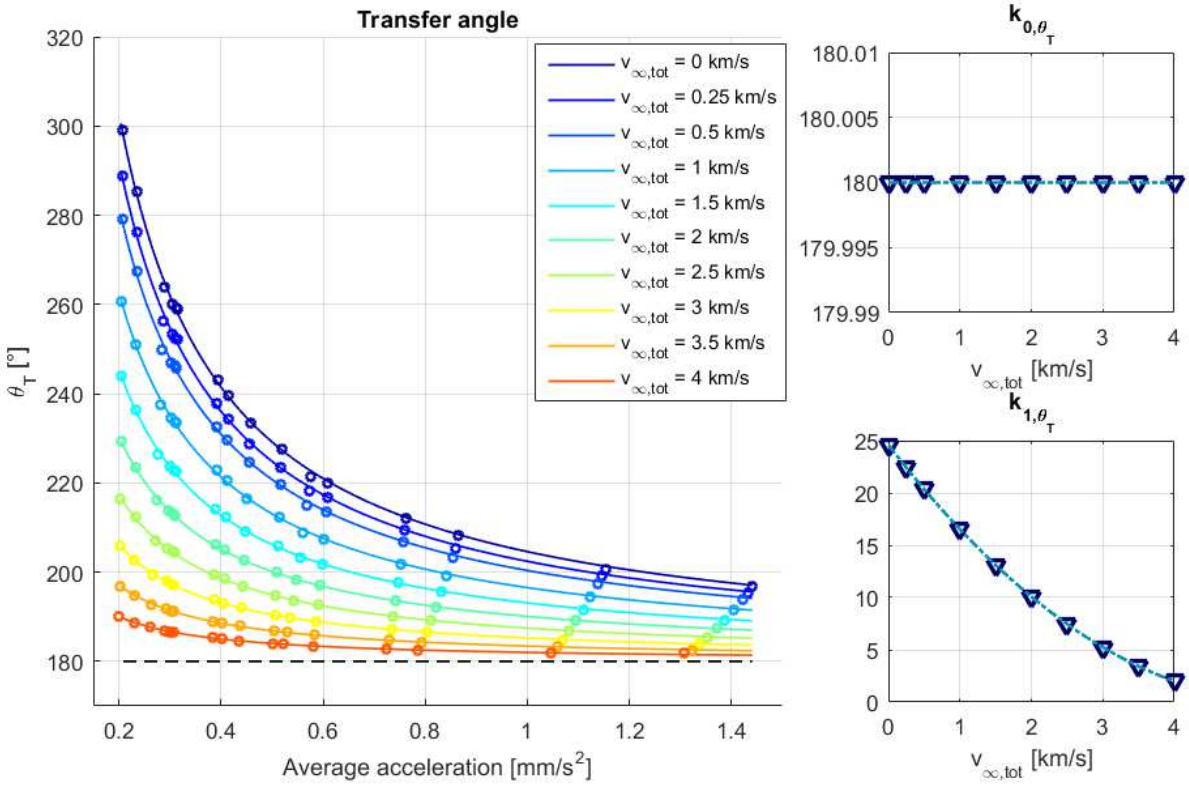

Figure 4.12: Left: transfer angle data of reference curves depending on average acceleration and total infinity velocity. Right: hyperbolic coefficients k_{0,θ_T} and k_{1,θ_T} against total infinity velocity.

The values of the coefficients k_{0,θ_T} and k_{1,θ_T} are similarly derived from the total infinity velocity, by means of the polynomial functions displayed in light blue in the right-hand side of Figure 4.12 and identified by the polynomial coefficients $\theta_{T,H} = 180°$ and p_{1j,θ_T} (with $j = 0,1,2$):

$$k_{0,\theta_T} = 180° \tag{4.15}$$

$$k_{1,\theta_T} = p_{10,\theta_T} + p_{11,\theta_T} v_{\infty,tot} + p_{12,\theta_T} v_{\infty,tot}^2 \tag{4.16}$$

Delta-V

The model function that has been identified for the ΔV comprises four instead of two hyperbolic coefficients. Although the ΔV curves also flatten with increasing $v_{\infty,tot}$ (left-hand side of Figure 4.13), a higher-order polynomial is needed to describe the evolution of the three optimized coefficients $k_{1,\Delta V}$, $k_{2,\Delta V}$ and $k_{3,\Delta V}$. The right-hand side of Figure 4.13 shows the 10 discrete values of the coefficients and the order-three polynomial functions that best fit these data points, which are displayed in light blue and identified by the polynomial coefficients ΔV_H and $p_{ij,\Delta V}$ (with $i = 1,2,3$ and $j = 0,1,2,3$). Given a specific value of total infinity velocity, the reference curve that models the ΔV evolution with $\bar{a}$ is uniquely determined from Equations 4.17 to 4.20:

$$k_{0,\Delta V} = \Delta V_H \tag{4.17}$$

$$k_{1,\Delta V} = p_{10,\Delta V} + p_{11,\Delta V} v_{\infty,tot} + p_{12,\Delta V} v_{\infty,tot}^2 + p_{13,\Delta V} v_{\infty,tot}^3 \tag{4.18}$$

$$k_{2,\Delta V} = p_{20,\Delta V} + p_{21,\Delta V} v_{\infty,tot} + p_{22,\Delta V} v_{\infty,tot}^2 + p_{23,\Delta V} v_{\infty,tot}^3 \tag{4.19}$$

$$k_{3,\Delta V} = p_{30,\Delta V} + p_{31,\Delta V} v_{\infty,tot} + p_{32,\Delta V} v_{\infty,tot}^2 + p_{33,\Delta V} v_{\infty,tot}^3 \tag{4.20}$$

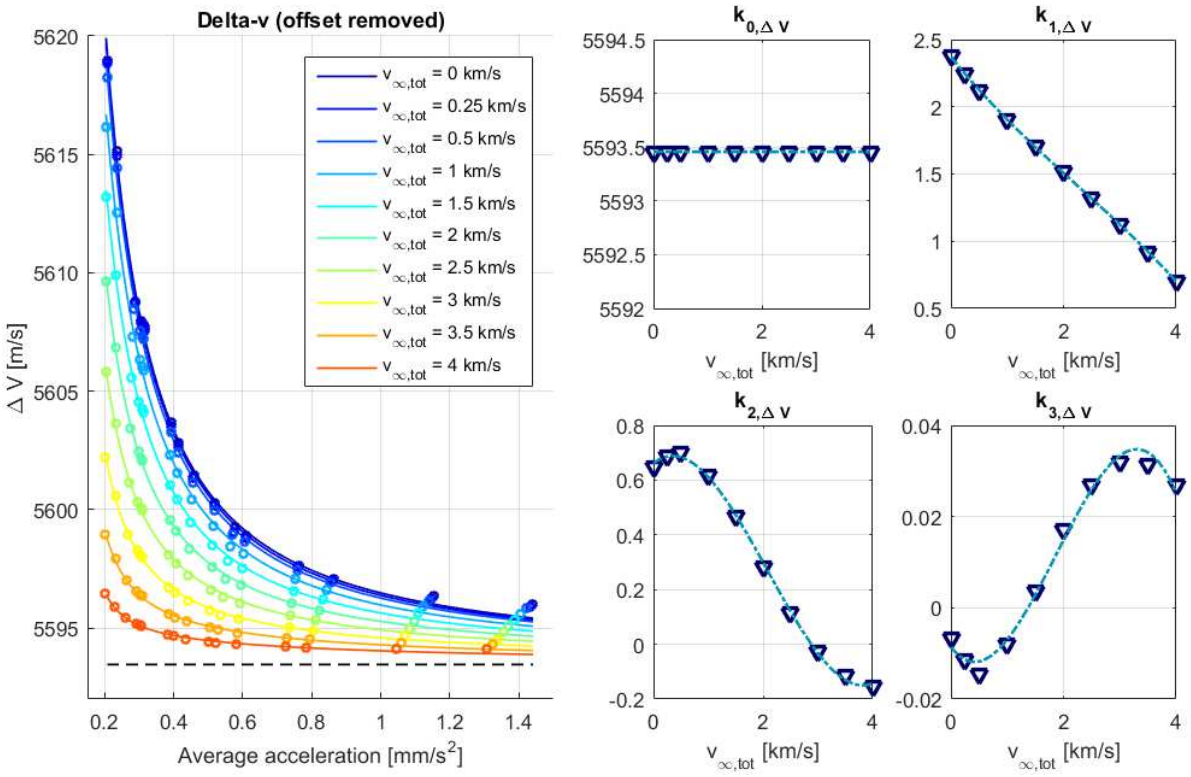

Figure 4.13: Left: ΔV data of reference curves depending on average acceleration and total infinity velocity. Right: hyperbolic coefficients $k_{0,\Delta V}$ to $k_{3,\Delta V}$ against total infinity velocity.

Summary

A summary of all polynomial fitting functions that approximate the hyperbolic coefficients of the reference curves is given in Table 4.1. Values of the polynomical coefficients are also included.

p	**Polynomial function**	$p_{i0,p}$	$p_{i1,p}$	$p_{i2,p}$	$p_{i3,p}$
ΔV	$k_{0,\Delta V} = \Delta V_H$	5593.457	-	-	-
	$k_{1,\Delta V} = p_{10} + p_{11}\,v_{i,t} + p_{12}\,v_{i,t}^2 + p_{13}\,v_{i,t}^3$	-0.009183	0.062361	-0.520305	2.371807
	$k_{2,\Delta V} = p_{20} + p_{21}\,v_{i,t} + p_{322}\,v_{i,t}^2 + p_{23}\,v_{i,t}^3$	0.040251	-0.251548	0.161308	0.660989
	$k_{3,\Delta V} = p_{30} + p_{31}\,v_{i,t} + p_{32}\,v_{i,t}^2 + p_{33}\,v_{i,t}^3$	-0.003903	0.021781	-0.016239	-0.008579
TOF	$k_{0,TOF} = TOF_H$	258.863	-	-	-
	$k_{1,TOF} = p_{10} + p_{11}\,v_{i,t} + p_{12}\,v_{i,t}^2$	1.191444	-12.909801	35.321082	-
θ_T	$k_{0,\theta_T} = 180°$	180	-	-	-
	$k_{1,\theta_T} = p_{10} + p_{11}\,v_{i,t} + p_{12}\,v_{i,t}^2$	0.805611	-8.868851	24.594335	-

Table 4.1: Polynomial model functions, coefficients and goodness of the fit.

4.2.3. Dependence on Infinity Velocity Fraction

An example of the quadratic trend mentioned in Subsection 4.2.1 is obtained if the transfer time data is plotted as in Figure 4.14. In the right-hand side of the graph, the longest transfer time of each family is related to the corresponding value of fraction velocity at arrival. Eighteen families are included, which are collected into four groups depending on the total infinity velocity (for values of 0.25, 1, 2 and 3 km/s of $v_{\infty,tot}$).

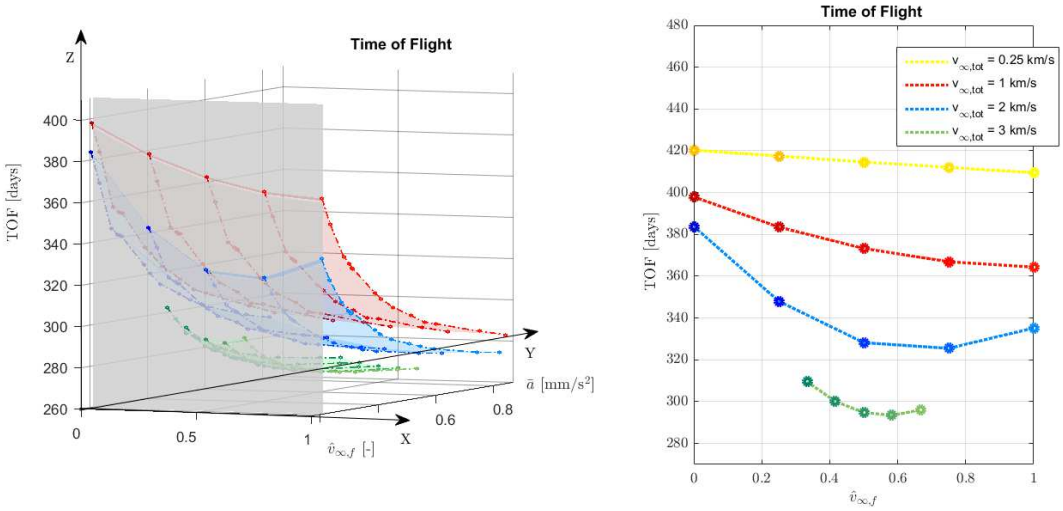

Figure 4.14: Longest transfer times across four groups of transfers. It is pointed out that the plane shown on the left is only intended for illustration purposes: due to the differences in the values of average acceleration, each curve is sliced for a slightly different value of $\bar{a}$.

A similar behaviour is found for the transfer angle and ΔV as well: for simplicity the discussion is therefore focused on the time of flight results.

Time of Flight

When the four groups are analyzed separately, a parabola provides a good fit for the hyperbolic coefficients $k_{1,TOF}$. In Figure 4.15, the empirical values of $k_{1,TOF}$ are displayed in dark blue, except for that of the reference curve, which is highlighted in red. These reference hyperbolic coefficients are called $\bar{k}_{TOF}$ in the remaining of the report. Dashed lines represent parabolic fit functions which are forced through $\bar{k}_{TOF}$, as in Equation 4.21:

$$k_{1,TOF} = \bar{k}_{TOF} - \frac{a_{0,TOF}}{2} - \frac{a_{1,TOF}}{4} + a_{0,TOF}\,\hat{v}_{\infty,f} + a_{1,TOF}\,\hat{v}^2_{\infty,f} \tag{4.21}$$

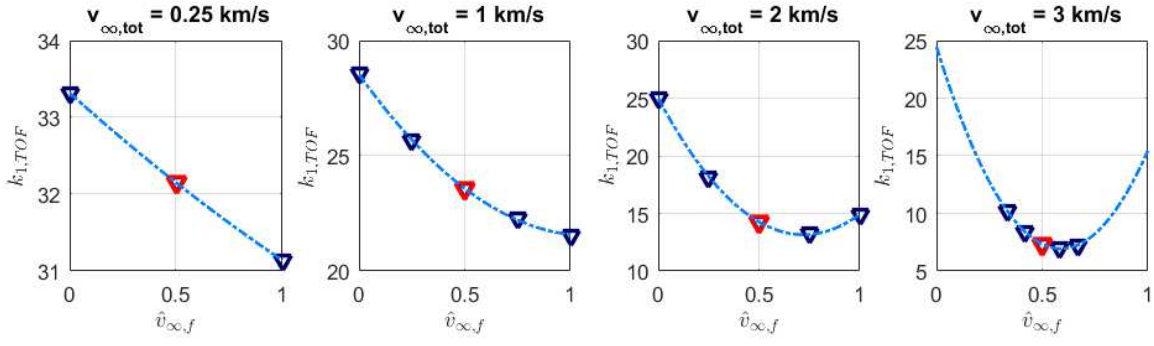

Figure 4.15: Trends of hyperbolic coefficient $k_{1,TOF}$ with respect to $\hat{v}_{\infty,f}$, for four groups of transfers.

Equation 4.21 defines the parabolic correction that should be applied to $\bar{k}_{TOF}$ in order to find $k_{1,TOF}$ for an arbitrary combination of $v_{\infty,i}$ and $v_{\infty,f}$. It is noticed that distinct parabolas (and thus corrections) are identified across groups. First of all, the convexity grows with the total infinity velocity. Moreover, the axis

of symmetry shifts towards lower values of $\hat{v}_{\infty,f}$ for increasing total infinity velocity. These two trends are confirmed by the evolution of $a_{0,TOF}$ and $a_{1,TOF}$ in Figure 4.16. Both coefficients approach zero for small values of $v_{\infty,tot}$, meaning that the correction is not significant in that region of the design space.

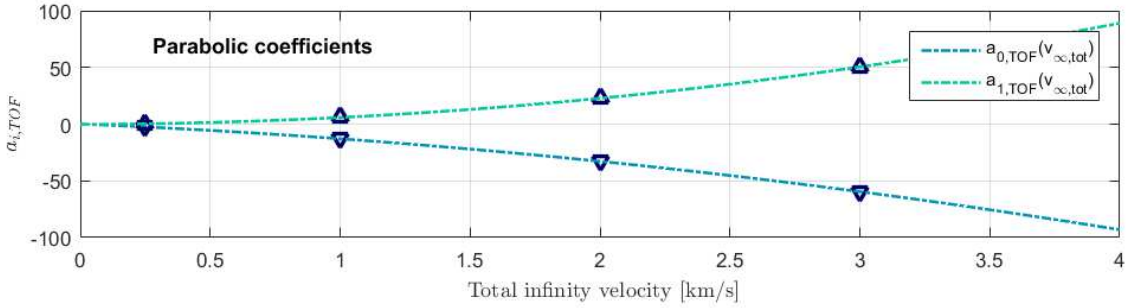

Figure 4.16: Parabolic coefficients a_0 and a_1 with total infinity velocity, for four groups of transfers.

Transfer Angle

Inspection of the transfer angle data across the four groups reveals that the same conclusions can be drawn as for the transfer time. Firstly, k_{1,θ_T} within each group can be approximated by parabolic functions (see top of Figure 4.17). Secondly, with increasing $v_{\infty,tot}$, the convexity of the parabolas becomes more significant and the axis is shifted towards the left.

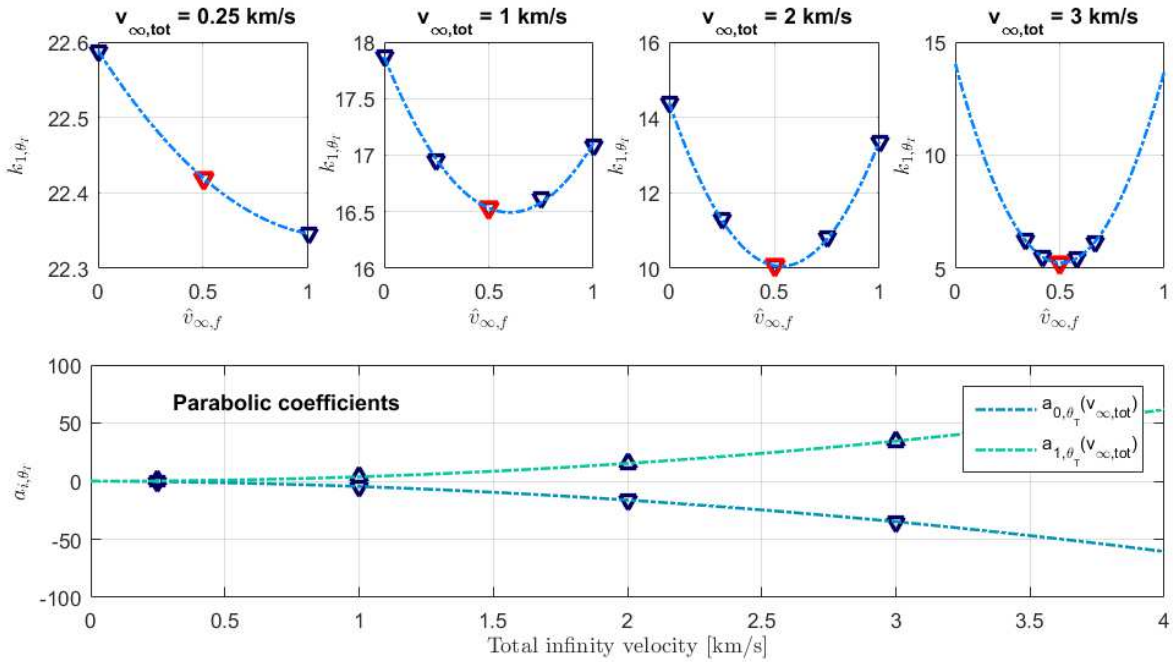

Figure 4.17: Top: trends of hyperbolic coefficient $k_{1,TOF}$ with respect to $\hat{v}_{\infty,f}$, for four groups of transfers.
Bottom: parabolic coefficients a_0 and a_1 with total infinity velocity, for the same groups of transfers.

In conclusion, the same type of correction can be implemented for the transfer angle hyperbolic coefficients:

$$k_{1,\theta_T} = \bar{k}_{\theta_T} - \frac{a_{0,\theta_T}}{2} - \frac{a_{1,\theta_T}}{4} + a_{0,\theta_T}\hat{v}_{\infty,f} + a_{1,\theta_T}\hat{v}^2_{\infty,f} \tag{4.22}$$

Delta-V

The maximum ΔV difference that exists within the groups of transfers amounts to 3.98 m/s, which corresponds to 0.11%. Given the little significance of this error, no correction needs to be implemented for the approximation of the ΔV.

Summary

A summary of all the derived fitting functions needed to implement the parabolic correction on $k_{1,TOF}$ and k_{1,θ_T} is given in Table 4.2. Values of the fit coefficients are also included.

p	**Parabolic correction**	**Parabolic coefficients**	$c_{j,0}$	$c_{j,1}$	$c_{j,2}$
TOF	$k_{1,TOF} = \bar{k}_{TOF} - a_{0,TOF}/2 - a_{1,TOF}/4$ $+ a_{0,TOF}\,\hat{v}_{\infty,f} + a_{1,TOF}\,\hat{v}^2_{\infty,f}$	$a_{0,TOF} = c_{0,0} + c_{0,1}\,v_{\infty,t} + c_{0,2}\,v^2_{\infty,t}$	-3.419336	-9.644566	0.156283
		$a_{1,TOF} = c_{1,0} + c_{1,1}\,v_{\infty,t} + c_{1,2}\,v^2_{\infty,t}$	5.406480	0.676210	-0.191508
θ_T	$k_{1,\theta_T} = \bar{k}_{\theta_T} - a_{0,\theta_T}/2 - a_{1,\theta_T}/4$ $+ a_{0,\theta_T}\,\hat{v}_{\infty,f} + a_{1,\theta_T}\,\hat{v}^2_{\infty,f}$	$a_{0,\theta_T} = c_{0,0} + c_{0,1}\,v_{\infty,t} + c_{0,2}\,v^2_{\infty,t}$	-3.489972	-1.202006	0.092904
		$a_{1,\theta_T} = c_{1,0} + c_{1,1}\,v_{\infty,t} + c_{1,2}\,v^2_{\infty,t}$	3.873142	-0.096548	-0.008495

Table 4.2: Fit functions and coefficients for the parabolic correction.

4.2.4. Conclusions

In the previous paragraphs, the model functions identified for the reference family with zero infinity velocity have been applied to the rest of the database to evaluate the behaviour of the hyperbolic coefficients across families. First inspection of the data highlighted two overlapping trends which led to:

- the identification of total infinity velocity and fraction infinity velocity at arrival as independendent variables;
- the definition of *reference curves* and of *groups*.

The analysis limited to the reference curves produced a number of polynomial functions which model the hyperbolic coefficients with respect to the total infinity velocity. Investigation of the remaining families pointed out that for transfer time and angle a correction to this estimate is needed, if the initial infinity velocity magnitude differs from the final one. The correction has been modelled by a series of parabolas, which also depend on the total infinity velocity. On the contrary, the approximation of the ΔV is considered accurate enough not to require any further correction. Figure 4.18 compares DITAN data with the fitting models that are derived by using the polynomial approximation with $v_{\infty,tot}$, and applying the parabolic correction related to $\hat{v}_{\infty,f}$.

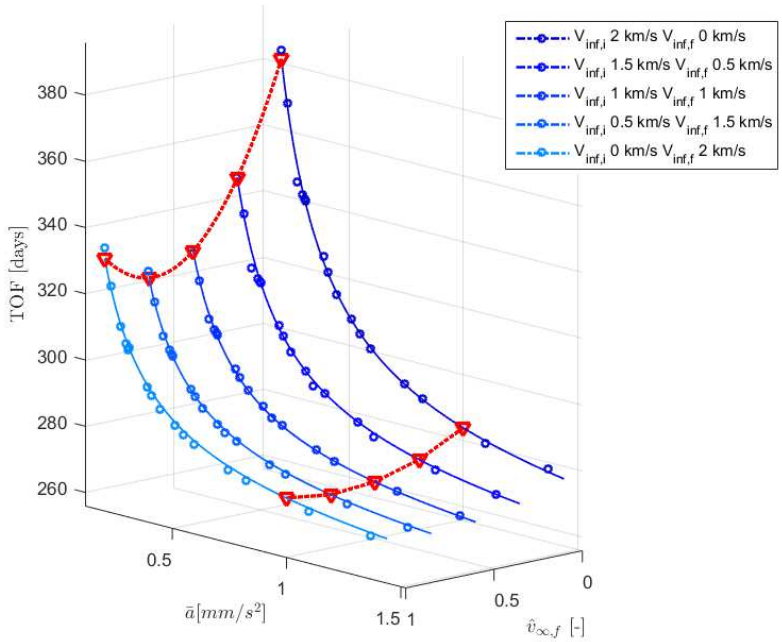

Figure 4.18: DITAN data together with the curves that result from the implementation of the parabolic correction to the reference curve. The quadratic trends are highlighted in red.

4.3. Model Logic

The previous paragraphs have explained the derivation of a number of fitting models, that can be combined together to determine ΔV, time of flight and transfer angle by using the system parameters and the infinity velocities as starting point. To conclude, a procedure that allows to identify the hyperbolic curve $p(\bar{a})$ for each transfer performance parameter p is outlined:

1. from the total infinity velocity, the reference hyperbolic coefficients $k_{i,p}$ and $\bar{k}_p$ are derived by means of polynomial fit functions;
2. from the total infinity velocity, parabolic coefficients $a_{0,p}$ and $a_{1,p}$ are derived by means of parabolic fit functions (if applicable);
3. from the fraction infinity velocity, the correction that determines $k_{1,p}$ is derived from the parabola identified by $\bar{k}_p$, $a_{0,p}$ and $a_{1,p}$ (if applicable);
4. coefficients $k_{i,p}$ are used to uniquely define the hyperbolic function $p(\bar{a})$.

After identification of the curve, input system parameters are used to approximate the mean acceleration $\bar{a}$, and the corresponding three transfer parameters are computed. The logic of the model that is obtained by combining the model functions is displayed in Figure 4.19, showing the flow from inputs to outputs and highlighting each of the fitting elements (tape-like boxes).

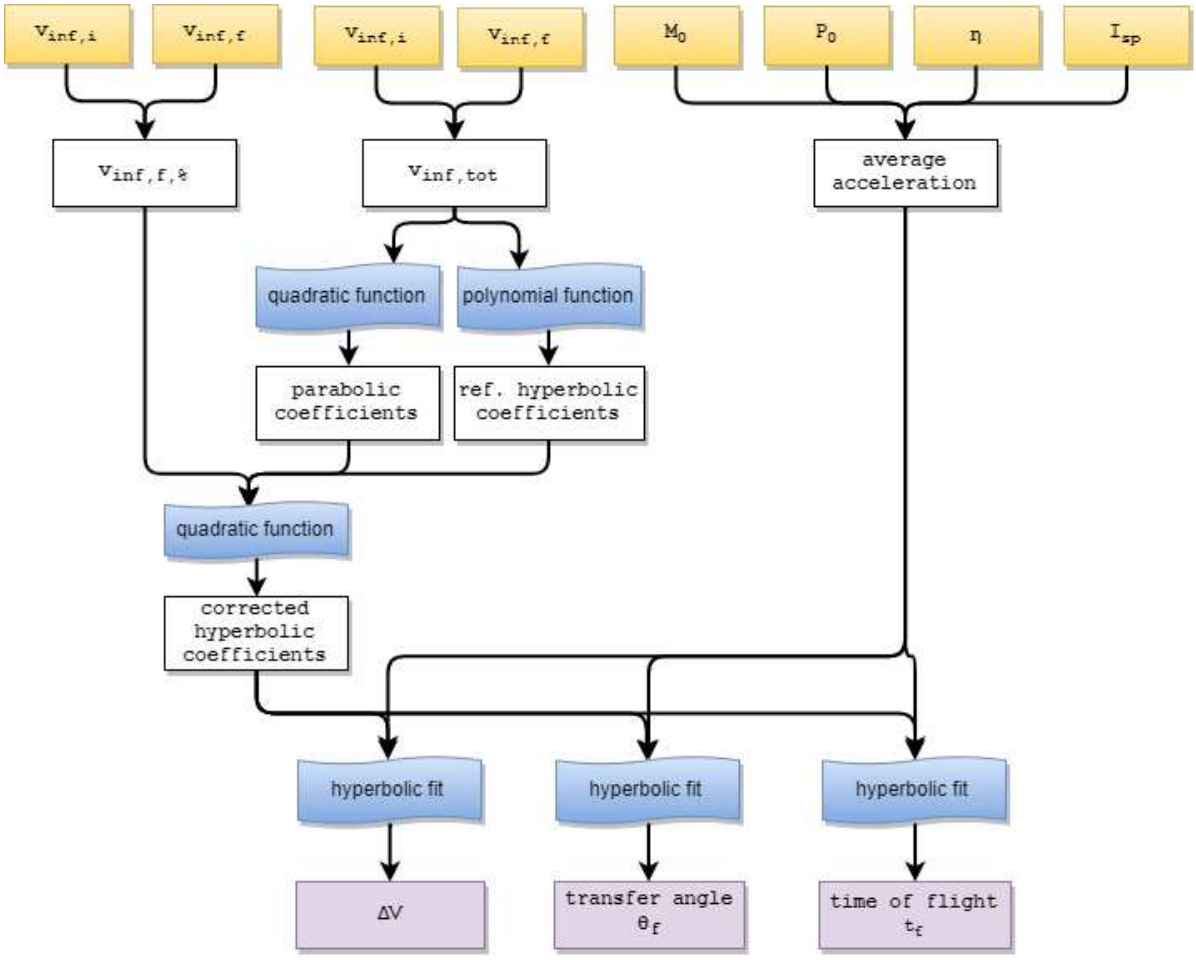

Figure 4.19: Model logic: from input parameters to transfer performance by using a series of fitting elements.

5

Model Architecture

The full logic of the modelling tool includes the approximation of the transfer performance parameters as well as the determination of departure and arrival dates, which for the analysis of interplanetary transfers represents a relevant aspect. While the trajectory parameters have been modelled as outputs of the optimization, the timing of the transfer cannot be derived from DITAN due to the adoption of circular planar orbits. Departure and arrival dates are therefore determined by solving the phasing problem separately, as will be described in Section 5.1. After the derivation of all the elements of the model has been completed, the full logic of the tool is detailed in Section 5.2.

5.1. Departure and Arrival Dates

The transfer time and angle being known for a specific optimal trajectory, determination of the departure date is reduced to a purely geometrical problem. In fact, the waiting time that is needed before initiating the transfer can be computed, so that the final position of the spacecraft matches that of planet Mars.

5.1.1. Phasing

In order to achieve phasing between the planets and the spacecraft, two boundary conditions on the spacecraft angular position need to be satisfied, at beginnning (t_i) and end (t_f) of the transfer:

$$\theta_{SC}(t_i) = \theta_E(t_i) \qquad \theta_{SC}(t_f) = \theta_M(t_f) \tag{5.1}$$

where t_i and t_f are the Julian dates of departure and arrival, while the angular positions of Earth and Mars follow from their angular velocities ω_E and ω_M, as in Equations 5.2:

$$\theta_E(t_i) = \theta_E(t_0) + \omega_E(t_i - t_0) \qquad \theta_M(t_f) = \theta_M(t_0) + \omega_M(t_f - t_0) \tag{5.2}$$

From the application of the model which was the subject of Chapter 4 to a given set of input parameters, the corresponding values of time of flight and transfer angle can be estimated. These are related to the variables of Equations 5.1 to 5.2 by means of the equations below:

$$TOF = t_f - t_i \tag{5.3}$$

$$\theta_T = \theta_{SC}(t_f) - \theta_{SC}(t_i) \tag{5.4}$$

If the conditions of Equations 5.2 are plugged into Equation 5.4, and after some manipulations, the following result is obtained:

$$\theta_T + \theta_E(t_0) + \omega_E \Delta t = \theta_M(t_0) + \omega_M TOF + \omega_M \Delta t \tag{5.5}$$

where $\Delta t = t_i - t_0$. This stands for the waiting time between a guess departure date t_0 and the departure date t_i that enables phasing with planet Mars. It is easily computed from Equation 5.6:

$$\Delta t = \frac{\theta_M(t_0) - \theta_E(t_0) + \omega_M TOF - \theta_T}{\omega_E - \omega_M} \tag{5.6}$$

In conclusion, given a guess departure date t_0 and the outputs TOF and θ_T of the curve-fit model, initial and final longitudes of the interplanetary phase of the transfer are derived by adjusting the time of the beginning of the transfer. The procedure directly produces depature and arrival dates:

$$t_i = t_0 + \Delta t \qquad\qquad t_f = t_i + TOF \tag{5.7}$$

The achievement of phasing and rendezvous with Mars is shown in Figure 5.1, for a given optimal transfer that is represented by the continuous line. The geometry of the transfer departing at guess departure date t_0 is on the left. Phasing with Mars is achieved in this case by waiting about 40 days, as in the plot on the right.

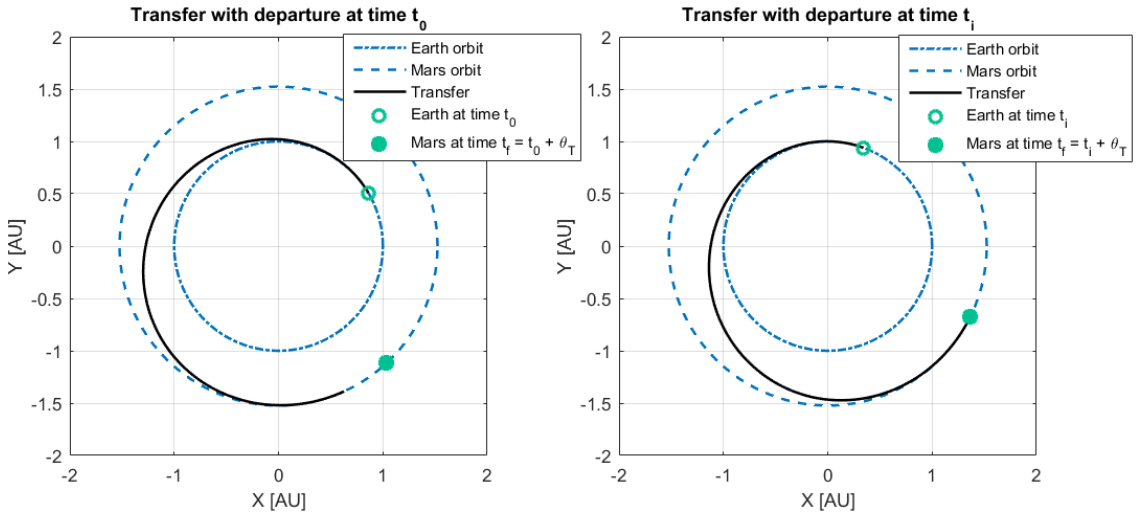

Figure 5.1: Comparison between the geometry of transfers 40 days apart: successful phasing is on the right.

Given the fact that the geometry repeats itself every synodic period, the same type of transfer is feasible for different departure dates, obtained by adding (or subtracting) one or more synodic periods to t_i.
Mars synodic period is about 780 days:

$$T_{syn} = \frac{2\pi}{\omega_E - \omega_M} \approx 778.72 \quad \text{days} \tag{5.8}$$

5.1.2. Analytical Ephemeris

The computation of the waiting time Δt is carried out with respect to a guess departure date t_0 at which the angular position of planets Earth and Mars is assumed to be known. The fastest option to obtain an accurate estimate for the angular position and velocity is the use of analytical planetary ephemerides such as those of [Dysli, 1977]. In this model, orbital elements are expressed as functions of the date t (as Julian centuries since 1900). Polynomial functions up to order three are used [Dysli, 1977]. Orbital elements of Earth and Mars are approximated by the equations of Table 5.1 [1].

Earth	**Mars**
$a = 1.00000023$	$a = 1.523688399$
$e = 0.01675104 - 0.00004180\,t - 0.000000126\,t^2$	$e = 0.0933129 + 0.0000921\,t - 0.0000001\,t^2$
$i = 0$	$i = 1.850333 - 0.000675\,t + 0.000013\,t^2$
$\Omega = 0$	$\Omega = 48.7864417 + 0.7709917\,t - 0.0000014\,t^2 - 0.0000053\,t^3$
$\omega = 101.220833 + 1.719175\,t + 0.000453\,t^2 + 0.000003\,t^3$	$\omega = 285.4317611 + 1.0697667\,t + 0.000131\,t^2 + 0.0000041\,t^3$
$\omega_E = 35999.04975 - 0.000150\,t - 0.000003\,t^2$	$\omega_M = 19139.8585 - 0.0001808\,t - 0.0000012\,t^2$
$\omega = 358.4758 + \omega_E\,t$	$\omega = 319.529425 + \omega_M\,t$

Table 5.1: Analytical ephemeris model made up of polynomial approximating functions [Dysli, 1977].

[1] Some of coefficients have been truncated for brevity.

5.2. Tool Architecture

The full logic of the Earth-Mars transfer computation tool comprises two elements, which have been detailed separately in the current and previous chapters. The first element consists of the curve-fit model, which was derived by analyzing DITAN outputs for mass optimal transfers. It takes as inputs:

- *system parameters*: initial mass, power at 1 AU, specific impulse and system efficiency;
- *infinity velocity* at departure and arrival.

By combining a number of fitting blocks, it computes estimates for ΔV cost of the transfer, as well as transfer time and angle. Its logic is displayed in the upper box of Figure 5.2. The second element is represented in the box at the bottom of the same figure. It uses the transfer time and angle values that are the outputs of the curve-fit model, together with analytical ephemerides, to complete the geometrical phasing with Mars. Figure 5.2 combines both elements in the complete architecture of the modelling tool.

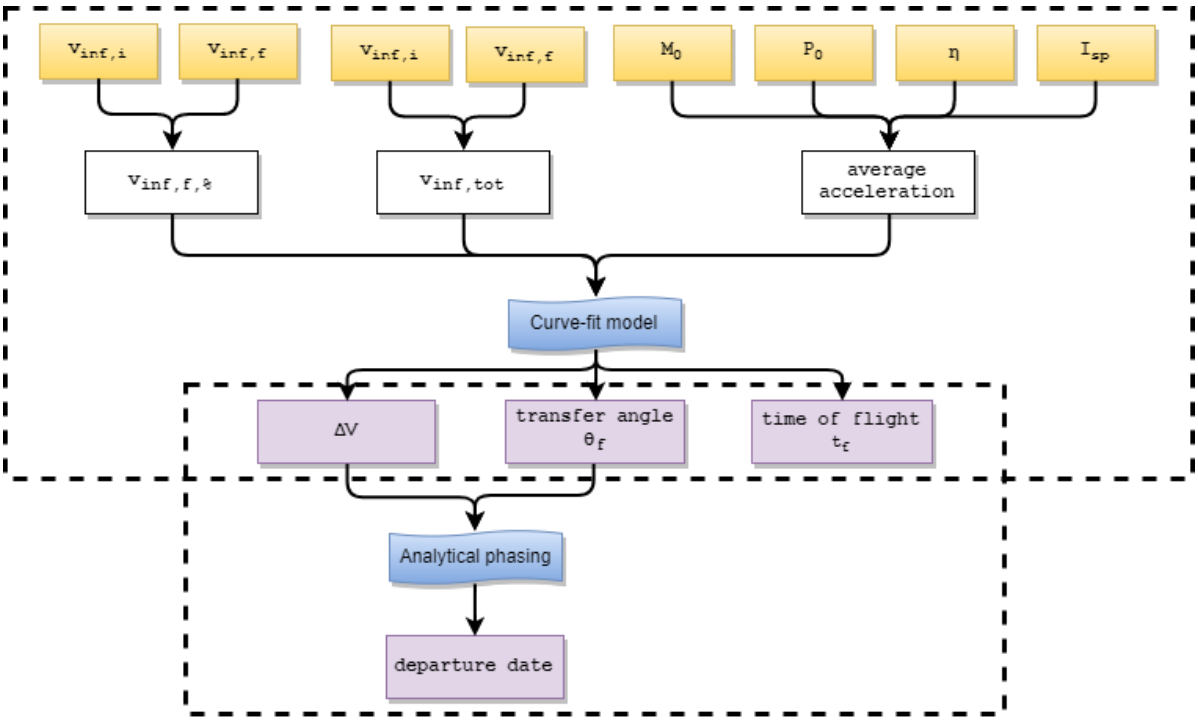

Figure 5.2: Full architecture of the modelling tool: curve-fit model and phase solver.

The architecture of Figure 5.2 was implemented both as a set of Matlab functions and in an Excel worksheet, that also allows visualization of the geometry of the transfer and parametric analysis of the inputs. As was pointed out during the setup of the database, and specifically in Subsection 3.1.2, the thrust-to-mass ratio at 1 AU and the specific impulse account for all aspects of the propulsion system that are relevant to this study. For the generation of the transfers, it was decided to use fixed values of initial mass and system efficiency, while varying power at 1 AU and specific impulse to cover the entire acceleration range of interest. However, typically the set of inputs available could differ from the one used in this study. Therefore, both implementations of the modelling tool have been structured so as to accept different combinations of system input parameters:

1. thrust-to-mass ratio and specific impulse: m_0, T_0 and I_{sp};
2. power-to-mass ratio, efficiency and specific impulse: m_0, P_0, η and I_{sp}.

6

Results and Performance Assessment

For academic results and conclusions to be reliable and credible a process of testing, verification and validation is required, that is designed for the specific project/product. The assessment of the results and the performance of the model has been therefore structured into a number of independent stages, which are depicted in Figure 6.1. The aim of each element is summarized below:

1. **Residual Analysis**:
   The significance and the distribution of the residuals are analyzed on the entire dataset, in order to evaluate the propagation of the errors of each fitting model up to the final estimates of the trajectory parameters.

2. **Testing and Verification**:
   The model is verified by assessing its performance on independently generated test cases, which cover the entire design space and are derived in the simplified dynamical environment.

3. **Full Ephemeris Model Comparison**:
   The approximate transfers that are produced by the modelling tool in the simplified dynamics are compared with transfers which are optimized in the full ephemeris model. Conclusions are drawn not only with respect to the accuracy, but also with respect to attributes such as specificity, efficiency and suitability, in order to further detail the impact, the capabilities and the limitations of the result.

Each of the three steps of the process is dealt with in one of the sections that compose the present chapter.

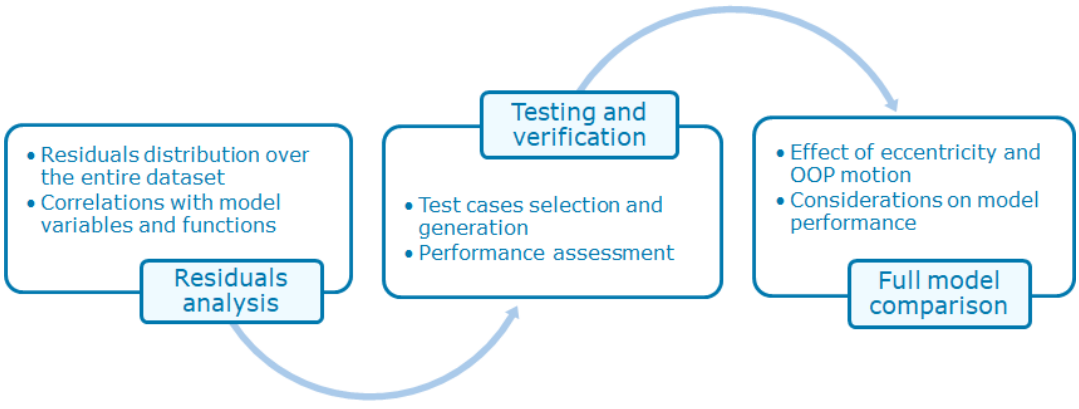

Figure 6.1: The three stages of the model performance assessment.

6.1. Residuals Analysis

While the goodness of each model function has been evaluated at the time of the fitting, the combination of such functions into a more complex architecture could lead to a significant propagation of the errors to the trajectory metrics estimates. For this reason, the modelling tool is applied to each of the set of inputs that were selected for the generation of the database, and used to estimate the corresponding trajectory metrics. Unlike in Chapter 4, in which each element of the model was analyzed independently, this section deals then with an assessment of the overall accuracy of the model.

6.1.1. Residuals Distribution

In the coming paragraphs, residuals are expressed in terms of percent error, and their distribution is studied with respect to each of the independent variables used for the modelling, namely average acceleration, total infinity velocity and fraction infinity velocity.

Average Acceleration

A first examination of the data shows that all errors are within 0.11% for the ΔV, 1.6% for transfer time and 1.2% for transfer angle. If also the root mean square of the residuals is expressed as a percentage, the following errors are derived:

$$\text{rms}_{\Delta V,\%} = 0.016\% \qquad \text{rms}_{TOF,\%} = 0.306\% \qquad \text{rms}_{\theta_T,\%} = 0.238\% \tag{6.1}$$

It can be observed from the distribution of the residuals that the errors are typically greater for lower values of the average acceleration. This is associated with the shape of the model functions and can be traced back to the residuals of Section 4.1. Moreover, by exploring Figure 6.2, one can notice that the most significant erros are related to specific families of transfers. With regard to the ΔV, percent errors greater than 0.05% correspond to the families 2-0, 1.5-0.5, 2-1 and 1-2. This is explained by the use of the coefficients of the reference curves for the entire group of families. Nonetheless, errors are well within the bounds specified and this correlation should not be the cause of great concern. As for transfer time and transfer angle, the two distributions of residuals mirror each other. Errors are greater than 0.5% for specific families, which can be explained by the values of infinity velocities, as in the following.

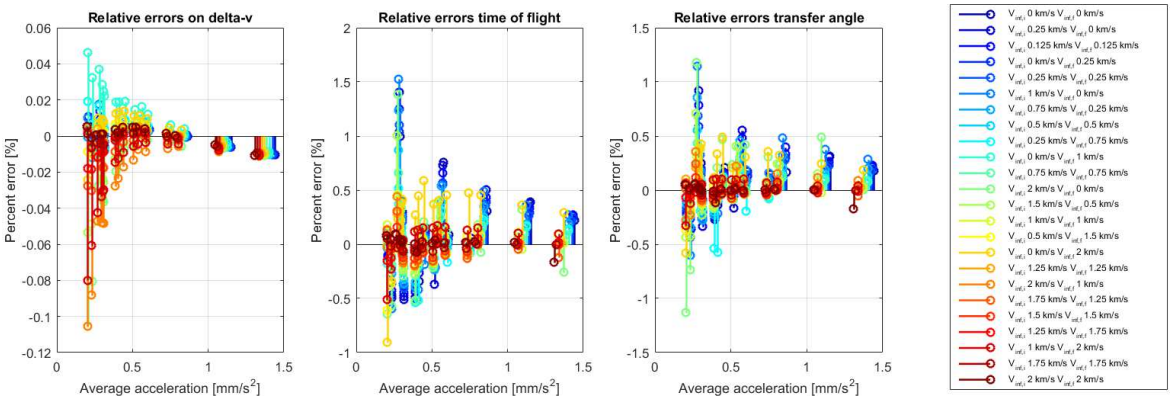

Figure 6.2: Residuals distribution with respect to average acceleration levels, for the entire dataset.

Fraction Infinity Velocity

Examination of the same residuals according to the fraction infinity velocity at arrival clarifies the remaining trends in their distribution. The left-hand side of Figure 6.3 confirms that, for the ΔV, the errors grow within each group when moving away from the reference case ($\hat{v}_{\infty,f}$). This appears very clearly when observing for example the red groups, including all families with $v_{\infty,tot} = 3$ km/s. Also for transfer time and transfer angle a similar trend is observed, with greater errors for low and high $\hat{v}_{\infty,f}$. This is due to the combination of the uncertainty on the reference hyperbolic coefficients with the inaccuracies brought about by the parabolic correction. Exceptions are the families 0-0, 0.125-0.125 and 0.25-0.25, that are located on the reference plane. For those, errors are traced back at the fitting over the reference curves.

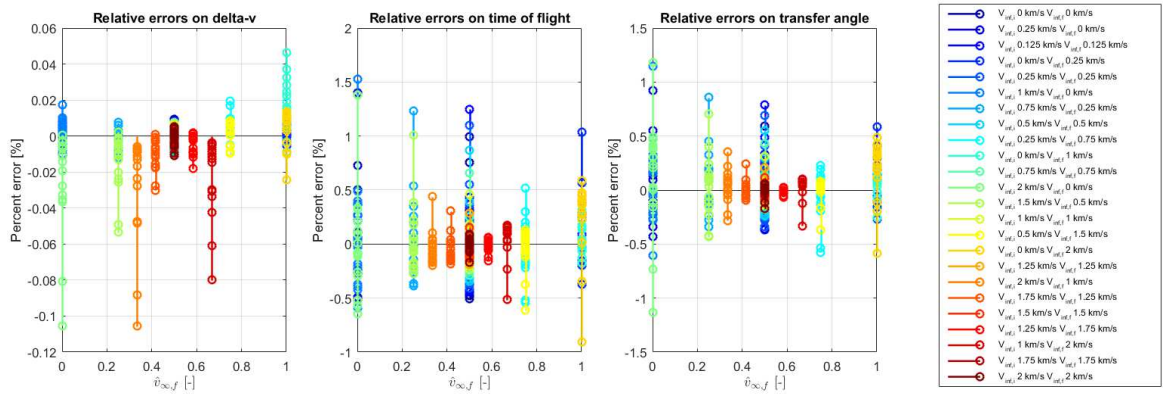

Figure 6.3: Residuals distribution with respect to fraction infinity velocity at arrival, for the entire dataset.

Total Infinity Velocity

To be thorough, the distribution has also been displayed against the total infinity velocity. No further trends are identified, besides the dependencies on average acceleration and fraction infinity velocity that have been already discussed.

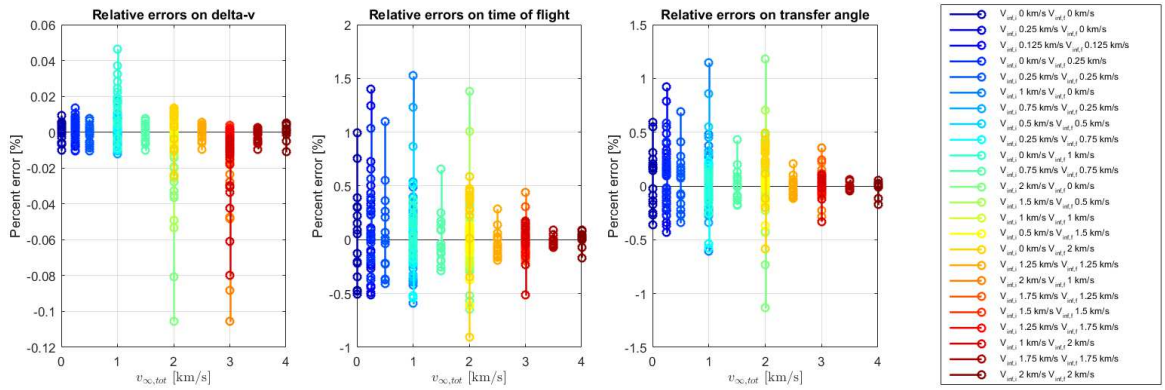

Figure 6.4: Residuals distribution with respect to total infinity velocity, for the entire dataset.

6.1.2. Conclusions

Detailed analysis of the residuals distribution has been carried out in order to identify bounds, typical values and trends of the errors. For each of the trajectory parameters, the accuracy achieved is reported in Table 6.1 in terms of maximum percent error and root mean square. In summary, errors are found to grow, within the limits reported, for lower values of the average acceleration, and when moving away from the reference curves for small and great values of fraction infinity velocity at arrival.

Parameter	*Bounds*	*Typical errors* (RMS)
ΔV	+0.046/-0.106 %	0.016%
TOF	+1.526/-0.906 %	0.306%
θ_T	+1.179/-1.133 %	0.238%

Table 6.1: Accuracy of the curve-fit model, as estimated from the residuals analysis.

6.2. Testing and Verification

Having identified by means of the residuals analysis the expected performance with respect to ΔV, time of flight and transfer angle, accuracy levels need to be verified using test cases that are independent of the dataset used for the derivation of the model. The purpose of the verification is twofold:

- to quantify the model accuracy in relation to optimal transfers which are generated independently from the original data, in the simplified dynamical model;
- to compare the figures with the requirements specified in Chapter 1, to assess the suitability of the model for the intended purpose.

6.2.1. Test Cases Selection

Testing of the modelling tool is carried out by using dedicated test cases, that are optimized with DITAN in a fashion similar to what described in Chapter 3. The rationale behind this choice takes two aspects into consideration. First, given the specificity of the models and assumptions adopted, few results in literature have a similar set up, and none has been found that considers non-zero values of infinity velocities. Moreover, the aim is the generation of a number of samples that cover the entire design space. Design of *ad hoc* test cases allow to define the desired pattern and choose the resolution for their distribution over the design space.

A large number of possible combinations of input parameters has been generated randomly. Eighteen have been chosen, according to a specific logic. In order to span over the entire thrust-to-mass ratio range, the combinations of the system parameters are such that six test cases are in the range $0.2-0.6$ mm/s^2, six in the range $0.6-1$ mm/s^2 and the final six in the range $1-1.8$ mm/s^2. The three groups are identified in Figure 6.5 by the symbols triangles, diamonds and circles, respectively. Furthermore, the combinations of infinity velocity at departure and at arrival sample the design space so that within each of the three groups, three test cases have total infinity velocity higher than 2 km/s, while the remaining three have $v_{\infty,tot} < 2$ km/s. At last, in each subgroup one sample presents prevalence of infinity velocity at departure $\hat{v}_{\infty,f} << 0.5$, one the opposite situation $\hat{v}_{\infty,f} >> 0.5$ and the third one is in between ($\hat{v}_{\infty,f} \approx 0.5$). The pattern that was just described is summarized in Figure 6.5. Grey areas have been filled to point out that no transfer of the database, as well as no test case, can fall in those regions due to the way the design parameters were defined. In order to be in the top left region, for example, a departure infinity velocity higher than 2 km/s is required.

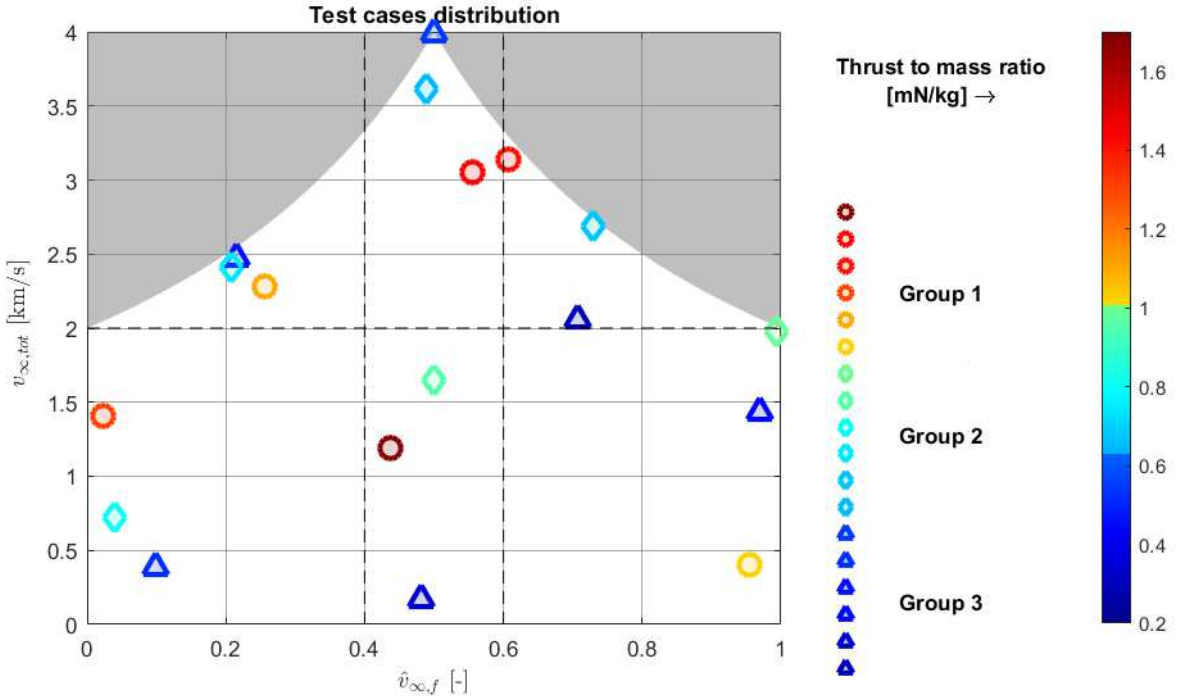

Figure 6.5: Distribution of the 18 test cases over the design space, in relation to thrust to mass ratio and infinity velocities.

6.2.2. Results and Conclusions

Each of the set of inputs selected in Subsection 6.2.1 was individually optimized with DITAN and the outputs in terms of ΔV, time of flight and transfer angle were extracted. The results are compared with the curve-fit model outputs in Figure 6.6 (ΔVs are displayed after removal of the offset).

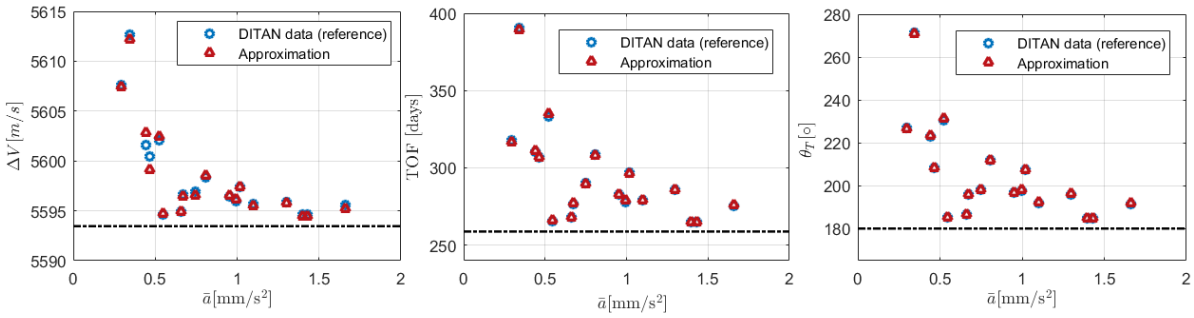

Figure 6.6: DITAN and curve-fit model outputs are compared with respect to ΔV, transfer time and transfer angle.

The performance is more effectively evaluated in terms of percent errors against average acceleration levels, as in Figure 6.7. Each column corresponds to one of the performance parameters, respectively ΔV, transfer time and transfer angle, while the two rows contain the same graphs, with the only difference in the colormap. Double visualization allows to correlate relative errors with all relevant variables, with the conclusions:

- **Maximum errors**: the bounds identified by the percent errors confirm that all errors are within +0.03/-0.05% for ΔV, within +0.54/-0.35% for transfer time and within +0.40/-0.25% for transfer angle;
- **RMS**: RMS of the errors is 0.013% for ΔV, 0.22% for transfer time and 0.16% for transfer angle;
- **Trends**: errors are greater for lower average accelerations and for transfers distant from reference ones.

This assessment confirms what has been discussed in terms of accuracy during the analysis of the residuals (Section 6.1). By comparing the figures determined above with the goals defined in Subsection 1.3.2, it is concluded that the model performance is more than compliant with the requirement of 5% accuracy for all transfer parameters. Errors are for all test cases, as well as on the original dataset, well within 1%.

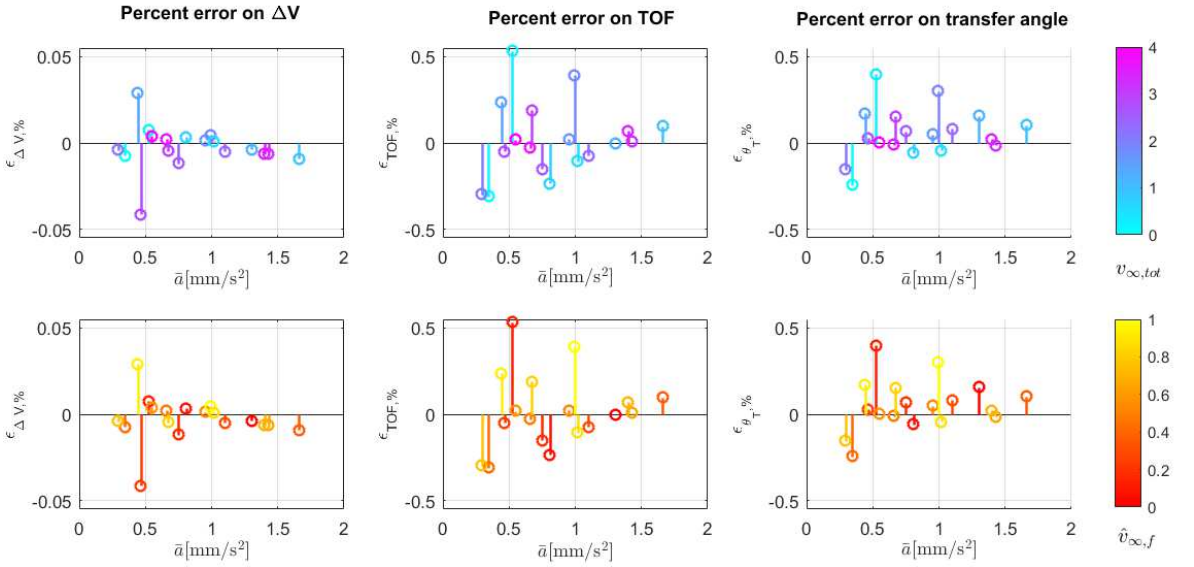

Figure 6.7: Percent errors of ΔV, time of flight and transfer angle against average acceleration levels, depending on the total infinity velocity and fraction infinity velocity at arrival.

In the following the relative errors are shown in different fashions, to better visualize the trends mentioned above. As in Figure 6.7, each column corresponds to one of the performance parameters, while the independent variable is either the total infinity velocity (first two rows) or the fraction infinity velocity at arrival (last two rows). Figure 6.8 confirms that larger errors are typically associated with lower acceleration levels (blue elements of rows 1 and 3). Furthermore, rows 3 and 4, which depict the errors distribution against $\hat{v}_{\infty,f}$, show that the relative errors are in general smaller when close to the reference curves (middle part of the graphs) than when moving towards an uneven distribution of infinity velocity between departure and arrival (outer part of the plots).

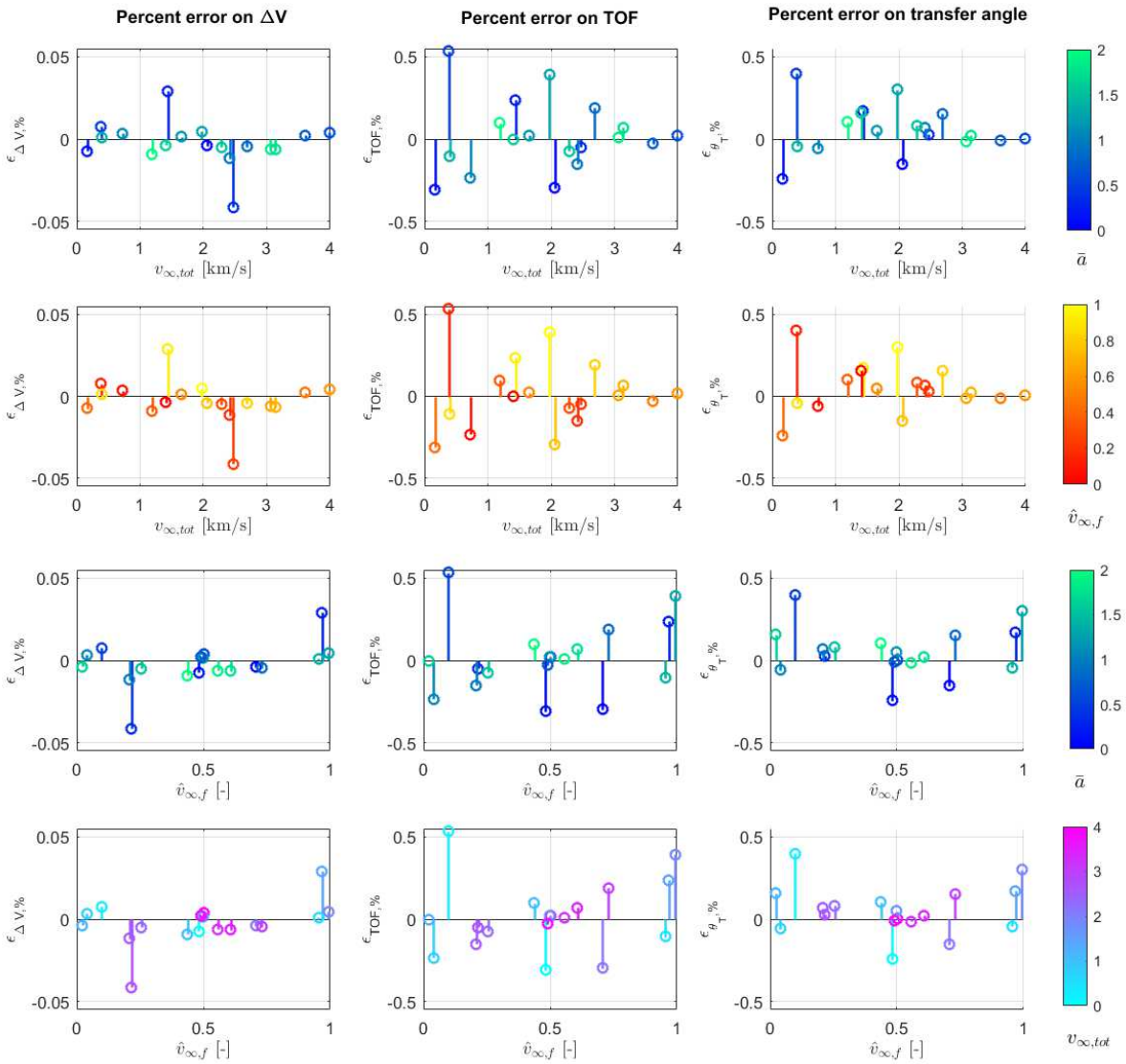

Figure 6.8: Percent errors of ΔV, time of flight and transfer angle against total infinity velocity and fraction infinity velocity at arrival, depending on the remaining model variables.

6.3. Full Ephemeris Model Comparison

This section is concerned with the assessment of the model performance with respect to transfers optimized in the full ephemeris model. The purpose is the verification of the compliance with the requirements established in Chapter 1 and of the suitability of the method for the intended application. The optimization was carried out in a more complex dynamical environment, which includes the use of 3D dynamics with real ephemerides of planets and free direction for infinity velocities. This implies:

1. motion during the transfer is not restricted to the ecliptic;
2. initial and final orbits are defined by means of ephemeris data;
3. infinity velocities direction is optimized and not necessarily tangential.

As it becomes evident from the list above, the main purpose is the evaluation of the effect of the eccentricity of the orbits and of the out-of-plane motion. No perturbation has been accounted for, including third-body contribution at beginning and arrival, meaning that the analysis is limited to the interplanetary cruise.

6.3.1. Test Cases Selection

The four test cases that have been individually optimized in the full ephemeris model have all departure dates in the same synodic period, and specifically in the timeframe September/October 2026. This enables to have a similar geometry between the transfers, and therefore to better compare transfers that have a different set of input parameters. The relevant input parameters for the four cases are summarized in Table 6.2.

Synodic Period

The choice for this specific year for the investigation is driven by the fact that mass-optimal transfers with less than one revolution departing in late 2026 fall in the thrust-coast-thrust profile regime, as on the right of Figure 6.9. On the contrary, when using DITAN to optimize transfers departing in the following or preceding synodic period, a different regime is found, for example the five-subarc profile (left side of Figure 6.9). This does not mean that thrust-coast-thrust transfers are not possible for those launch opportunities, but simply that propellant mass can be saved by adopting five subarcs. Since DITAN does not allow for forcing a specific thrust profile, the comparison with transfers departing in 2028 or 2024 is not meaningful, as those transfers violate the thrust-coast-thrust assumption. For a further assessment of how the model performs over the years, a different optimizer should be used, that allows to define a specific sequence of thrust and coast arcs.

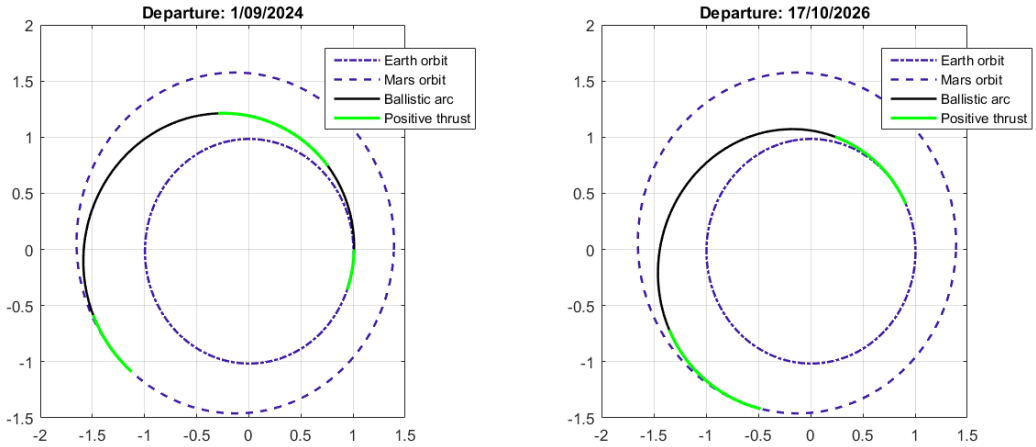

Figure 6.9: Geometry and thrust profiles of transfers with the same set up, with departure in 2024 (left) and 2026 (right).

Input Parameters

Four transfers were selected with different values of system parameters and infinity velocities, to identify potential correlation between those and the significance of the errors. Three values of the thrust-to-mass ratio at 1 AU are used, specifically 0.389, 0.556 and 0.625 mN/kg. Figures of initial mass and thrust, specific impulse and infinity velocities are listed in Table 6.2.

Transfer #	T_0 [mN]	m_0 [kg]	I_{sp} [s]	$v_{\infty,i}$ [km/s]	$v_{\infty,f}$ [km/s]
1	0.5	900	3000	0	0
2	0.35	900	4010	1	0
3	0.5	800	3000	1	1
4	0.5	800	3000	2	0.5

Table 6.2: Input parameters of the four transfers optimized in the full dynamical model.

6.3.2. Results

Unlike previous assessments, this analysis includes all the elements of the modelling tool and conclusions can be drawn not only with respect to trajectory parameters, but also to the launch window determination. The four test cases are visualized in Figures 6.10 to 6.13 as projections of the spacecraft path onto the ecliptic. Initial and final orbits are also displayed, both as real eccentric orbits and as circular approximations. The first consideration to be made is that the significance of all errors is similar across all test cases, meaning that a correlation with the input parameters is not found, or it represents noise compared to the other effects.

Delta-V

ΔV errors are negligible for all transfers, since they never exceed 1%, independent of the values of the infinity velocities. This suggests that the the way infinity velocities have been expressed by means of boundary conditions for the tangential velocity successfully represent the real behaviour, as confirmed later.

Transfer Time

Errors in the estimation of the time of flight range between 12.2 and 14.8% for the four transfers. All of them are in the full ephemeris model about 50 days longer than the approximation, regardless of the individual setup. This suggests that the error is due to the specific geometry of the transfers: because of the eccentricity of Mars orbit the rendezvous with the planet is delayed, lengthening the transfer. Analysis of other launch opportunities could clarify this point and assess the impact of the geometry on the tranfer time error, but, due to the unavailability of suitable optimization tools, is left for future work.

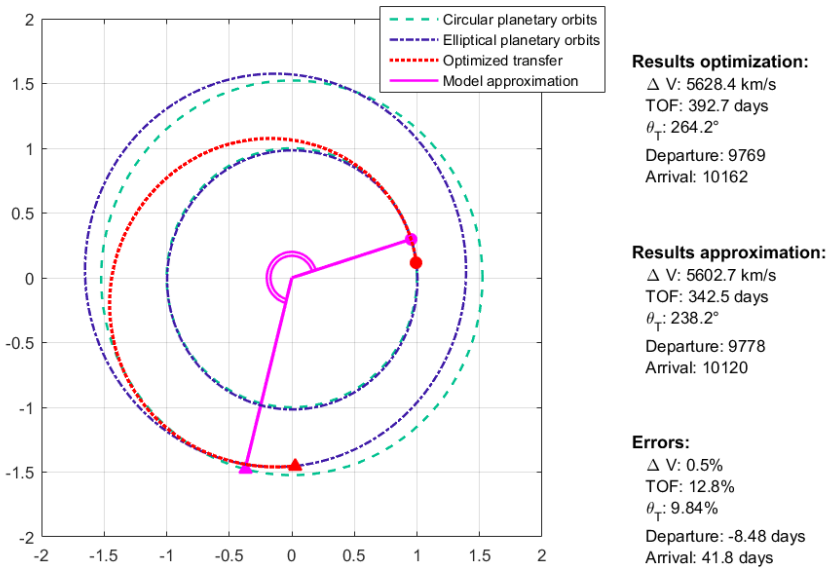

Figure 6.10: Comparison between approximated solution and optimized transfer in the full dynamic model: $T/m|_0 = 0.556$ mN/kg, $v_{\infty,i} = 0$ km/s, $v_{\infty,f} = 0$ km/s.

Transfer Angle

Considerations on the tranfer angle errors directly reflect those drawn for the tranfer time. Percent errors span over the range 9.8-11.3%.

In the following, visualization of the trajectory optimal paths and corresponding approximations is displayed for the remaining cases. On a more general note, it is noticed that the estimated departure date and transfer time provide very useful information for propagation of known thrust laws to generate suitable initial guesses. In the author's experience, if a guess departure date is available, adjusting the thrust levels and propagating the control law in time so as to reach Mars in the guessed transfer time normally provides a very good guess for further optimization of this type of transfers.

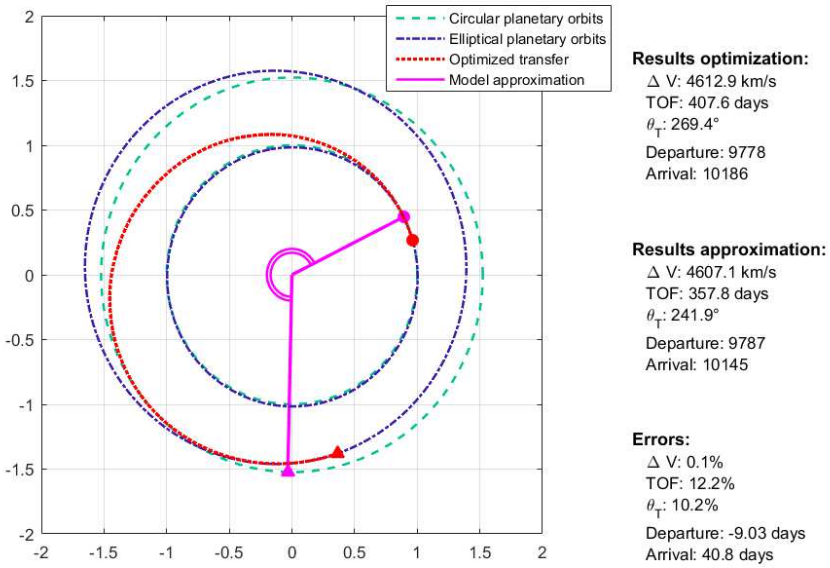

Figure 6.11: Comparison between approximated solution and optimized transfer in the full dynamic model: $T/m|_0 = 0.389$ mN/kg, $v_{\infty,i} = 1$ km/s, $v_{\infty,f} = 0$ km/s.

Moreover, it is pointed out that the trajectory parameters are produced in milliseconds for any combination of inputs, making the model very suitable for a broad search of the design space and a fast assessment.

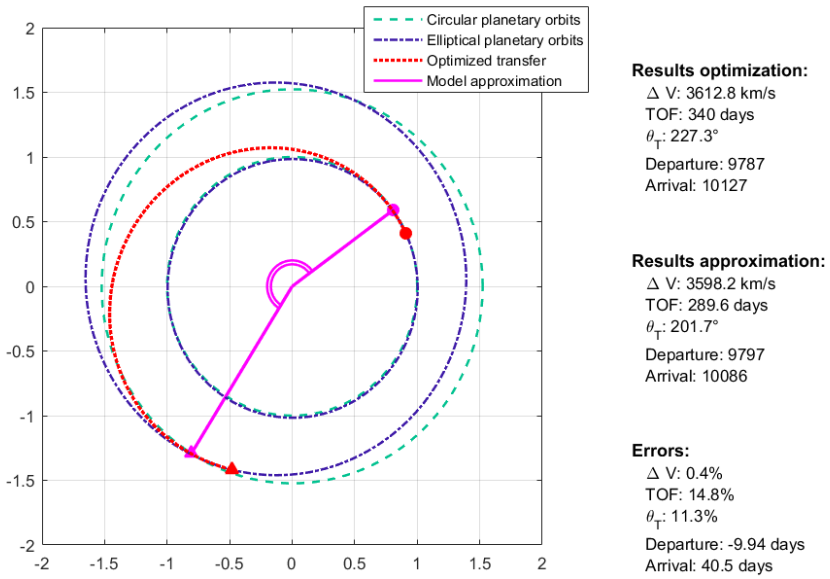

Figure 6.12: Comparison between approximated solution and optimized transfer in the full dynamic model: $T/m|_0 = 0.625$ mN/kg, $v_{\infty,i} = 1$ km/s, $v_{\infty,f} = 1$ km/s.

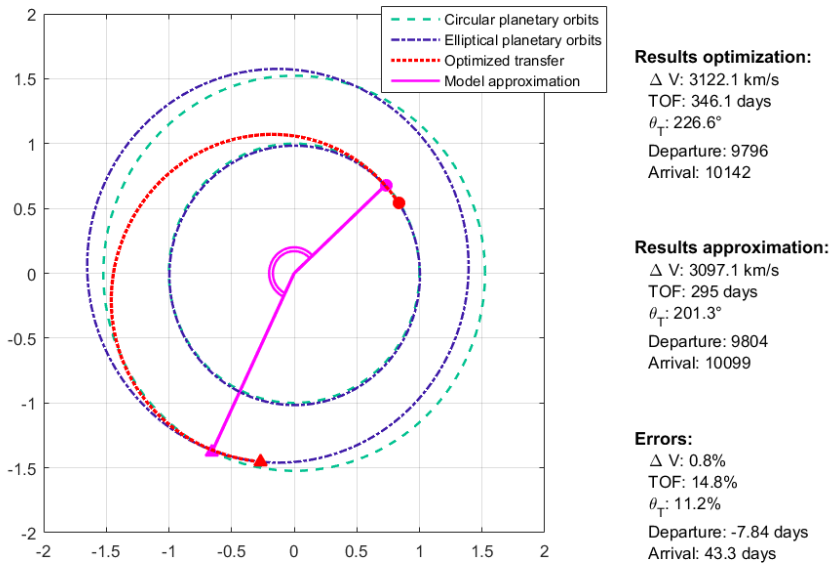

Figure 6.13: Comparison between approximated solution and optimized transfer in the full dynamic model: $T/m|_0 = 0.625$ mN/kg, $v_{\infty,i} = 2$ km/s, $v_{\infty,f} = 0.5$ km/s.

6.3.3. Direction of Infinity Velocity

The direction of the infinity velocities is analyzed to draw considerations with regard to the assumption of tangential infinity velocity. Figure 6.14 presents the results of this assessment, by comparing the radial component (dark bars) with the component that lies on the plane tangential to the trajectory[1]. The assessment confirms that also when the direction of the infinity velocity is given freedom, the direction tangential to the trajectory is a very good approximation of the results obtained for optimal transfers.

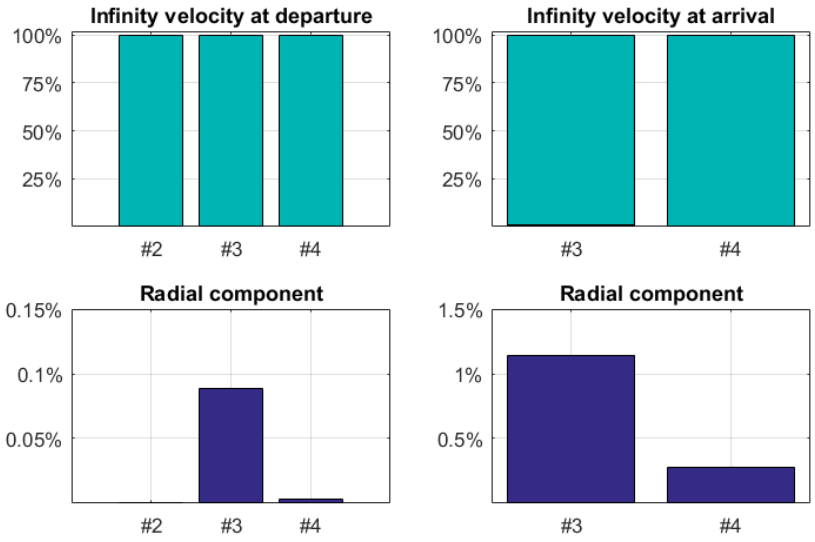

Figure 6.14: Assessment of the components of the optimized infintiy velocities, for cases 2 to 4. Dark bars represent the radial components, and are barely visible in the top graph, reason why their percent contribution has been highlighted, at the bottom.

[1] Since the motion is optimized in the 3D model, also the out-of-plane component needs to be taken into account.

6.3.4. Conclusions

Detailed analysis of four test cases has been carried out in order to identify bounds and trends of the errors. For each of the relevant parameters, typical errors are reported in Table 6.3. Some conclusions are drawn:

- **Model performance:**
  Typical values of the errors are within 1% for the ΔV, between 12.2 and 14.8% for the time of flight and between 9.8 and 11.3% for the transfer angle. This results in an excess time of about 50 days for all transfers, 8-10 days distributed at departure, while the remaining on the arrival date. This is in agreement with the requirements of early-stage concept development, as established in Chapter 1. Moreover, the demonstrated efficiency and simplicity of implementation of the method confirm the suitability for fast and broad assessments.

- **Error distribution:**
  Errors do not appear to be correlated with the different setup of the test cases. This suggests that the inaccuracy is mainly associated with the geometry of the transfers, that differs from the circular planar simplification.

- **Direction of the infinity velocity:**
  It has been shown that when transfers are optimized in the full ephemeris model and no bounds are provided for the infinity velocity direction, the optimal direction is very close to tangential, thus legitimating the simplification adopted in the study.

- **First-guess generation:**
  Approximations of departure date and transfer time provide a valid starting point for the generation of a first guess for the optimization process. In fact, the significance of the errors is, in the author's experience, acceptable for proper adjustment of the control law propagation. In order to use the outputs of the curve-fit model to provide a propagated initial guess, the strategy advised consists in:

  1. propagating tangential continuous thrust from the estimated departure date;
  2. adjusting the initial thrust levels so that the propagated solution reaches Mars orbit in the estimated transfer time.

- **Future work:**
  In order to assess the impact of the geometry over different years and launch opportunities, a different optimizer that allows to force a specific arc sequence is required.

Parameter	*Minimum errors*	*Maximum errors*
ΔV	0.1%	0.8%
TOF	12.2%	14.8%
θ_T	9.8%	11.3%
Departure date	7.84 days	9.94 days

Table 6.3: Model accuracy with respect to transfers optimized in the full ephemeris model.

7

Conclusions

A novel technique for the assessment of the performance of Solar Electric Propulsion transfers to Mars is proposed, which is based on the analysis and fitting of a database of pre-optimized trajectories. The motivation for the development of such a model is the lack of available medium-to-low fidelity design tools for SEP missions, that allow fast computation of transfer performance parameters in the frame of preliminary assessments and early-stage design. During high-level concept development, the availability of fast and simple models enables to carry out analysis of a broad search space and to characterize several options. The methodology that is proposed consists in the identification and modelling of the underlying relations of a large trajectory dataset, and leads to the derivation of a number of fit models that accurately approximate the transfer performance in terms of ΔV cost, transfer time and transfer angle, including a wide range of system parameters and of departure and arrival infinity velocities.

7.1. Conclusions

It has been shown that a large dataset of optimal Earth-Mars transfers can be produced in a semi-automatic way, that characterizes a wide design space and includes not only several system parameters, but also a significant range of departure and arrival infinity velocities. A limited number of variables and analytic relations successfully describes the underlying trends in such a database. Modelling of the trends by means of curve-fitting positively identifies those relations, dealing with the effect of the infinity velocities as well. The main difficulty encountered in the modelling phase is related to the presence of different regimes in the database. To avoid major inaccuracies, the restriction to the thrust-coast-thrust profile is needed. On this class of transfers, the accuracy of the model that has been derived results in a maximum of 1.6% error for the three trajectory parameters, namely ΔV, transfer time and transfer angle, which is well within the requirements. This level of model performance confirms the consolidation of a modelling methodology that can be applied to other datasets with similar structure. The accuracy with respect to transfers derived in the full ephemeris model is well within 15% for all transfer parameters, in compliance with the requirements of early-stage mission concept development. This, together with the efficiency and simplicity of the method, makes the developed tool suitable for such assessments, and for the generation of initial guess solutions for optimization.

The considerations that have just been summarized are further detailed in the following two subsections. The research objectives and corresponding tasks that are identified in Sections 1.3 and 1.4 have been expanded into a number of assessments. Although the activities have been organized into three distinct phases, the considerations that were drawn are not simply listed accordingly, but they are reorganized so as to separately answer the two main research questions formulated in Subsection 1.3.2. In fact, Subsection 7.1.1 not only addresses the problem formulation and the database generation of Chapters 2 and 3, but also reports all the findings related to the transfers characterization and analysis that were derived throughout the project. Later on, in Subsection 7.1.2, the conclusions dealing with the model derivation and assessment are summarized.

7.1.1. Answer to the First Research Question

The first research question and related sub-questions are reported here for easy reference:

RQ1 - *How can quantitative data be generated so as to effectively capture the main characteristics of mass optimal Earth-Mars transfers using solar electric propulsion?*

- **RQ1.1** - *What simplifications/assumptions in the problem description are needed to escape the diversity and complexity of such transfers without causing major inaccuracies?*
- **RQ1.2** - *For generation of a representative dataset, which are the key variables and which is the range of interest and the required resolution for each of them?*
- **RQ1.3** - *What are the characteristics of the corresponding transfers in terms of thrust profile, number of revolutions and typical values of transfer performance parameters?*

Problem Modelling

In the frame of interplanetary cruise between Earth and Mars, adoption of the two-body problem, only perturbed by the thrust acceleration, is well suited for preliminary trajectory design. With regard to the infinity velocity modelling, the assumption of tangential direction has been validated by the analysis of transfers optimized in the full ephemeris model, conducted with no bounds on the velocity direction. The modelling of SEP propulsion system is achieved by means of inverse-square power loss law, that is extended to the thrust since a fixed specific impulse is considered, as it is representative of current SEP systems. The characteristics of the propulsion system that are relevant to the trajectory analysis are thrust-to-mass ratio and specific impulse, which are successfully captured by the use of the average acceleration as variable.

Transfer Characterization

In the investigated acceleration range, transfers have been found to follow either a three sub-arc thrust profile, for transfers shorter than one revolution, or a five sub-arc profile, for transfers between one and two revolutions. The transition between the two regimes occurs for a specific value of average acceleration, that varies across families depending on the infinity velocity values. However, transfers with a mean acceleration higher than 0.2 mm/s^2 follow the thrust-coast-thrust profile for any combination of infinity velocities. This range corresponds to approximately 90% of the original acceleration vector.

Relevant Variables

Three variables have been identified for proper description of the underlying trends: the average acceleration $\bar{a}$, the total infinity velocity $v_{\infty,tot}$ and the fraction infinity velocity at arrival $\widehat{v}_{\infty,f}$. In particular, the average acceleration allows better comparison between systems, and therefore more regular trends, because it includes both initial thrust levels and specific impulse. Although it is not an input to the problem, it can be very accurately estimated from the inputs (the maximum error in the entire dataset amounts to 0.035%).

Relevant Trends in the Data

Preliminary analysis of the data has identified three overlapping trends, in relation to each of the three variables. Within each family, all parameters decrease with increasing average acceleration, approaching the reference values corresponding to the Hohmann transfers. Moreover, all transfer parameters decrease across families for increasing total infinity velocity, the other variables being equal. Lastly, a quadratic trend is observed with respect to fraction infinity velocity.

Database Generation

For generation of a large number of trajectory data, for example for extension of the model to other targets, establishment of a continuation problem is recommended. The automation of such a process can be easily achieved by an upper layer of scripting, but requires a significant effort for familiarizing with the specific problem and setting up the continuation properly. If a direct method such as the one implemented in DITAN is used, the main issues are caused by the inability of jumping from one set of transfers to the other. Typically, a solution is found that has the same number of revolutions as the initial guess. Moreover, such complex problems can be only partially automated: normally the refinement of the solution requires manual adjustments.

7.1.2. Answer to the Second Research Question

The second research question and related sub-questions are reported here for easy reference:

RQ2 - *To which extent can empirical functions derived by curve-fitting model trends in the transfer parameters depending on the system parameters, and accounting for infinity velocity at departure and arrival?*

- **RQ2.1** - *Which analytic relations describe these trends best and with what accuracy?*
- **RQ2.2** - *Which is the performance of the modelling tool resulting from the combination of such model functions in computing transfers performance parameters?*
  - **RQ2.2.1** - *Which is the performance in relation to transfers between circular coplanar orbits? Is the requirement of maximum percent error of 5% for all transfer parameters met, when the analysis is extended to include the effect of the infinity velocities?*
  - **RQ2.2.2** - *Which is the performance in relation to transfers optimized in the full ephemeris model? Is the requirement of maximum percent error of 15-20% for all transfer parameters, that is typically adopted of the intended applications, met?*

Model Functions

Fit models have been derived for each of the trends mentioned in the above, that involved all three variables: $\bar{a}$, $v_{\infty,tot}$ and $\widehat{v}_{\infty,f}$. Firstly, within each family, the evolution of the transfer parameters is well approximated by a linear combination of hyperbolic basis functions, resulting, for the reference family, in maximum errors of 0.01% for the ΔV, 1% for the transfer time and 0.6% for the transfer angle. Secondly, by analyzing the reference curves ($v_{\infty,i} = v_{\infty,f}$) in relation to the total infinity velocity, the trends in the hyperbolic coefficients are successfully modelled by polynomial functions, of order three for the ΔV and of order two for transfer time and angle. Finally, a parabolic correcting factor is derived that accounts for the distribution of the total infinity velocity between departure and arrival. The parabolic coefficients can as well be mapped and determined from the total infinity velocity. The correction is not needed in the case of the ΔV, for which the accuracy is already in the order of few m/s.

Model Accuracy

The accuracy of the model has been assessed through a number of independent analyses, both for circular coplanar transfers and for the full ephemeris model. Firstly, a study of the residuals identified bounds for the percent errors with respect to the trajectories dataset, that amount to +0.046/-0.106% for the ΔV, +1.526/-0.906% for the transfer time and +1.179/-1.133% for the transfer angle. Verification carried out on dedicated test cases has shown agreement with the residuals analysis, resulting in maximum errors of +0.03/-0.5% for the ΔV, +0.54/-0.35% for the transfer time and +0.40/-0.25% for the transfer angle. Finally, comparison with four transfers optimized in the full ephemeris model produces errors within 1% for the ΔV, between 12.2 and 14.8% for the transfer time and between 9.8 and 11.3% for the transfer angle.

Model Performance

With regard to the model accuracy, the assessments proved compliance with the requirements, both for the simplified and for the full model. In terms of efficiency, it enables to have instant estimates for ΔV, time of flight and departure date, which can make the model very suitable for high-level mission concept assessments. As for the limitations of the model, the comparison with the full ephemeris model shows no correlation between the errors and the input parameters, suggesting that most of the inaccuracy is due to the neglected effect of the eccentricity. Moreover, it is pointed out that the model is restricted to the thrust-coast-thrust type of transfer, which is not always feasible, and when it is, it might not be the optimal one.

Methodology

The successful modelling of the Earth-Mars transfers is not only relevant for the development of this set of fit functions, but most importantly because it confirms the potential of generating automatically a large number of low-thrust transfers and modelling the underlying trends by means of empirical relations. Having consolidated this methodology, the extension to other targets and/or types of transfers is expected to be faster and more straightforward.

7.2. Recommendations for Future Work

The lessons learned of the current project are concerned with several theoretical and practical aspects. First of all, opportunities of enriching the current model are envisaged, with the effort of enhancing the model performance for real applications. Furthermore, one of the important outcomes of the research is the development of a methodology that enables to extend the model in terms of validity and/or applicability. At last, recommendations are also formulated with regard to the operational aspects of the optimization.

Model Enhancement

The limitations of the model are mainly associated with the simplifications used for the derivation of the transfers, rather than with the methodology used. The potential of relaxing some of the assumptions is envisaged, although this process would most likely enhance the complexity of the model, and a trade-off between these two aspects should be carried out. In particular, including the effect of the eccentricity of Mars is of great interest. On the contrary, enhancement aimed at the improvement of the model performance in the current setup is not considered very interesting, as the fit models are already very accurate. Another opportunity for enhancement would be the extension of the analysis to other classes of transfers, with a different thrust profile. As it has been shown that the significant discontinuities between sets of transfers exist, use of multiple model functions is advised, in order to maintain the same accuracy levels. In this line of reasoning, also fixed-time mass-optimal transfers could be included.

Model Extension

The consolidation of a method for characterization and modelling of SEP transfers simplifies the extension to other targets (Venus, asteroids) and/or return transfers. It is strongly advised to spend time on the investigation and analysis of a few transfers before proceeding with the generation of a large dataset. The savings in terms of time and effort that follow from a well-posed continuation problem are not to be overlooked, since a very high level of automation can be achieved even for complex optimization processes.

Optimization

Use of an optimization tool with many functionalities and options such as DITAN has allowed to investigate a wide class of transfers, and to gain insight into the physics of the problem. However, when a specific thrust profile is of interest, as it was in the second part of the study, use of a dedicated optimization tool that allows to force a specific arc sequence is recommended. Even the development of an *ad-hoc* optimizer could be advantageous, due to the complexity and time consumption of propely setting up the optimization for tools such as DITAN.

Appendices

A. Constants and Parameters Used

A brief overview of the constant parameters that were used for the calculations is included.

Values of the gravitational parameters are derived from [Wertz, 2001] and summarized in Table 1:

Celestial body	**Symbol**	**Value** $[m^3/s^2]$
Sun	μ_{Sun} (μ)	1.3272×10^{20}
Earth	μ_{Earth}	3.9860×10^{14}
Mars	μ_{Mars}	4.2832×10^{13}
Moon	μ_{Moon}	4.9064×10^{12}
Jupiter	$\mu_{Jupiter}$	1.2669×10^{17}

Table 1: Gravitational parameters of most relevant celestial bodies. μ_{Sun} is normally referred to simply as μ throughout the report.

The value used for the astronomical unit corresponds to 149597870.7 km, from which the distances of Table 2 follow. Those are used for the computation of the reference Hohmann transfers, as in Table 3.

Celestial body	**Distance** [AU]	**Distance** [km]
Mercury	0.387099	0.57909176×10^8
Venus	0.723332	0.108208928×10^9
Earth	1	0.1495978707×10^9
Mars	1.523662	0.22793664×10^9

Table 2: Sun distance of most relevant celestial bodies, expressed in astronomical units and in km.

Target	r_f [AU]	a_T [AU]	V_1 [km/s]	ΔV_1 [km/s]	$V_{circ,2}$ [km/s]	V_2 [km/s	ΔV_2 [km/s]	ΔV [km/s]	TOF [days]	TOF [years]
Mercury	0.3871	0.6936	22.252	7.533	47.872	57.486	9.612	17.144	106	0.289
Venus	0.7233	0.8617	27.289	2.495	35.021	37.727	2.707	5.202	146	0.400
Mars	1.5237	1.2618	32.729	2.945	24.130	21.481	2.649	5.594	259	0.709

Table 3: Detailed computation of Hohmann transfer burns for several destinations.

Values used for the standard gravity constant and the solar constant are:

$$g_0 = 9.80665 \text{ m/s}^2$$
$$W_{1\text{AU}} = 1366 \text{ W/m}^2$$

B. Models Used

B.1. Dynamics Model: Perturbations

It is here reported on the numerical assessment carried out during the literature review, that has led to adopt the dynamical model that consists of the two-body problem, with the addition of the perturbing effect of the thrust. The perturbing factors that have been included in the assessment are listed in the following, while a comprehensive analysis can be found in [Wertz, 2001] and [Wakker, 2015].

N-body gravity

Perturbing acceleration acting on body i due to body j is:

$$\vec{f}_{nb} = \mu_j \left(\frac{\vec{r}_{ij}}{r_{ij}^3} - \frac{\vec{r}_j}{r_j^3} \right) \tag{1}$$

where μ_j is the gravitational parameter of the perturbing body j, and the vectors $\vec{r}_j$ and $\vec{r}_i$ are position vectors relative to the main attracting body [Wakker, 2015].

Atmospheric drag

The acceleration due to drag acts in the direction opposite to the relative velocity vector [Wakker, 2015]:

$$\vec{f}_{drag} = -C_D \frac{1}{2} \rho \frac{A}{m} |\vec{v}| \vec{v} = -\frac{1}{2} \frac{\rho}{B} |\vec{v}| \vec{v} \tag{2}$$

where ρ is the atmospheric density, $\vec{v}$ is the relative velocity vector, C_D is the drag coefficient, A is the cross-sectional area, m is the mass of the satellite and B is defined as ballistic coefficient. For interplanetary flights considered in this report, the density ρ is very low if not zero, thus $\vec{f}_{drag}$ will be neglected from now on.

Non-spherical gravity

The expression for the gravitational potential of the Earth due to the irregularities in its mass distribution, when assumed static, is [Wakker, 2015]:

$$U = -\frac{\mu}{r} \left[1 - \sum_{n=2}^{\infty} J_n \left(\frac{R}{r} \right)^n P_n(\sin\phi) + \sum_{n=2}^{\infty} \sum_{m=1}^{n} J_{n,m} \left(\frac{R}{r} \right)^n P_{n,m}(\sin\phi) \{ \cos m(\Lambda - \Lambda_{n,m}) \} \right] \tag{3}$$

where r, ϕ, Λ are the spherical coordinates in geocentric rotating reference frame, R is the mean equatorial radius, J_n, $J_{n,m}$ and $\Lambda_{n,m}$ are constant values associated with model parameters. The terms $P_n(\sin\phi)$ are called *Legendre polynomials* of degree n, while the terms $P_{n,m}(\sin\phi)$ are *associated Legendre functions of the first kind* of degree n and order m, which are defined as [Wakker, 2015]:

$$P_n(x) = \frac{1}{(-2)^n n!} \frac{d^n}{dx^n} (1-x^2)^n \qquad P_{n,m}(x) = (1-x^2)^{m/2} \frac{d^m P_n(x)}{dx^m} \tag{4}$$

In Equation 3 one can distinguish the Newton potential (first term) from the deviations from the gravitational potential of a spherical body with radially symmetric mass density distribution. The latter are called zonal, tesseral and sectorial harmonics and are displayed in Figure 1.

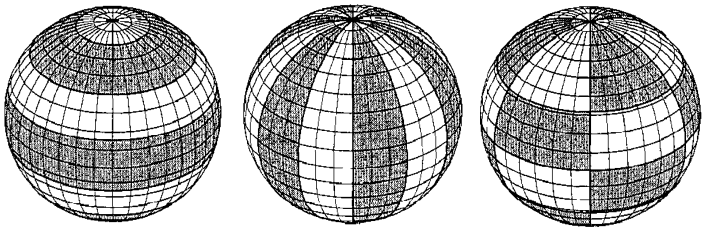

Figure 1: Visualization of zonal, sectoral and tesseral harmonics [Wertz, 2001].

Since the largest of the geopotential terms is by far represented by J_2, one common simplification for the perturbing acceleration is the following [Wertz, 2001]:

$$\vec{f}_{geo} = -\vec{\nabla}\left(U + \frac{\mu}{r}\right) \quad \rightarrow \quad \vec{f}_{geo,J2} = -\vec{\nabla}\left(\frac{1}{2}\mu J_2 \frac{R^2}{r^3}(3\sin^2\phi - 1)\right) \tag{5}$$

The maximum values of the r and ϕ components of $\vec{f}_{geo,J2}$ at specified distance r are:

$$|\vec{f}_{max,r}| = 3\mu J_2 \frac{R^2}{r^4} \qquad |\vec{f}_{max,\phi}| = \frac{3}{2}\mu J_2 \frac{R^2}{r^4} \tag{6}$$

If these components are evaluated at the edge of the sphere of influence of the Earth, their values are in the order of magnitude of 10^{-21} m/s^2, which is already very small compared to the other terms and can therefore be neglected when analyzing interplanetary flight, along with atmospheric drag.

Radiation Pressure

Spacecraft travelling the Solar System experience a radiation force caused by the combination of direct solar radiation, albedo radiation and thermal radiation emitted by celestial bodies. Restricting ourselves to the most relevant direct solar radiation acceleration, Equation 7 is reported as derived in [Wakker, 2015]:

$$F = C_R \frac{WA}{c} \tag{7}$$

where C_R is the satellite's reflectivity, W is the solar flux, c is the speed of light and A is the cross-sectional area. It follows that the perturbing force on the satellite's motion has the form:

$$\vec{f}_{rad} = -\frac{F}{m}\vec{e}_{Sun} = -C_R \frac{WA}{mc}\vec{e}_{Sun} \tag{8}$$

and acts along the line connecting the satellite and the Sun, but pointing in the direction opposite to the Sun. A first-order approximation of the solar power density at arbitrary distance from the Sun can be obtained starting from the solar constant, defined conventionally as the mean solar irradiance at a distance of one astronomical unit: $W_{1\,AU} = 1366$ W/m^2. The solar flux at heliocentric distance r_{AU} (measured in AU) is [Lissauser and de Pater, 2013]:

$$W = \frac{W_{1\,AU}}{r_{AU}^2} \tag{9}$$

Although negligible for Earth orbits below approximately 800 km altitude [Wertz, 2001], the solar radiation force is a dominant perturbation for interplanetary flights, and it is therefore worth investigating further for our application.

Thrust

Generally speaking, the one intended perturbation for the ballistic flight of a spacecraft is the thrust generated by a rocket engine[1]. The propulsive force has been introduced in Subsection 2.1.1, and its generation is described by Equation 10:

$$T = \dot{m}c_e = \dot{m}g_0 I_{sp} \tag{10}$$

For low-thrust propulsion systems, the specific impulse is typically one order of magnitude higher with respect to conventional chemical engines, while the thrust is much lower. For typical SEP systems, the specific impulse is in the order of 1600 s for gridded engines and of 3000 s for plasma engines, while the specific thrust amounts to 10^{-4} m/s^2 [Racca, 2003].

[1] Sometimes, the effect of other perturbations is used advantageously for orbit design. Analysis of these cases is however beyond the scope of this study.

Assessment

The aim of the following paragraphs is to assess which of the elements introduced in Subsection B.1 should be included in the dynamical model. Since their relevance can only be established quantitatively when the performance requirements of the model to be developed are known, the focus will be in determining the order of magnitude of each contribution and drawing general conclusions that apply to all Earth-Mars transfers.

The assessment is carried out by computing the values of the perturbing accelerations for a spacecraft that is located halfway between the Earth and Mars (1.25 AU from the Sun) and travels in a coplanar Solar System. Besides the main attracting body, the gravitation due to Earth, Moon, Mars and Jupiter are included[2]. Table 4 reports the assumptions made in the calculations as derived from textbooks and previous missions.

Parameter	***Value***	***Unit***
μ_{Sun}	1.3272×10^{20}	m^3/s^2
μ_{Earth}	3.9860×10^{14}	m^3/s^2
μ_{Mars}	4.2832×10^{13}	m^3/s^2
μ_{Moon}	4.9064×10^{12}	m^3/s^2
$\mu_{Jupiter}$	1.2669×10^{17}	m^3/s^2
c	299792458	m/s
AU	149597870.66	km
W_{1AU}	1366	W/m^2
C_R	1.5	-
A	6	m^2
M	1500	kg
C_D	2.5	-

Table 4: Assumptions made: lines 1-7: values from [Wertz, 2001], line 8: value from [Lissauser and de Pater, 2013], lines 9-12: values based on mission heritage.

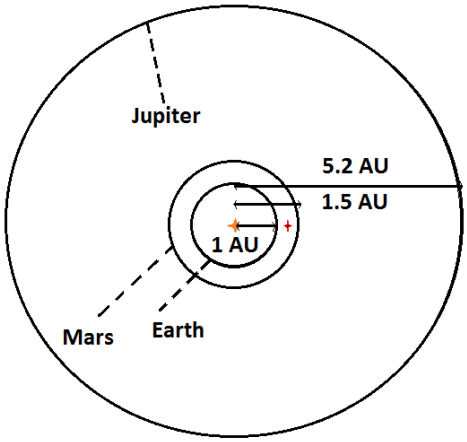

Figure 2: Sketch of the geometry used for the computations.

The results of the computation are summarized in Table 5. There are several orders of magnitude between the gravitational attraction of the Sun and all the other terms, which justifies the adoption of a two-body dynamical model for the description of the problem. The most relevant perturbations are due to point-mass attraction, specifically from the Earth and Jupiter, which are in the order of 10^{-7} m/s^2. However, one should keep in mind that the case of closest approach to the planets was considered, while it is hardly ever the case and perturbing accelerations can be much smaller along the orbit. Next to gravitational forces, radiation pressure has quite a significant impact as well, in the order of 10^{-8} m/s^2.

Acceleration	***Description***	***Value*** $[\frac{m}{s^2}]$
$\vec{f}_{Sun}$	Sun attraction	3.8×10^{-4}
$\vec{f}_{Earth}$	Earth attraction	2.7×10^{-7}
$\vec{f}_{Moon}$	Mars attraction	3.0×10^{-8}
$\vec{f}_{Mars}$	Moon attraction	3.3×10^{-9}
$\vec{f}_{Jup}$	Jupiter attraction	1.5×10^{-7}
$\vec{f}_{drag}$	atmospheric drag	$<< 10^{-10}$
$\vec{f}_{J2}$	J2 effect	$<< 10^{-10}$
$\vec{f}_{rad}$	radiation pressure	1.8×10^{-8}
$\vec{f}_T$	low-thrust	10^{-4}

Table 5: List of perturbing acceleration and their magnitude.

[2]These terms are estimated in the worst case scenario (minimum possible distance from the body) although this is often not realistic.

B.2. Propulsion System Model

The model used to describe the decay of the available power with the Sun-spacecraft distance consists of the inverse-square power law, with the addition of a constant efficiency factor, as in Equation 2.13. More complex models exist, which have been compared during the review of the literature, as it is presented here to justify the final selection. An alternative to the constant efficiency is the expression of this factor as a function of the operating temperature T_{SP}, which is also a function of the Sun-spacecraft distance r: $\eta_{SP}(T_{SP}(r))$. Since a high operating temperature is not the only cause for degradation of the solar arrays, η_{SP} is composed of two contributions: one term η_r accounts for the mentioned effect of T_{SP} and depends on r, while the second term η_L accounts for the other losses and stays constant:

$$\eta_{SP} = \eta_L \eta_r = \eta_L \cos\delta[1 - C_T(T_{SP} - T_0)] \tag{11}$$

where δ is the angle between the normal to the surface and the Sun direction, T_0 is a reference temperature and C_T is the temperature coefficient. The operating temperature of the solar arrays T_{SP} is computed by balancing the incoming solar radiation (received by the solar array surface A) and the infrared radiation radiated by the surface A_{IF}, according to Equation 12:

$$T_{SP} = \left(\frac{W_{1,AU}\alpha\cos\delta}{r^2\sigma\kappa\epsilon}\right)^{0.25} \tag{12}$$

where α is the surface absorptivity in the solar spectrum, ϵ is the surface emissivity in the infrared spectrum, σ is the Stefan-Boltzmann constant and the parameter κ represents the ratio between the areas A_{IF} and A. Equations 2.13, 2.14, 11 and 12 enable to build up a more sophisticated power supply model, which combines the decrease in incoming solar radiation with the positive effect of the reduced temperature of the solar cells. The price for the increased accuracy is clearly the complexity of this second model.

A third alternative for the power supply model consists in adopting the simple power law as in Equation 2.13, but with an exponent $\tau \neq 2$. Fortescue, Stark and Swinerd, for instance, suggest the adoption of $\tau = 1.5$ to include the effect of solar array degradation [Fortescue et al., 2003]. This solution keeps the model simple, while approximating the trend described above by the combination of Equations 2.13 and 11.

$$P_{SP} = \eta_{SP} P_0 \left(\frac{r_0}{r}\right)^{1.5} \tag{13}$$

The main characteristics of the three models described in the previous paragraphs are summarized in Table 6. In order to make a proper comparison between the three, it is needed to make some considerations on how to select the reference values that allow an effective comparison.

#	***Model***	***Exponent*** τ	***Efficiency*** η	***Equations***
1	Quadratic power law	2	η_{SP}	$P_{SP} = \eta_{SP} P_0 \left(\frac{r_0}{r}\right)^2$
2	Temperature dependent	2	$\eta_L \eta_r(r)$	$P_{SP} = \eta_{SP} P_0 \left(\frac{r_0}{r}\right)^2$ $\eta_{SP} = \eta_L \cos\delta[1 - C_T(T_{SP} - T_0)]$ $T_S = \left(\frac{W_{1,AU}\alpha\cos\delta}{r^2\sigma\kappa\epsilon}\right)^{0.25}$
3	Generic power law	τ	η_{SP}	$P_{SP} = \eta_{SP} P_0 \left(\frac{r_0}{r}\right)^{\tau}$

Table 6: Characteristics of different power supply models.

In models 1 and 3, the curves are entirely defined by the constant parameter η_{SP} and by the reference distance r_0, which is normally associated with the Sun-Earth distance 1 AU. If the comparison was only to be carried out between these two models, it would make sense to simply consider $r_0 = 1$ AU and η_{SP}, which implies: intersection of the two curves at Sun-Earth distance, pessimistic power estimation for model 3 with respect to model 1 when $r < 1$ AU, optimistic estimation for model 3 with respect to model 1 when $r > 1$ AU. However, when also model 2 is included in the evaluation, things get a bit more complicated. Since in model 2 the efficiency is not a constant, it is sensible to make some considerations when assuming a value for η.

If the incoming sunlight is assumed to be perpendicular to the surface of the solar panels ($\delta = 0°$), the overall efficiency η_{SP}, in model 2, coincides with η_L when $T_{SP} = T_0$, which is a reference temperature, for example the temperature at which testing of the panels is conducted. In practical cases, it is reasonable to know the efficiency η_L at the reference temperature, and then to superimpose the variations due to the change in temperature in order to obtain η_{SP} as a function of r. With the purpose of generating a valuable comparison, in the following assumptions will be made for the value of the efficiency η_L, which is also the η_{SP} at $T_{SP} = T_0$ for model 2. For models 1 and 3, the factors will be scaled such that all the three models perform equivalently at $T_{SP} = T_0$ (which means at a distance r_0 different than 1 AU). This can be obtained by choosing η_{SP} for models 1 and 3 equal to η_L in model 2, while using as reference distance r_0 the distance at which $T_{SP} = T_0$. Table 7 summarizes the assumptions made to generate the curves shown in Figure 3. From those assumptions, a reference distance $r_0 = 1.263$ AU follows, as visualized in Figure 3.

Parameter	***Description***	***Value***	***Unit***
Constants			
$W_{1,AU}$	solar constant	1366	W/m^2
σ	Stefan-Boltzmann constant	5.6704×10^{-8}	W/m^2K^4
T_0	reference temperature	293	K
Solar arrays parameters			
A	solar array area	30	m^2
α	surface absorptivity	0.75	–
ϵ	surface emissivity	0.8	–
κ	radiating/absorbing surface ratio	4	–
δ	sun aspect angle	0	°
C_T	temperature coefficient	0.5	$\%/K$
η_L	partial efficiency[a]	0.2733[b]	–
η_{SP}	overall solar panels efficiency[c]	0.3	–

Table 7: Assumptions made: lines 1-2 from [Lissauser and de Pater, 2013], lines 3-11 based on existing systems.

[a] Efficiency that accounts for losses other than solar array degradation when Equation 11 is applied.
[b] Determined such that overall efficiency $\eta_{SP} = 0.3$ when the distance spacecraft-Sun is $r_{AU} = 1\,AU$.
[c] Efficiency that accounts for all losses when constant efficiency model is used.

It is emphasized that the decision of taking a reference distance different than 1 AU is arbitrary, although extensively justified, as well as the assumptions presented in Table 7. The purpose of this analysis was limited to draw general considerations about the curves in Figure 3, as the design parameters were not yet known.

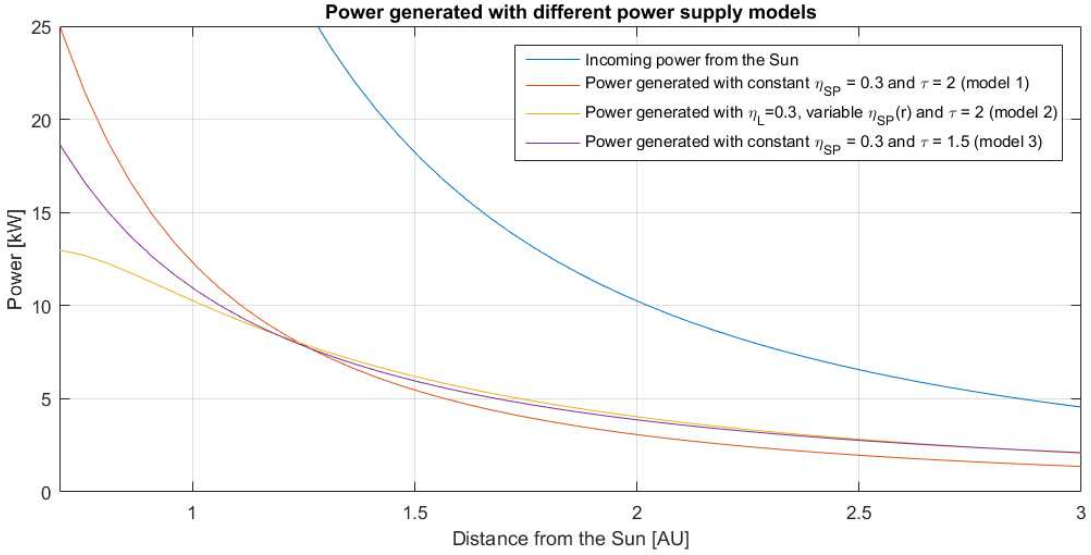

Figure 3: Comparison between different power supply models.

From Figure 3, it is noticed that for distances smaller than the reference distance both power laws, models 1 and 3, significantly overestimate the available power when getting closer to the Sun, and that the error increases as the Sun-spacecraft distance decreases. Compared to model 1, model 3 brings about smaller errors and is sufficiently close to the more accurate model 2, at least for distances bigger than 1 AU, as the ones we are interested in. At 1 AU, the percent error in power is 19.5% for model 1 and 7.7% for model 3, and decreases for both while getting closer to the reference distance. For distances bigger than the reference one, which in this specific case falls about halfway between Earth and Mars (1.26 AU), the three models are more consistent with one another. Specifically, the curve corresponding to model 3 converges asymptotically to the one of model 2. Between 1.1 and 3.1 AU, the percent error for this model stays below 3.5%. As for model 1, there is still a relevant offset relative to model 2, but now this is smaller and more stable than for $r < r_0$ (for example, 11.5% at 1.5 AU, 23.8% at 2 AU), besides resulting in an underestimation of the available power, which is less dangerous for the design.

We can conclude that for Earth-Mars transfers (r between 1 and 1.5 AU) the three models procude approximately the same curve. Model 3 is much more accurate than model 1, while preserving its simplicity. On a more practical note, model 1 is normally a built-in functionality in the software tools used for this type of problems, while model 3 is less commonly used and would require dedicated implementation in the case of DITAN. For very accurate estimations, model 2 is the only one that captures the trend due to the degradation of the solar arrays, which becomes more and more important for smaller distances. However, for many practical applications such accuracy is not needed and unnecessarily complicates the problem.

Bibliography

[Bernelli Zazzera et al. 2002] BERNELLI ZAZZERA, F. ; VASILE, M. ; FORNASARI, N. ; MASARATI, P.: *Design of Interplanetary and Lunar Missions Combining Low Thrust and Gravity Assists, Final Report*. Milano, Italy : Politecnico di Milano, September 2002

[Betts 1998] BETTS, J. T.: Survey of Numerical Methods for Trajectory Optimization. In: *Journal of Guidance, Control and Dynamics* 21 (1998), Nr. 2

[Biesbroek 2016] BIESBROEK, R.: *Lunar and Interplanetary Trajectories*. Springer Praxis Books, 2016 ISSN 2365-9599

[Campagnola et al. 2014] CAMPAGNOLA, S. ; BOUTONNET, A. ; SCHOENMAEKERS, J. ; GREBOW, D. J. ; PETROPOULOS, R. P.: Tisserand-Leveraging Transfers. In: *Journal of Guidance, Control, and Dynamics* 37 (2014)

[Chen et al. 2008] CHEN, K. J. ; KLOSTER, K. W. ; LONGUSKI, J. M.: A Graphical Method for Preliminary Design of Low-Thrust Gravity-Assist Trajectories. In: *Astrodynamics Specialist Conference and Exhibit* (2008)

[Conway 2010] CONWAY, B.: *Spacecraft Trajectory Optimization*. Cambridge University Press, 2010

[Curtis 2013] CURTIS, H.: *Orbital Mechanics for Engineering Students*. Butterworth-Heinemann, 2013. – ISBN 978-0-08-097747-8

[Dankanich 2010] DANKANICH, J. W.: *Aerospace Technologies Advancements*. INTECH, Open Access Publisher, 2010

[Dysli 1977] DYSLI, P.: Analytical ephemeris for planets (MATLAB code `AST_orbplt.m`), 1977

[Estublier et al. 2007] ESTUBLIER, D. ; SACCOCCIA, G. ; AMO, J. Gonzalez del: *Electric Propulsion on SMART-1*. Noordwijk, The Netherlands : ESA bulletin, February 2007

[Fatemi et al. 2005] FATEMI, N. S. ; ALTRO ; ALTRO ; ALTRO: Performance of high-efficiency advanced triple-junction solar panels for the LILT Mission Dawn. In: *31st Photovoltaic Specialists Conference* (2005)

[Fortescue et al. 2003] FORTESCUE, P. ; STARK, J. ; SWINERD, G.: *Spacecraft Systems Engineering*. Chichester, United Kingdom : John Wiley and Sons, 2003

[Galletti 2017] GALLETTI, E.: Semi-Analytic Methods for Low-Thrust Interplanetary Transfers / Delft University of Technology. Delft, The Netherlands, January 2017. – Literature Survey

[Gondelach 2012] GONDELACH, D. J.: *A Hodographic-Shaping Method for Low-Thrust Trajectory Design*, Delft University of Technology, Master Thesis, August 2012

[Kluever 2014] KLUEVER, C.: Efficient Computation of Optimal Interplanetary Trajectories Using Solar Electric Propulsion. In: *Journal of Guidance, Control, and Dynamics* (2014). – URL `http://arc.aiaa.org/doi/abs/10.2514/1.G000144`.– ISSN 0731-5090

[Kuninaka and Kajiwara 2011] KUNINAKA, H. ; KAJIWARA, K.: Overview of JAXA's activities on Electric Propulsion. In: *32nd International Electric Propulsion Conference* (2011)

[Lissauser and de Pater 2013] LISSAUSER, J. J. ; PATER, I. de: *Fundamental Planetary Science: Physics, Chemistry and Habitability*. Cambridge University Press, September 2013. – ISBN 9780521618557

[Oh et al. 2004] OH, D. ; RANDOLPH, T. ; KIMBREL, S. ; MARTINEZ-SANCHEZ, M.: End-to-End Optimization of Chemical-Electric Orbit-Raising Missions. In: *Journal of Spacecraft and Rockets* 41 (2004), Nr. 5

[Oh 2006] OH, D. Y.: Development of a Simple Analytic Model for Optimum Specific Impulse Interplanetary Low Thrust Trajectories. In: *Advances in the Astronautical Sciences* (2006), January

[Oh and Landau 2010] OH, D. Y. ; LANDAU, D.: Progress on a Simple Analytic Model for Interplanetary Solar Electric Low Thrust Trajectories. In: *46th AIAA Joint Propulsion Conference* (2010), July

[Oh and Landau 2011] OH, D. Y. ; LANDAU, D.: A Simple Semi-Analytic Model for Optimum Specific Impulse Interplanetary Low Thrust Trajectories. In: *32nd International Electric Propulsion Conference* (2011)

[Oh and Landau 2013] OH, D. Y. ; LANDAU, D.: Simple Semi-Analytic Model for Optimized Interplanetary Low-Thrust Trajectories Using Solar Electric Propulsion. In: *Journal of Spacecraft and Rockets* 50 (2013)

[Ohndorf 2016] OHNDORF, A.: *Multiphase Low-Thrust Trajectory Optimization Using Evolutionary Neurocontrol*, Delft University of Technology, Dissertation, 2016

[Petropoulos and Sims 2002] PETROPOULOS, A. E. ; SIMS, J. A.: A Review of Some Exact Solutions to the Planar Equations of Motion of a Thrusting Spacecraft. In: *2nd International Symposium Low Thrust Trajectories* (2002)

[Racca 2003] RACCA, G.: New challenges to trajectory design by the use of electric propulsion and other new means of wandering in the solar system. In: *Celestial Mechanics and Dynamical Astronomy* 85 (2003), S. 1–24. – ISSN 09232958

[Sovey et al. 2001] SOVEY, J. S. ; RAWLIN, V. K. ; PATTERSON, M. J.: Ion Propulsion Development Projects in U.S.: Space Electric Rocket Test I to Deep Space 1. In: *Journal of Propulsion and Power* 17 (2001), Nr. 3

[Vasile 2009] VASILE, M.: *DITAN User Manual*. Politecnico di Milano, May 2009

[Wakker 2015] WAKKER, K. F.: *Fundamentals of Astrodynamics*. TU Delft Library, January 2015. – ISBN 9789461864192

[Wertz 2001] WERTZ, J.: *Mission Geometry: Orbit and Constellation Design and Management*. Space Technology Library, 2001. – ISBN 9781881883074